
Universidad de Alcalá
Environmental fate of microplastics under ageing conditions
Carmen Sorasan
2022
PhD in Forensic Science

Doctoral Program in:

Forensic Science

Environmental fate of microplastics under ageing conditions

Doctoral Thesis presented by:

Carmen Sorasan

Alcalá de Henares, 2022

Preface

The present dissertation is sent for the degree of Doctor of Philosophy in the University of Alcalá, Madrid, Spain. This Thesis hold the research conducted at the Department of Analytic Chemistry, Physical Chemistry and Chemical Engineering to University of Alcalá from November 2020 to June 2022 under the supervision of Dr. Roberto Rosal García, Dr. Antonio Rodríguez Fernández-Alba, and Dr. Fernando Ernesto Ortega Ojeda, professors at University of Alcalá.

The results obtained during the study for this Thesis, grouped into three scientific articles, have been published in three international journals: Environmental Pollution, Microplastics, and Science of the Total Environment.

The results presented in this Ph.D. dissertation are original, except where due reference has been made to the work of others.

No part of this dissertation, or any like it, has been, or is currently being, sent for any degree of other qualification at any other university.

Carmen Sorasan

Alcalá de Henares

June 2022

Agradecimientos

Es el momento de dar las gracias a todas aquellas personas que han hecho posible este trabajo.

Primero, a mi director de Tesis, el Dr. Roberto Rosal, artífice de este trabajo: "Ha sido un gran honor trabajar y aprender contigo. ¡Gracias! Gracias por toda la dedicación, el tiempo y la confianza depositada en mí, gracias por todo lo que hizo posible que una simple idea se materialice, coja forma y llegue a buen puerto."

Asimismo, quisiera agradecer todo su esfuerzo a mi Codirector de Tesis, profesor emérito de nuestra universidad, el Dr. Antonio Rodriguez Fernandez-Alba, que hizo posible el inicio y el desarrollo de este trabajo abriendo puertas y tendiendo puentes de conocimiento profesional y personal.

A mi tutor, Dr. Fernando Ernesto Ortega Ojeda quiero agradecerle la orientación y el apoyo para entender el maravilloso mundo de las Ciencias Forenses a través de estudios estadísticos.

A la Dra. Begoña Espina por darme la oportunidad de conocer/trabajar/aprender en su equipo Water Quality en INL Braga, Portugal, a mi supervisora Dra. Patricia Taladriz y especialmente a mi compañera y amiga Lourdes Gonçalves "Thank you a lot".

Un especial agradecimiento a mi compañero y amigo Dr. Raúl Alonso de Águila que ha sido una presencia inequívoca en todo momento de este trabajo ayudándome a entender que la humildad, la paciencia y la generosidad son los mejores aliados del investigador.

También quiero agradecer a la profesora Guadalupe Ramos Caicedo por sus permanentes mensajes llenas de optimismo y buena energía.

Agradezco a todos mis compañeros del Departamento de Ingeniería Química de la Universidad de Alcalá por el buen ambiente de trabajo en el laboratorio.

Por último, quisiera agradecer a mi querido marido, Niculai, por ser el maestro y el apoyo incondicional de mi vida en los últimos 30 años.

Contents

Abstract

Plastics are ubiquitous in our society. It has been estimated that, after the onset of their industrial production, near 10 000 million tons of plastic have been synthesized worldwide, many of which ended up in the environment. The concern about its impact started in the 50s with the evidence of the accumulation of plastic debris in the oceanic gyres and the proofs on the pervasive presence of small plastic fragments in the most diverse environments. The reason is that under the influence of environmental activates, plastics undergo chemical changes that result in the alteration of their physicochemical properties eventually leading to their fragmentation into small fragments. Due to historical reasons, plastic fragments are generally referred to as microplastics if they are in the 1 μm-5 mm range or nanoplastics, a term used for fragments < 1 μm with colloidal behaviour.

This work investigated the structural and chemical changes of plastics undergoing conditions that simulated solar radiation with emphasis in the generation of small plastic particles. The plastics selected were polyethylene, polypropylene, and polystyrene either in the form of pure pellets, commercial plastics, and debris sampled from sandy beaches. We recorded Fourier Transform Infrared (FTIR) spectra to track the absorption peaks associated to photochemical ageing and used Orthogonal Partial Least Squares Discriminant Analysis (OPLS-DA) chemometric methods to process the whole spectral information. Flow cytometry combined with laser diffractometry was used to quantify the generation of small (< 100 μm) plastic particles. Micro-FTIR measurements were used to track the formation of oxygenated moieties in small fragments, including hydroxyl, carbonyl, and carbon-oxygen bonds, as well as to assess the presence of plastic in the nanoplastic (< 1 μm) size fraction.

The results show that FTIR spectra allowed to differentiate specimens according to their degree of ageing, although none of the classic degradation indexes, based on peaks from specific moieties, could be related to the accumulated exposure to photochemical ageing. The results also show the generation of an elevated number of small plastic fragments (1–5 μm), that reached 10^4-10^5 particles/g for new polyethylene pellets and

10^8–10^9 particles/g when exposing polyethylene, polypropylene, or polystyrene from marine debris. Evidence has also been found on the production of a high number of nanoplastics with size in the few hundreds of nanometers as determined by dynamic light scattering, which could represent up to 10^{13} particles/g. It has also been demonstrated that ultraviolet irradiation favours the generation of nanoplastics from microplastics. The results of this Doctoral Thesis demonstrated that environmentally aged plastics deliver many small particles consistent with continuous fragmentation in all spatial dimensions. It should be noted that the number of small microplastics obtained was by far higher than that reported in the current sampling campaigns, which is relevant for the risk assessment of plastic waste and to close the circuit of plastic delivered to the environment.

Resumen

Los plásticos son omnipresentes en nuestra sociedad. Se ha estimado que, tras el inicio de su producción industrial, se han sintetizado mundialmente unos 10 000 millones de toneladas de plástico, muchas de las cuales han terminado diseminadas en el medio ambiente. La preocupación por su impacto ambiental comenzó en los años 50 con la acumulación de evidencias sobre la gran cantidad de desechos plásticos presentes en los giros oceánicos, así como con las pruebas sobre la presencia generalizada de pequeños fragmentos de plástico en los más diversos ambientes. La razón es que, bajo la influencia de factores ambientales, los plásticos experimentan cambios químicos que dan como resultado la alteración de sus propiedades fisicoquímicas, lo que finalmente conduce a su desintegración en pequeños fragmentos. Por razones prácticas, los fragmentos de plástico se denominan microplásticos si se encuentran en el rango de 1 µm - 5 mm o nanoplásticos si se trata de fragmentos secundarios < 1 µm y presentan comportamiento coloidal.

Este trabajo investigó los cambios estructurales y químicos de los plásticos sometidos a condiciones que simularon la radiación solar con énfasis en la generación de pequeñas partículas plásticas. Los plásticos seleccionados fueron polietileno, polipropileno y poliestireno en forma de granza industrial y plásticos comerciales, así como desechos muestreados en playas. Los cambios producidos en los picos de absorción asociados al envejecimiento fotoquímico se estudiaron con espectroscopia infrarroja por transformada de Fourier (FTIR) y se utilizaron métodos quimiométricos de análisis discriminante de regresión de mínimos cuadrados parciales en proyección ortogonal (OPLS-DA) para procesar toda la información espectral. Se utilizó citometría de flujo combinada con difractometría láser para cuantificar la generación de pequeñas partículas plásticas (< 100 µm). Las mediciones de micro-FTIR permitieron determinar la formación de funciones oxigenadas en fragmentos pequeños, particularmente los correspondiente a grupos hidroxilo, carbonilo y otros enlaces carbono-oxígeno. También permitió evaluar la presencia de plástico en la fracción de tamaño < 1 µm.

Los resultados mostraron que los espectros FTIR permiten diferenciar fragmentos según su grado de envejecimiento, aunque ninguno de los índices de degradación habituales, basados en absorciones de grupos funcionales específicos, pudo relacionarse con la exposición acumulada al envejecimiento fotoquímico. Los resultados también mostraron la generación de un elevado número de pequeños fragmentos de plástico (1-5 μm), que alcanzó 10^4-10^5 partículas/g en el caso de granza de polietileno y 10^8-10^9 partículas/g al exponer polietileno, polipropileno o poliestireno procedente de desechos marinos. También se encontró evidencia de la generación de una cantidad grande de nanoplásticos con un tamaño de unos pocos cientos de nanómetros según medidas realizadas por dispersión dinámica de la luz, y que podrían representar hasta 10^{13} partículas/g. También se ha demostrado que la radiación ultravioleta favorece la generación de nanoplásticos a partir de microplásticos. Los resultados presentados en esta Tesis Doctoral demostraron que los plásticos envejecidos ambientalmente dan lugar a una gran cantidad de pequeñas partículas en un patrón consistente con una fragmentación progresiva en las tres dimensiones espaciales. La cantidad de pequeños microplásticos obtenidos fue muy superior a la habitualmente encontrada en las campañas ambientales de muestreo, lo que es un hecho relevante para la cuantificación del riesgo ambiental de los desechos plásticos, así como para cerrar el balance de plástico en el medio ambiente.

Objectives

The scientific community is putting a huge amount of effort into the study of the life cycle of plastic in the environment due to the need of clarifying the complex processes the chemical, mechanical and hydrolytic degradation that results in the creation of microplastics and nanoplastics. The main aim of this Doctoral Thesis is the study of the degradation processes of the plastics under environmental stressors, focused on the generation of secondary plastic particles, namely microplastics and nanoplastics. To achieve this goal, polyethylene, polypropylene, and polystyrene in different states of degradation will be used including new and recycled fabrication pellets, processed objects, and marine debris. Proper analytical techniques will be used to quantitatively track the degradation suffered under conditions that mimic environmental exposure with particular attention to the conditions leading to the generation of nanoplastic particles.

Specific goals:

- ✓ To investigate the generation of secondary microplastics and nanoplastics in laboratory conditions simulating photochemical ageing thanks to the use of commercial lamps that deliver UV irradiation for accelerated ageing exposure runs.
- ✓ To assess the use of flow cytometry for the quantification of microplastics as well as its combination with other techniques based on size segregation to obtain a particle size distribution of the smaller fraction of secondary microplastics.
- ✓ To evaluate the suitability chemometric models based on mid-infrared spectroscopic data for tracking the chemical changes underwent by plastics suffering photochemical and oxidative ageing.

General introduction

To put this work in context nothing best than the vision of global organisms. António Guterres, Secretary -General of the United Nations, in the foreword of The Sustainable Development Goals Report, 2020, wrote:

> The 2030 Agenda for Sustainable Development was launched in 2015 to end poverty and set the world on a path of peace, prosperity, and opportunity for all on a healthy planet. The 17 Sustainable Development Goals (SDGs), figure 1, demand nothing short of a transformation of the financial, economic, and political systems that govern our societies today to guarantee the human rights of all. They require immense political will and ambitious action by all stakeholders (The-Sustainable-Development-Goals-Report, 2020).

Figure 1 Illustration of Sustainable Development Goals: Ending poverty and hunger, improving health and education, gaining gender equality, access to clean water, adequate sanitation, and clean energy, a decent work and perspectives for economic stability, better and sustainable infrastructures, limited inequality, environmentally responsible production, and institutions able to guarantee peace and justice (The Sustainable Development Goals Report 2020).

And at the end of the same report, it reads: "Everything we do during and after this crisis [COVID-19] must be with a strong focus on building more equal, inclusive, and sustainable economies and societies that are more resilient in the face of pandemics, climate change, and the many other global challenges we face."

1. Polymers, plastics, plastic waste, and marine plastic litter

The technological advances of the second industrial revolution brought to humanity an impressive variety of petroleum materials and products. Synthetic polymers are among the most important of them. These materials, known as plastics, remain vital for the functioning and development of the economy. Plastics define the quality of life around the world making it easier and safer, while they are cornerstone to accelerate transition to a circular economy that allow material resources and energy to be used with greater efficiency.

Plastics will continue to be essential for our future, but we will not be able to enjoy the full potential of these materials if we do not address the global challenges related to their negative impact on the environment. Global issues demand global approaches and global solutions. Specifically, "The New Plastics Economy Global Commitment", held between more than 250 international organizations in collaboration with the United Nations and headed by Ellen MacArthur Foundation, advocated for the elimination of useless and problematic plastics as a way to keep the remaining plastics within the economy.

The 2021 Global Commitment Progress Report showed that over 500 organizations are joining into a common circular economy vision for plastics that pursues the reduction of plastic pollution at source. Specifically, companies that produce 20% of the plastic used for packaging worldwide committed to an ambitious target to reduce unnecessary plastic usage and its corresponding waste. This report stresses that: (1) After many year of growth, the worldwide production of virgin plastic is reaching its maximum, and is expected to fall faster in the near future; (2) Current progresses in circularity have been

made by promoting plastic recycling, but this approach is insufficient to tackle with the problem of plastic pollution and further efforts are needed for example in reducing the use of single-use plastics packaging; and (3) There is a growing body of evidence that many companies and public bodies are ready to support initiatives to reduce the burden of plastic pollution, but at the same time there is a consensus that voluntary initiatives are not enough by themselves (The Global Commitment 2021 Progress Report).

Plastic waste affects the quality of environmental life at all levels of the ecosystem. For example, in 2010, it is estimated that about 10 million metric tons (Mt) of plastic waste are entering the oceans every year, coming from countries that do not possess an adequate infrastructure for managing solid wastes, but also from high-income countries because of their high volume of waste generation (Law et al., 2020).

The example of greatest concern is the Great Pacific Garbage Patch, called the 7th continent. It is an accumulation of tens of thousands of tons of small floating plastic particles in a surface that it is about three times the size of France. From the total number of fragments, microplastics account for > 94%, the rest being plastic debris with larger dimension over 5 mm (Lebreton et al., 2018; Toussaint et al., 2019) .

It has been recently stated that the main plastic producing corporations are also responsible for large contributors to greenhouse gas emissions. Incidentally, several hundreds of organizations from 76 countries have recently signed a public addressed to the delegates attending COP26 to demand a deep change that overcomes the dependency on fossil fuels and fossil-derived plastic production by making investments in circular economy alternatives (https://es.weforum.org/events/forum-cop26-live-2021).

The recent joint workshop report by Intergovernmental Science-Policy Platform on Biodiversity and Ecosystem Services and Intergovernmental Panel on Climate Change stated that it will be impossible to address the current global threats posed by biodiversity loss and climate change if a joint effort is made by all parties involved (IPBES-IPCC workshop report, 2021). It is essential to embrace the idea that nature-

based solutions are required to meet the current global threats (Pörtner et al., 2021; Smith et al., 2021).

The data show that near 30 million tonnes of plastics waste are generated every year in the European Union (plus Norway, United Kingdom and Switzerland, *Plastics Europe 2021*). It is also a fact that about 80% of all collected marine litter corresponds to plastic. In response to the concern on plastic pollution the regulating authorities are issuing measures to fight against the uncontrolled dissemination of plastics in the environment like the so-called single use plastics directive (Directive EU 2019/904). Taxing is another way to limit the use of unnecessary plastic. Accordingly, a plastic tax has been recently introduced in the EU as part of the Decision (EU) 2019/665 implementing the Packaging and packaging waste Directive. In addition, members and partners of Plastics Europe have launched campaigns like Gestes Prospers, BlueMed Hackathon, and EsPlásticos.

Forensic Science is the application of science to criminal and civil laws. Forensic Engineering is a subdivision that refers to the analysis of structures and products that can cause damage upon failure. More specifically, Forensic Polymer Engineering is the study of issues derived from the fabrication and use of polymeric products, which traditionally refers to the problems associated with plastics misused or not meeting design specifications. Its Environmental Forensic branch refers to the study the impact of polymers on the environment. This includes the traceability of the plastics produced by a given source with potential impact on the environment.

This Doctoral Thesis aims at studying the links between chemical, physical, and structural changes observed in plastic under the action of environmental factors and their fate, fragmentation, and potential effects as new persistent anthropogenic pollutants.

2. Micro and nano plastics

Microplastic (MP) particles are complex and diverse. EFSA Panel on Contaminants in the Food Chain (CONTAM Panel) in their statement "Presence of microplastics and nanoplastics in food, with particular focus on seafood", 2016, defines microplastics

> as a heterogeneous mixture of differently shaped materials referred to as fragments, fibres, spheroids, granules, pellets, flakes or beads, in the range of 0.1–5,000 μm, and, based on the internationally recognised definition of nanomaterials, nanoplastics can be defined as a material with any external dimension in the nanoscale or having internal structure or surface structure in the nanoscale 0.001–0.1 μm (EFSA, 2016; Shopova et al., 2020).

Some authors like Desforges (2015), Mintenig (2017), Kolandhasamy (2018), and notably the Groups of Experts on the Scientific Aspects of Marine Environmental Protection (GESAMP, 2019) proposed the use of the term to refer to plastic particles below 5 mm (and lately > 1 μm). MPs can be either primary or secondary. Primary MPs are manufactured in that specific size for applications like cosmetics or agriculture, while; secondary MPs come from the breakdown of larger plastic fragments or fibers (OSPAR, 2017). Other authors develop their research using a certain fraction of microplastics: 1 mm – 5 mm (Edo et al., 2019), 0.33 mm-5 mm (Masura et al., 2015), 1 μm–5 mm (Brander et al., 2020), 0.1 μm-5 mm (Prüst et al., 2020), or use microplastics term without a strict definition (Aragaw, 2020).

Gigault (2018) define nanoplastics as "particles unintentionally produced (e.g., from the degradation and the manufacturing of the plastic objects) within the size range from 1 to 1000 nm" (Gigault et al., 2018) and presenting a colloidal behaviour. A bibliometric analysis performed by Wang et al. 2021 about the recent research concerning nanoplastics and published in a wide range of specialized journals, found a substantial growth from a few publications per year in 2004 to several hundred in 2020, reflecting the evidence on their toxicity to the environment in general and the human being in particular (J. Wang et al., 2021). In what follows, we will consider nanoplastics the secondary fragments produced from plastic items with larger dimension < 1 μm (Gigault

et al., 2018; Sorasan et al., 2022). MPs as particles smaller than 5 mm. That is the most accepted classification of sizes and with greater presence in the most recent scientific articles, classification that we have used in this work. Microplastics will refer to particles smaller than 5 mm, following the generally accepted classification (GESAMP, 2019).

3. From microplastics to nano plastics

Microplastics have been found in all variety of environments, including air (Gasperi et al., 2018), soil (Guo et al., 2020), and water (Mateos-Cárdenas et al., 2020; Picó & Barceló, 2019). In their receiving compartments, microplastics are suspected to cause toxic effects due to mechanical damage, the generation of smaller particles, and their own chemical load (C. Wang et al., 2021).

MPs/NPs pollution is a great challenge for humanity in the near future. It is especially important to supply sufficient tools for its assessment and control. The way MPs lead to NPs under environmental conditions is a particularly difficult task due to the lack of analytical and conceptual tools. Many studies proved that MPs/NPs are everywhere, and it has been shown that a variety of complex physical, mechanical, chemical, and biological processes are involved in the environmental fate of MPs/NPs. However, the scientific community is quickly advancing towards the understanding of the problem and the methods for its control.

This work focuses on the study of UV radiation, air, and water on the wear and fracture processes of MPs leading to the creation of smaller MPs and NPs used three different LDPE in the ultrapure water: Chapter 1 "**Generation of nanoplastics during the photoageing of low-density polyethylene**" (*published in Journal Environmental Pollution, 289, November 2021),* the results showed that one gram of LDPE generated up to 10^{10} NPs, and 10^{4}- 10^{5} MPs in the 1-25 μm; real marine microplastics: Champer 2 "**Ageing and fragmentation of marine microplastics**" (*published in Journal Science of The Total Environment, 827, June 2022)*, the results demonstrate that marine debris give rise to a very high number of MPs in the few microns range (< 2μm), which reached

10^5- 10^6items/mg of plastic and 10^{11}-10^{13} NPs/g with NPs mostly forming aggregates of a few hundred of nanometres; Chapter 3 "**Modelling the photodegradation of marine microplastics by means of infrared spectrometry and chemometric techniques**" (*published in Journal Microplastics, 198-210, March 2022)*, the results demonstrated that the cheap, fast and non-destructive test using mid-IR spectroscopy provides spectra that allows investigation the structural and changes suffered by plastics undergoing accelerated ageing, and using the Orthogonal Partial Least Squares Discrimination Analysis (OPLS-DA) models is possible automate an endless analysis.

References

Aragaw, T. A. (2020). Surgical face masks as a potential source for microplastic pollution in the COVID-19 scenario. *Marine Pollution Bulletin*, *159*, 111517. https://doi.org/10.1016/J.MARPOLBUL.2020.111517

Brander, S. M., Renick, V. C., Foley, M. M., Steele, C., Woo, M., Lusher, A., Carr, S., Helm, P., Box, C., Cherniak, S., Andrews, R. C., & Rochman, C. M. (2020). Sampling and Quality Assurance and Quality Control: A Guide for Scientists Investigating the Occurrence of Microplastics Across Matrices. *Applied Spectroscopy*, *74(9)*(1099–1125), 1100–1125. https://doi.org/10.1177/0003702820945713

Desforges, J. P. W., Galbraith, M., & Ross, P. S. (2015). Ingestion of Microplastics by Zooplankton in the Northeast Pacific Ocean. *Archives of Environmental Contamination and Toxicology*, *69*(3). https://doi.org/10.1007/s00244-015-0172-5

Edo, C., Tamayo-Belda, M., Martínez-Campos, S., Martín-Betancor, K., González-Pleiter, M., Pulido-Reyes, G., García-Ruiz, C., Zapata, F., Leganés, F., Fernández-Piñas, F., & Rosal, R. (2019). Occurrence and identification of microplastics along a beach in the Biosphere Reserve of Lanzarote. *Marine Pollution Bulletin*, *143*(February), 220–227. https://doi.org/10.1016/j.marpolbul.2019.04.061

EFSA. (2016). Presence of microplastics and nanoplastics in food, with particular focus on seafood. *EFSA Journal*, *14*(6). https://doi.org/10.2903/J.EFSA.2016.4501

Gasperi, J., Wright, S. L., Dris, R., Collard, F., Mandin, C., Guerrouache, M., Langlois, V., Kelly, F. J., & Tassin, B. (2018). Microplastics in air: Are we breathing it in? *Current Opinion in Environmental Science & Health*, *1*, 1–5. https://doi.org/10.1016/J.COESH.2017.10.002

Guo, J. J., Huang, X. P., Xiang, L., Wang, Y. Z., Li, Y. W., Li, H., Cai, Q. Y., Mo, C. H., & Wong, M. H. (2020). Source, migration and toxicology of microplastics in soil. *Environment International*, *137*, 105263. https://doi.org/10.1016/J.ENVINT.2019.105263

Introduction of plastic tax in EU from 2021 on - Circular Plastics Alliance. (n.d.). Retrieved December 9, 2021, from https://circular-plastics-alliance.com/en/plastic-tax-in-eu-from-2021/

Kolandhasamy, P., Su, L., Li, J., Qu, X., Jabeen, K., & Shi, H. (2018). Adherence of microplastics to soft tissue of mussels: A novel way to uptake microplastics beyond ingestion. *Science of the Total Environment*, *610–611*, 635–640. https://doi.org/10.1016/j.scitotenv.2017.08.053

Law, K. L., Starr, N., Siegler, T. R., Jambeck, J. R., Mallos, N. J., & Leonard, G. H. (2020). The United States' contribution of plastic waste to land and ocean. *Science Advances*, *6*(44). https://doi.org/10.1126/SCIADV.ABD0288/SUPPL_FILE/ABD0288_TABLE_S6.DOCX

Lebreton, R., Slat, B., Ferrari, F., Sainte-Rose, B., Aitken, J., Marthouse, R., Hajbane, S., Cunsolo, S., Schwarz, A., Levivier, A., Nobel, K., Debeljak, P., Maral, H., & Schoeneich-Argent, A. (2018). Evidence that the Great Pacific Garbage Patch is rapidly accumulating plastic. *Scientific Reports*. https://doi.org/10.1038/s41598-018-22939-w

Masura, J., Baker, J., Foster, G., & Arthur, C. (2015). *Laboratory Methods for the Analysis of Microplastics in the Marine Environment: Recommendations for quantifying synthetic particles in waters and sediments.* https://doi.org/10.25607/OBP-604

Mateos-Cárdenas, A., O'halloran, J., Van Pelt, F. N. A. M., & Jansen, M. A. K.

(2020). *Rapid fragmentation of microplastics by the freshwater amphipod Gammarus duebeni (Lillj.)*. *10*, 12799. https://doi.org/10.1038/s41598-020-69635-2

Micro- and nanoplastics detectable in human tissues. (n.d.). American Chemical Society. Retrieved December 17, 2021, from https://phys.org/news/2020-08-micro-nanoplastics-human-tissues.html

Mintenig, S. M., Int-Veen, I., Löder, M. G. J., Primpke, S., & Gerdts, G. (2017). Identification of microplastic in effluents of waste water treatment plants using focal plane array-based micro-Fourier-transform infrared imaging. *Water Research*, *108*, 365–372. https://doi.org/10.1016/j.watres.2016.11.015

OSPAR. (2017). *Assessment document of land-based inputs of microplastics in the marine environment*.

Picó, Y., & Barceló, D. (2019). *Analysis and Prevention of Microplastics Pollution in Water: Current Perspectives and Future Directions*. https://doi.org/10.1021/acsomega.9b00222

Plastics. (n.d.). Retrieved December 6, 2021, from https://ec.europa.eu/environment/topics/plastics_en

Pörtner, H.-O., Scholes, R. J., Agard, J., Archer, E., Arneth, A., Bai, X., Barnes, D., Burrows, M., Chan, L., Cheung, W. L. (William), Diamond, S., Donatti, C., Duarte, C., Eisenhauer, N., Foden, W., Gasalla, M. A., Handa, C., Hickler, T., Hoegh-Guldberg, O., … Ngo, H. (2021). *Scientific outcome of the IPBES-IPCC co-sponsored workshop on biodiversity and climate change*. https://doi.org/10.5281/ZENODO.5101125

Prüst, M., Meijer, J., & Westerink, R. H. S. (2020). The plastic brain: neurotoxicity of micro-and nanoplastics. *Particle and Fibre Toxicology*, *17*, 1–16. https://doi.org/10.1186/s12989-020-00358-y

Shopova, S., Sieg, H., & Braeuning, A. (2020). Risk assessment and toxicological research on micro- and nanoplastics after oral exposure via food products. *EFSA Journal*, *18*(S1), e181102. https://doi.org/10.2903/J.EFSA.2020.E181102

Smith, P., Beaumont, L., Bernacchi, C. J., Byrne, M., Cheung, W., Conant, R. T., Cotrufo, F., Feng, X., Janssens, I., Jones, H., Kirschbaum, M. U. F., Kobayashi, K., LaRoche, J., Luo, Y., McKechnie, A., Penuelas, J., Piao, S., Robinson, S., Sage, R. F., … Long, S. P. (2021). Essential outcomes for COP26. *Global Change Biology*, *28*(1), 1–3. https://doi.org/10.1111/GCB.15926

Sorasan, C., Edo, C., González-Pleiter, M., Fernández-Piñas, F., Leganés, F., Rodríguez, A., & Rosal, R. (2022). Ageing and fragmentation of marine microplastics. *Science of The Total Environment*, *827*, 154438. https://doi.org/10.1016/J.SCITOTENV.2022.154438

The Sustainable Development Goals Report. (n.d.).

Toussaint, B., Raffael, B., Angers-loustau, A., Kestens, V., Petrillo, M., Rio-echevarria, I. M., Van, G., Kestens, V., Petrillo, M., Rio-echevarria, I. M., & Eede, G. Van Den. (2019). Food Additives & Contaminants : Part A Review of micro- and nanoplastic contamination in the food chain. *Food Additives & Contaminants: Part A*, *36*(5), 639–673. https://doi.org/10.1080/19440049.2019.1583381

Wang, C., Zhao, J., & Xing, B. (2021). Environmental source, fate, and toxicity of microplastics. *Journal of Hazardous Materials*, *407*, 124357. https://doi.org/10.1016/J.JHAZMAT.2020.124357

Wang, J., Zhao, X., Wu, F., Niu, L., Tang, Z., Liang, W., Zhao, T., Fang, M., Wang, H., & Wang, X. (2021). Characterization, occurrence, environmental behaviors, and risks of nanoplastics in the aquatic environment: Current status and future perspectives. *Fundamental Research*, *1*(3), 317–328. https://doi.org/10.1016/J.FMRE.2021.05.001

1 Generation of nanoplastics during the photoageing of low-density polyethylene

Abstract

In this work, we studied the hydrolytic and photochemical degradation of three low-density polyethylene (LDPE) materials, within the size range of microplastics (MP). The MPs were exposed to mechanical agitation and UV irradiation equivalent to one year of solar UVB + UVA in a stirred photoreactor. Flow cytometry was used to track the formation of small (1-25 μm) MPs by applying Mie's theory to derive the size of MP particles from scattering intensity readings. The calculation was based on a calibration with polystyrene (PS) beads. The results showed that the generation of 1-5 μm MPs reached 10^4-10^5 MPs in the 1-25 μm range per gram of LDPE. ATR-FTIR and micro-FTIR measurements showed the formation of oxygenated moieties, namely hydroxyl, carbonyl, and carbon-oxygen bonds, which increased with irradiation time. We also found evidence of the production of a high number of nanoplastics (< 1 μm, NPs). The Dynamic Light Scattering (DLS) size of secondary NPs was in the hundreds of nm range and might be up to 10^{10} NPs per gram of LDPE. Our results allowed the unambiguous spectroscopic assessment of the generation of NPs from LDPE under conditions simulating environmental exposure to UV irradiation and used flow cytometry for the first-time to track the formation of secondary MPs.

1.1 Introduction

Plastics are part of our lives since the middle of the last century. The worldwide plastic production in 2019 amounted to 368 million tonnes and the main end-use markets for plastics were packaging and building & construction standing for 39.6 % and 20.4 % respectively of the plastic demand in the European Union (EU28 plus Norway and Switzerland) according to PlasticsEurope (PlasticsEurope, 2020). Their versatility, lightness, resistance, and low cost made them unique to produce a vast variety of goods (Thompson et al., 2009). However, and despite of the efforts made to decarbonize plastic production, most plastics are produced from fossil sources and a circular economy of plastics is still far. The sector is expected to account for one fifth of the total oil consumption by 2050, standing for 15 % of the global annual carbon budget (WEF, 2016). In Europe, only 29.1 million tonnes post-consumer plastic waste was collected in 2018, 57.4 % of the total plastic demand, and from that amount, still 7.2 million tonnes were sent to landfill. The plastic waste that ends up gave in the environment is difficult to estimate because of the complexity of trade flows along the life cycle of plastics (Barrowclough et al., 2020).

When dispersed into the environment, plastics undergo ageing and transformation processes due to biotic and abiotic processes. Abiotic degradation mechanisms are the consequence of physical factors leading to cracking and fragmentation and chemical changes associated to the leaking of stabilizers and bond cleavage due to hydrolysis, oxidation, or photochemical reactions (Chamas et al., 2020). Biotic transformations are the consequence of the action of microorganisms able to use synthetic polymers as carbon source (Ru et al., 2020). The main parameter governing the environmental fate of plastics is particle size. Plastics are defined as microplastics (MPs) if their largest dimension is smaller than 5 mm (GESAMP, 2019). This boundary is clearly arbitrary and even inconsistent with the prefix “micro”. However, it has been widely accepted because of the need of preserving the existing body of information on the occurrence

and fate of MPs in many studies published with the 5 mm cut-off (GESAMP, 2015, 2016). The lower size limit of MPs is taken as 1 μm below which, the particles are referred to as nanoplastics (NPs) if they display colloidal behaviour and come from the degradation of larger plastics (Gigault et al., 2018). Ageing processes lead to the fragmentation of plastic materials into smaller particles generating the so-called secondary MPs, as opposed to some plastics specifically produced in small sizes, which are referred to as primary MPs (Koelmans et al., 2017). There are few experimental studies on the alteration of polymers in natural environments. Julienne et al. studied the artificial photodegradation of low-density polyethylene (LDPE) films and found that fragmentation was not correlated with the oxidation level, hydrolytic reactions being the main driver for cracking propagation (Julienne et al., 2019). The fragmentation of high-density polyethylene (HDPE) was studied by Kalogerakis et al. who found higher fragmentation rates on beach sand than in seawater, which was attributed to the combination of higher temperature, ultraviolet radiation, and mechanical stress due to sand abrasion (Kalogerakis et al., 2017). The weathering of plastics is usually addressed by spectroscopic techniques that identify the fingerprint of the typical moieties that appear upon hydrolysis and (photo)oxidation like hydroxyl, carbonyl, and carbon-oxygen groups. Fourier Transform Infrared (FTIR) or Raman spectroscopy have been used to identify the chemical changes produced during plastic ageing. Brandon et al. studied the changes in hydroxyl and carbon-oxygen bonds and correlated them with the time the plastics were exposed to degradation (Brandon et al., 2016). During the photodegradation of low-density polyethylene (LDPE), Hiejima et al. used Raman spectroscopy to assess an increase in crystallinity due to changes in the amorphous phase that accompanied the shrinkage and cracking of specimens (Hiejima et al., 2018).

The degradation of plastic polymers is known to produce low molecular weight fragments due to chain scission, including monomers and short-chain oligomers that would be classified as NPs, if their larger dimension is below 1 μm (Gewert et al., 2015). The occurrence and impact of NPs in natural environments have been largely discussed, but the methodological difficulties associated to their sampling make it difficult to draw

conclusions on the real risk posed by NPs. Gigault et al. provided the first data indicating that PE could be source of NPs because of UV irradiation (Gigault et al., 2016). The same group studied the presence of NPs in soil by combining separation by asymmetric flow-field flow fractionation with pyrolysis coupled to gas chromatography/mass spectrometry to demonstrate the presence of NPs from several polymers in soil (Wahl et al., 2021). The presence of NPs from the fragmentation of the microbeads used in cosmetics has also been recently assessed (Hernandez et al., 2017). Although still very incomplete, the available data confirm that NPs are part of the anthropogenic plastic litter discharged to the environment or produced during the degradation of larger particles in environmental compartments. Compared to their non-polar larger counterparts, NPs are expected to be relatively polar and more prone to interact with the biota. The toxic effect of NPs on different organisms has been reported elsewhere (Gonçalves and Bebianno, 2021; González-Pleiter et al., 2019). The higher mobility of colloidal NPs facilitates their migration through porous media and makes it possible their uptake by plants and even their internalization in tissues if they are small enough to cross epithelial barriers. Plastic leachates also contain the additives included in the formulation of commercial goods, some of which are a source of toxicity that can spread through the trophic chains (Larue et al., 2021). Finally, NPs, more than MPs due to their higher specific surface, may interact with co-contaminants like heavy metals, emerging pollutants, polycyclic aromatic hydrocarbons, and other nanoparticles, among others. Such pollutants may adsorb onto or become transformed upon interaction with NPs influencing the toxicity of their mixtures (Bhagat et al., 2021).

In this work, we studied the degradation of three LDPE materials when exposed in aqueous media to the UV radiation equivalent to one year of solar irradiance combined with mechanical agitation. The irradiation was applied using a mercury lamp covering the solar wavelength with UVA+UVB irradiance (280 to 400 nm) of 1060 W m^{-2}. We used flow cytometry to quantify the small MPs (1-25 μm) formed during the degradation of MP pellets. Besides, we obtained direct evidence for the generation of NPs during the ageing of PE materials.

1.2 Experimental section

1.2.1 Materials

The PE (CAS 9002-88-4) materials used for this research were: (1) LDPE 5 mm pellets, injection moulding grade, ET316305, supplied by Goodfellow (Coraopolis, USA); (2) laboratory LDPE flasks, manually cut into small pieces of 4-5 mm; and (3) recycled LDPE pellets (5 x 2 mm) produced from residual greenhouse film kindly supplied by Green World Compounding (Alhama de Murcia, Spain). The reason for choosing three materials was to cover all the lifecycle of LDPE, from virgin pellets to recycled LDPE coming through plastic from commercial goods. Chemical differences are expected in the presence of different additives in commercial and recycled pellets, supposedly absent in virgin pellets, marketed as additive-free. In what follows these three LDPE microplastics are referred to as LDPE-1, LDPE-2, and LDPE-3 respectively. The average weight of pellets was 0.0257 g for LDPE-1, 0.0240 g for LDPE-1 and 0.0378 for LDPE-3. Prior to the experiments, MP pellets and fragments were washed twice with HPLC grade methanol (CAS 67-56-1), and with ultrapure water (Milli-Q Q-POD® Ultrapure Water System), after which they were dried, their weight recorded, and some specimens reserved for analyses.

1.2.2 Experimental procedure

The irradiation was provided by a 150 W medium-pressure mercury lamp (Novalight TQ150) emitting in the 297-579 nm range. The emission spectrum is given in Fig. S1.1. chapter 4, Supplementary Material, SM. The irradiation experiments were conducted to mimic one year of solar radiation. The equivalence was calculated using the NASA Surface meteorology and Solar Energy database recording the monthly averaged insolation for the latitude of Madrid, which is in average 4.4 kWh m^{-2} day^{-1} (183 W m^{-}

^{2}). The average irradiance in middle point of the liquid exposed was 1060 W m^{-2} (UVB + UVA or 280-400 nm). Considering 5 % of the solar irradiance corresponds to UVA + UVB, 1 year was equivalent to approximately 3 days or 72 h of irradiation in our device. The irradiance was measured using a Modular Spectrometer System UV-Vis (StellarNet) equipped with SpectraWiz Spectrometer OS v5.33 software.

The experiments were performed in a 1 L photochemical reactor thermostated at 24 °C and magnetically stirred at 700 min^{-1} to provide homogenous exposure. The reactor was filled with 500 mL ultrapure water (Milli-Q resistivity > 10 MΩ cm, filtered 0.22 μm) and loaded with 10 % (w/v) MPs. Non-irradiated runs provided the fragmentation pattern due to hydrolysis and mechanical stress, whereas irradiation gave combined information on hydrolysis, mechanical stress, and photooxidative degradation. Additional runs were performed in the darkness and in the absence of any agitation, to clarify the role of mechanical stress in the release of secondary particles. All runs were performed at least twice, and all analyses were replicated. During the runs, samples were taken every 24 h to assess the physicochemical properties of MPs, and the generation of secondary fragments consisting of smaller MPs and NPs. The liquid was sampled by taking 25 mL aliquots from the central part of the reactor without stopping the stirrer. Additionally, five pellet particles were removed to perform spectroscopic, imaging, and mechanical studies. The samples were identified with LDPE-Plastic type-[Time]-Irradiation, where "Plastic type" was 1 (Goodfellow pellet), 2 (commercial flasks) or 3 (pellets from recycled greenhouse film); "time" corresponds to the sample (0 or initial and taken after 24, 48 and 72 h); and "irradiation" differentiates between irradiated (I) and non-irradiated (NI) runs. Non-irradiated/non-stirred runs were denoted as NI/NS. Aliquots of the samples were filtered using 1 μm pore size Puradisc 25 TF filters to separate submicron particles and dissolved material from larger MPs. Other aliquots were reserved for analyses as indicated below. A part of the final reaction mixture was filtered using 25 μm stainless steel mesh to obtain samples from the secondary MPs > 25 μm generated from the original MPs. Additionally, irradiated runs were performed in two ways. In one set of runs, the pellets were put in water stirred

and irradiated for the prescribed time (72 h, Procedure I), while in another set, the liquid obtained at the end of stirred and non-irradiated runs was further irradiated under stirring for another 72 h after withdrawing the pellets, indicated below as Procedure II.

1.2.3 Analytical procedures

Infrared spectra were acquired by means of Attenuated Total Reflectance Fourier Transform Infrared (ATR-FTIR) spectroscopy in a ThermoScientific Nicolet iS10 apparatus with a Smart iTR-Diamond module and OMNIC software in the 4000–650 cm^{-1} range with a resolution of 4 cm^{-1}. Micro-Fourier Transform Infrared Spectroscopy (micro-FTIR) was performed in a Perkin-Elmer Spotlight 200 Spectrum Two apparatus with MCT detector operating in transmission mode. The measurement procedure required individually placing the particles on KBr discs using a zircon microneedle. The resolution and spectral range were 8 cm^{-1} and 4000-550 cm^{-1} respectively. DLS measurements were performed using a Malvern Zetasizer Nano ZS instrument using backscatter detection and Non-Negative Least Squares fitting algorithm. Total Organic Carbon (TOC) was determined as Non-Purgeable Organic Carbon (NPOC), using a Shimadzu TOC-VCSH apparatus equipped with ASI-V autosampler. Differential Scanning Calorimetry (DSC) analyses were performed using a DSC/DTA/TGA Q600 module from TA Instruments with heating rate 10 °C/min. Melting temperature, T_m, was obtained from the heating curve and crystallinity from the ratio of the melting enthalpy of the sample taken the melting enthalpy of fully crystalline PE as 290 kJ/kg. The morphology of pellets before and after treatments was studied using scanning electron microscopy on gold-sputtered specimens (SEM, Zeiss DSM-950 operating at 25 kV).

1.2.4 Flow cytometry measurements

In flow cytometry, the laser light scattered from particles is recorded in forward or side scattering angles and can be used to quantify objects in the 0.5-40 μm (Primpke et al., 2020). However very few studies have used this technique to quantify MPs (Kaile et al., 2020). The main reason is that deriving size information from scatter intensities is not straightforward. Mie's scattering theory allows calculating the angular distribution of scattered light by spherical particles, but several variables like laser intensity, quantum efficiency of the detector, and user-defined variables, make difficult to handle the scattering intensities obtained as output from flow cytometers (Welsh et al., 2020). Besides, the intensity of light scattering depends not only on particle size but also on their refractive index, which is an issue if the nature of particles is unknown or if they have complex structure (Agagliate et al., 2018).

Recently, a theoretical background using Mie's theory has been provided to derive the size of extracellular vesicles from the scattering intensity based on a previous calibration with beads of known size and refractive index (de Rond et al., 2018). The calculation is based on relating forward-scattered light (FSC) or side-scattered light (SSC) to the scattering cross-section of the particle, σ_s, which represents the power scattered over the amount of power per unit area of the incident light. The procedure relates scattered intensities to particle size and refractive index and allows interconverting the intensity scattered by particles with different refractive index. A set of particles of known size and refractive index were used to calibrate the scattering intensities as read by the instrument (FSC or SSC) as follows:

1) PS latex beads of 1, 3, 4, 6, 10, 15 and 25 μm were used to derive a relationship between FSC (or SSC) and particle size (Fig. S1.2A, SM). For intermediate sizes, an interpolation allowed calculating the scattered intensity, I_{FSC} or I_{SSC}.

2) Mie's theory was used to derive scattering cross-sections for PS (n = 1.6113 at 488 nm) and LDPE (n = 1.5075 at 488 nm) as a function of size. Therefore, $(\sigma_s)_{PE}$ and $(\sigma_s)_{PS}$ can be computed for every particle size (Fig. S1.2B, SM).

3) The scaling factor that relates the measured scattering intensity to the theoretical scattering cross-section is the same for particles with different refractive index (de Rond et al., 2018). Therefore, scattering intensities are proportional to the scattering cross-section as follows:

$$\frac{(I_{FSC-SSC})_{LDPE}}{(I_{FSC-SSC})_{PS}} = \frac{(\sigma_s)_{LDPE}}{(\sigma_s)_{PS}} \quad (1)$$

$(I)_{LDPE}$ can be readily derived using Eq. 1 for any desired particle size. In other words, the scattering intensity (FSC or SSC) for LDPE can be obtained for any particle size within the calibration range. In this work we computed LDPE sizes in the 1-5 μm, and 5-25 μm ranges (as well as particles > 25 μm, which were those with scattering intensities higher than that calculated for 25 μm LDPE particles) as shown in Fig. S1.2C (SM). An example in given in Fig. S1.3 (SM) showing the tree regions indicated before. It is also apparent that a high number of particles < 1 μm existed in the sample.

The assumptions made for this calculation are that particles are spherical and homogeneous with refractive index coincident with the one reported for bulk material. For PS beads these assumptions offer no issues, but the particles produced during the photooxidative ageing of MPs are not expected to be spherical or homogeneous. In that case, the obtained diameter would be that of the equivalent sphere with the same scattering behaviour and refractive index. The water used for suspending the MP

materials was also analysed as contamination control and to subtract any possible background signal as explained below (Renner et al., 2021).

1.2.5 Nanoplastic measurements

Dynamic Light Scattering (DLS) measurements were performed to assess the presence of submicron particles in the liquid samples taken at different times and filtered using 1 μm pore size Puradisc 25 TF filters. For it, aliquots of 50 mL were taken from the liquid at the end of the runs after removing the pellets, filtered using 1 μm pore size filters, concentrated in vacuum oven at 60 °C, dissolved in xylene, and reprecipitated to obtain particles that could be inspected using micro-FTIR technique. Besides, pellets from LDPE-1, 2 & 3 were dissolved in xylene, filtrated using 1 μm pore filters, and concentrated using the same procedure until obtaining a solid deposit suitable for micro-FTIR analysis, which served to compare micro-FTIR signals from < 1 μm filtrates with spectra representative of the bulk composition of the pellets, not only the outer layer accessible to ATR-FTIR.

1.3 Results and discussion

1.3.1 Effects on microplastic fragments

The ATR-FTIR spectra of LDPE pellets showing the typical peaks of PE spectrum are presented in Fig. S1.4. (SM). The main peaks corresponded to the stretching vibrations of -CH_2 at 2920 cm^{-1} and 2846 cm^{-1}, the bending mode of the -CH_2 between 1474 cm^{-1} and 1460 cm^{-1} (in the lower range for LDPE). The bending of -CH_3 terminal groups appeared around 1370 cm^{-1} and is visible only in LDPE (absent in HDPE). The -CH_2 rocking vibration in amorphous and crystalline domains, respectively was clear at 719 cm^{-1} and 729 cm^{-1} (Hamzah et al., 2018). Besides, the carbonyl stretching vibration visible in LDPE-2 & 3 at 1715-1735 cm^{-1}, reflected some degree of degradation of laboratory LDPE flasks and the pellets made from recycled LDPE.

Degradation indexes quantifying the presence of hydroxyl (HO), carbonyl (C=O), and carbon-oxygen bonds (C-O) have been calculated as the ratio of peak(s) height, expressed as absorbance, to the height of a reference peak, both from corrected baseline. The reference taken in this work was the 2920 cm^{-1} main stretching vibration of -CH_2, that has been shown to be relatively insensitive to polymer ageing (Brandon et al., 2016). The bands generally selected for hydroxyl, carbonyl, and carbon-oxygen bonds are 3200-3500 cm^{-1}, 1550-1810 cm^{-1} and 1000-1200 cm^{-1} respectively. The presence of carbonyl bands is particularly relevant. The photochemical degradation of PE is known to proceed through various steps, beginning by the formation of ketones followed by carboxylic acids, esters, and lactones at wavenumbers in the 1713-1780 cm^{-1} range (Gardette et al., 2013). We took for carbonyl index, the highest peak in that area. For the quantification of carbon-oxygen bonds, we used the peaks at 1160 cm^{-1} and 1230 cm^{-1} attributed to C-O-C and C-O stretching vibrations.

Table 1.1. shows the evolution of the three degradation indexes (OH, C=O and C-O) for pellets taken at different times and for fragments recovered in 25 μm filters at the end of the runs. All indexes, calculated as average of at least three readings on different specimens from at least two experiments, displayed a tendency to increase with the time in contact with water and with irradiation time. The highest values corresponded to irradiated samples and, especially, to the small MP fragments detached from pellets during the runs and recovered onto 25 μm filters. The presence of oxygenated moieties was clearly observed. These findings agree with the well-known fact that the degradation of PE initiated by oxygen in combination with light, heat or mechanical stress is mediated by oxygen-containing radicals (Zhu et al., 2018). The mechanism of photoinitiated degradation of PE is known to proceed when UV-light breaks bonds on the polymer backbone followed by propagation steps in which the newly formed radicals take oxygen to form peroxyl radicals. Propagation reactions take place via hydrogen transfer or after the formation of alkoxy radicals eventually leading to the generation of hydroxyl groups (Smith et al., 2018). Subsequent reactions result to chain scission or crosslinking with the production of oxygenated specific oxygen-containing functional groups like aliphatic carboxylic acids, aldehydes, and ketones (Gewert et al., 2015). This scenario is consistent with the facts that all degradation indexes increased with time and that C-O index did not reach high values for some irradiated runs. In the absence of UV radiation, heat and mechanical also lead to the formation of oxygenated moieties that also increase the rate of hydrolysis like carbonyl bonds, which are hydrolytically susceptible. Besides, the initial formation of reactive moieties may take place during processing or manipulation and is most probably the reason for the relatively high oxidation indexes observed for LDPE-3-[0].

Table 1.1. *Hydroxyl (HO), carbonyl (C=O), and carbon-oxygen bond (C-O) indexes calculated from ATR-FTIR and micro-FTIR, melting temperature (T_m), and crystallinity (X) from DSC data. (Values are given with standard deviation; NS: Not significantly different from zero.)*

	HO index	C=O index	C-O index	T_m (°C)	*X*(%)
Pellets (ATR-FTIR)					
LDPE-1-[0]	-	-	-	117.8 ± 0.2	44.0 ± 0.8
LDPE-1-[24]-NI	NS	NS	0.109 ± 0.018	117.1 ± 0.3	48.1 ± 0.6
LDPE-1-[48]-NI	NS	NS	0.276 ± 0.022	115.5 ± 0.2	47.9 ± 0.5
LDPE-1-[72]-NI	NS	0.016 ± 0.009	0.452 ± 0.031	110.9 ± 0.4	44.6 ± 1.2
LDPE-1-[24]-I	NS	NS	0.184 ± 0.014	116.3 ± 0.5	45.0 ± 0.9
LDPE-1-[48]-I	NS	0.017 ± 0.011	0.273 ± 0.023	116.0 ± 0.3	46.9 ± 1.4
LDPE-1-[72]-I	0.010 ± 0.008	0.023 ± 0.014	0.289 ± 0.027	114.0 ± 0.4	49.7 ± 1.6
LDPE-2-[0]	0.012 ± 0.007	NS	0.025 ± 0.016	110.9 ± 0.4	45.4 ± 0.8
LDPE-2-[24]-NI	0.009 ± 0.005	NS	0.057 ± 0.021	110.2 ± 0.3	41.0 ± 1.1
LDPE-2-[48]-NI	NS	0.017 ± 0.011	0.173 ± 0.014	109.8 ± 0.3	40.2 ± 0.9
LDPE-2-[72]-NI	NS	0.026 ± 0.015	0.290 ± 0.023	107.9 ± 0.5	40.0 ± 1.3
LDPE-2-[24]-I	0.018 ± 0.010	NS	0.146 ± 0.017	108.8 ± 0.1	39.8 ± 1.5
LDPE-2-[48]-I	0.014 ± 0.008	0.016 ± 0.009	0.255 ± 0.020	108.0 ± 0.2	40.4 ± 1.4
LDPE-2-[72]-I	0.015 ± 0.011	0.022 ± 0.012	0.289 ± 0.021	107.9 ± 0.4	40.7 ± 0.9
LDPE-3-[0]	NS	0.070 ± 0.017	0.093 ± 0.031	117.0 ± 0.2	40.1 ± 0.6
LDPE-3-[24]-NI	0.016 ± 0.012	0.075 ± 0.032	0.166 ± 0.027	115.5 ± 0.3	40.6 ± 0.8
LDPE-3-[48]-NI	0.025 ± 0.010	0.080 ± 0.012	0.411 ± 0.051	114.8 ± 0.2	39.6 ± 1.1
LDPE-3-[72]-NI	0.038 ± 0.008	0.097 ± 0.016	0.462 ± 0.034	113.3 ± 0.4	39.1 ± 2.3
LDPE-3-[24]-I	0.012 ± 0.009	0.067 ± 0.021	0.113 ± 0.022	115.5 ± 0.3	38.6 ± 1.8
LDPE-3-[48]-I	0.022 ± 0.014	0.076 ± 0.008	0.141 ± 0.008	115.5 ± 0.3	39.5 ± 1.4
LDPE-3-[72]-I	0.041 ± 0.018	0.092 ± 0.015	0.281 ± 0.016	113.3 ± 0.4	40.0 ± 1.9

Small fragments (> 25 μm, micro-FTIR)					
LDPE-1-[72]-NI	NS	0.009 ± 0.007	0.137 ± 0.029	-	-
LDPE-1-[72]-I	0.028 ± 0.008	0.031 ± 0.011	0.353 ± 0.024	-	-
LDPE-2-[72]-NI	0.039 ± 0.014	0.098 ± 0.026	0.115 ± 0.057	-	-
LDPE-2-[72]-I	0.124 ± 0.021	0.170 ± 0.032	0.308 ± 0.062	-	-
LDPE-3-[72]-NI	0.076 ± 0.024	0.118 ± 0.028	0.074 ± 0.025	-	-
LDPE-3-[72]-I	0.152 ± 0.038	0.312 ± 0.051	0.476 ± 0.054	-	-

Fig. 1.1. shows the micro-FTIR spectra of small MPs detached from the pellets with all bands corresponding to oxygenated moieties clearly visible. Higher degradation was observed for small fragments in comparison with pellets because small MPs are more prone to undergo hydrolytic and photooxidative reactions and because the surface of pellets exposed after the detachment of secondary fragments should be less aged. Besides, the different technique used, transmittance micro-FTIR for small fragments, and ATR-FTIR for pellets needs to be considered. The penetration depth of ATR-FTIR depends on several factors, namely wavelength, angle of incidence, and the refractive indexes of the crystal used and the sample. Overall, the sampling depth of the method is approximately in the 2-15 μm range, higher for decreasing wavenumber (Larkin, 2011). Specifically, for the equipment used in this work, with angle of incidence 42°, diamond prism (refractive index 2.4) and for LDPE (refractive index 1.5), the penetration depth is in the range 0.5 μm (4000 cm^{-1}) to 5.0 μm (400 cm^{-1}). The relative protection of the inner parts of the plastic has been described before, as a factor to consider when using oxidation indexes to assess the weathering of plastics taken from the environment (Brandon et al., 2016). Although the comparison with other works is difficult due to the use of different reference bands and peak area instead of peak height, the results reported here are in line with those found for PE materials aged under UV- or Xe-arc light (Gulmine et al., 2003; Stark and Matuana, 2004). Fig. S1.5. (SM) shows

images of small MPs fragments recovered on 25 µm filters from which micro-FTIR spectra were recorded.

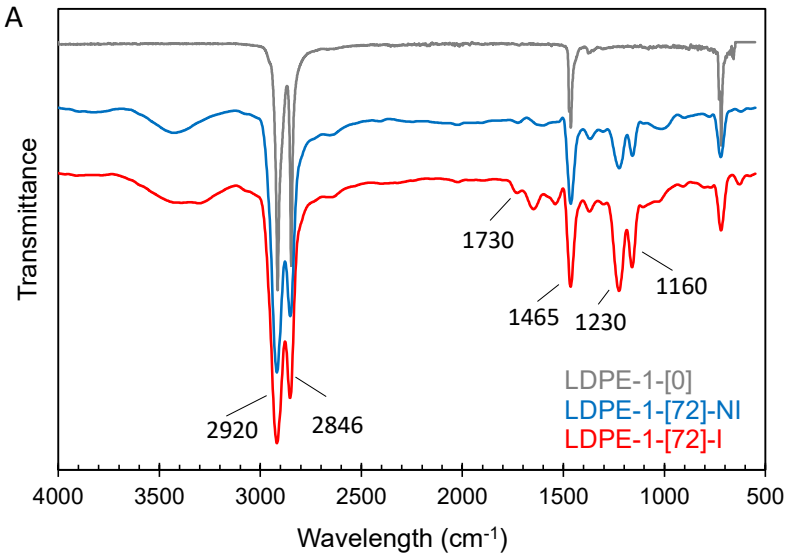

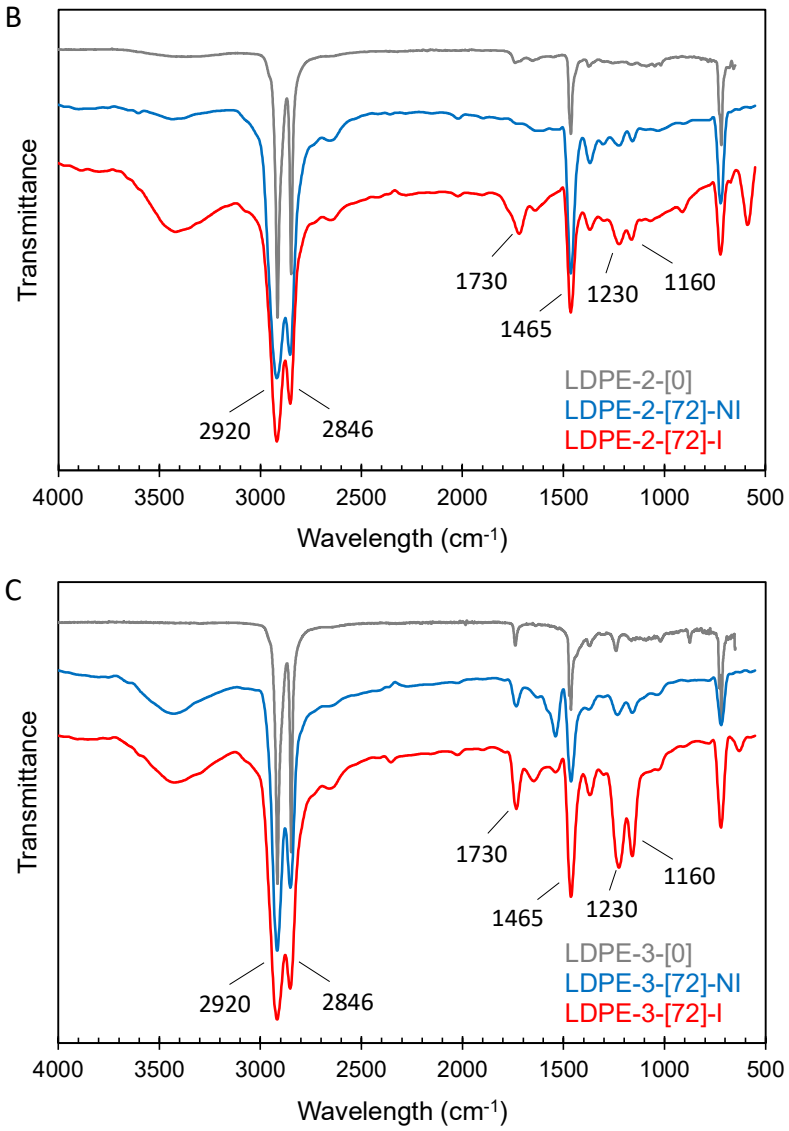

Figure 1.1. *Micro-FTIR spectra for the fragments retained by 25 μm filters indicating the main peaks used for the calculations shown in Table 1.1. The spectra of the original materials LDPE-1 (A), 2 (B) & 3 (C) are also shown.*

Table 1.1 also shows melting temperature, T_m, and the degree of crystallinity of pellets taken at different times from DSC measurements. Melting temperature showed a slight tendency to decrease with lowest values at the end of the runs, which could be explained by the increase in crystal defects that take place during oxidative degradation upon the incorporation of oxygenated moieties, chain ends, and branching sites, all of them

originating smaller and less perfect crystals (Ojeda et al., 2011). Crystallinity, however displayed little changes with a certain tendency to increase upon irradiation. It has been shown that UV irradiation generates bulkier oxygen-containing groups that increase interchain distance, therefore decreasing crystallinity. However, the structural modifications occurring during PE ageing are complex and some factors lead to a crystallinity increase and others to the opposite (Carrasco et al., 2001). The limited usefulness of crystallinity to assess PE ageing agrees with data reported elsewhere (Brandon et al., 2016). DSC plots are given in Fig. S1.6. (SM).

1.3.2 Fragmentation into smaller microplastics

In the environment, MPs undergo fragmentation processes that release smaller plastic fragments. While photodegradation has been considered the principal formation pathway for the degradation of plastics in the environment, other studies suggested that mechanical and even biological fragmentation may play a significant role. Recent evidence was provided that Antarctic krill, through their digestive system, could be fragmentating PE microbeads into smaller fragments (Dawson et al., 2018). The combination of oxidative degradation with mechanical stress was studied for expanded polystyrene (EPS) in laboratory simulations that included the nanoplastic size fraction measured by nanoparticle tracking analysis. The study concluded that mechanical fragmentation is an important environmental process leading to the formation of secondary particles, even nanoparticles in the few hundred of nanometers range (Mattsson et al., 2021). It has also been shown that polyester synthetic fibers undergo degradation and fragmentation due to a combination of photooxidation and mechanical abrasion, possibly with degradation being UV-initiated (Sørensen et al., 2021). Overall, the fragmentation of MPs is a complex process that could be attributed to the combined action of tensile stresses and the loss of mechanical properties due to polymer hydrolysis and photodegradation (ter Halle et al., 2016). Wahl et al. demonstrated the plastic degradation including the generation of NPs can take place in soil suggesting the implication of mechanisms different from photooxidative processes (Wahl et al., 2021).

Accelerated weathering experiments combining UV exposure with mechanical abrasion showed that polyolefins were fragmented mainly due to UV irradiation, which resulted in thousands of particles per pellet after prolonged exposure, while EPS was more affected by mechanical fragmentation (Song et al., 2017).

The ageing of polymers most probably begins by an alteration of the outer surface that leads to crack formation and propagation (Zhang et al., 2021). The SEM images of LDPE-1, 2 & 3 pellets in irradiated and non-irradiated runs showed the appearance of surface cracks and irregularities that most probably resulted in the detaching of fragments from the outer surface (Fig. S1.7, SM). Fig. 2 presents the number of particles in the 1-5 μm, 5-25 μm and > 25 μm ranges obtained from flow cytometry measurements as explained before and expressed per unit mass of exposed LDPE. In all cases, the background from ultrapure water was subtracted to account for possible particles driven by the MilliQ water, which represented in all cases a very minor number of particles. The results showed a high number of particles in the lower size range, with values in the tens of secondary MPs per mg of PE. It is interesting to point out that this size range, as low as 1 μm, is lower than that reported in most studies. The limit for FTIR imaging, even improved by the focal plane array (FPA)-based technology is still in the 10 μm range, and the accuracy considerably decreases for particles < 50 μm (Simon et al., 2018; Yang et al., 2021). Raman microscopy allows approaching the lower limit of MPs, in the few microns range, but the technique has important drawbacks like long measurement time and difficulty to process samples with fluorescence, which appears in most polymers (Araujo et al., 2018). Therefore, there are very limited evidence on the occurrence of small MPs in the environment, although different studies demonstrated that small MPs are much more abundant than larger fragments (Eo et al., 2018; Missawi et al., 2020).

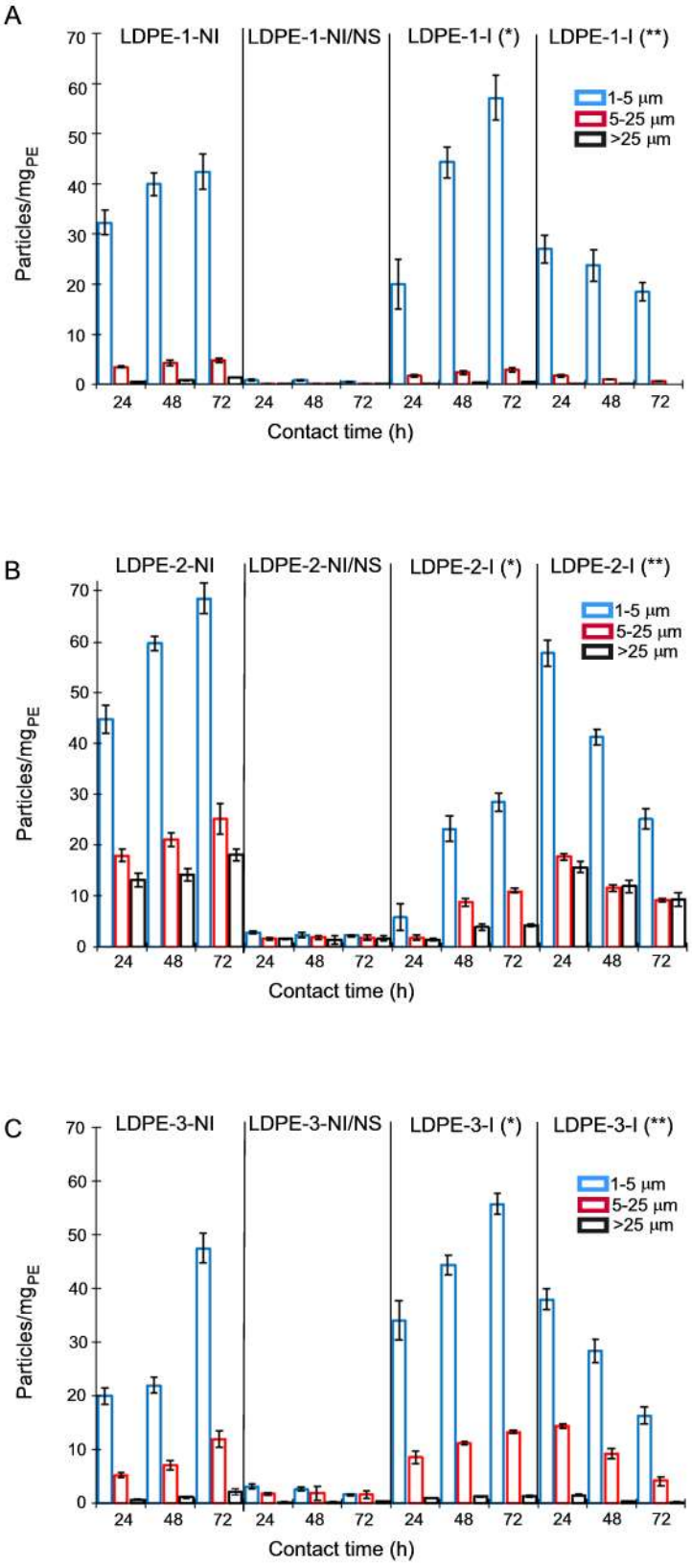

Figure 1.2. *Particle size distribution obtained from flow cytometry experiments with LDPE-1 (A), LDPE-2 (B) and LDPE-3 (C). One asterisk (*) means Procedure I: samples*

irradiated and stirred for 72 h in the presence of pellets; two asterisks (**) mean Procedure II: samples irradiated and stirred for 72 h without pellets after 72 h in water in darkness with pellets. NI/NS refers to non-irradiated/non-stirred samples.

The results showed that mechanical stress played an important role in the detachment of secondary MP particles. The number of MPs produced in the absence of agitation (NI/NS runs) was very low, in the order of units of MP/mg PE, that appeared at the beginning of the experiments and remained with little changes during the 72 h runs. These were most probably particles coming from an already altered surface that detached form larger pellets and fragments upon swelling after water immersion. The results also showed that the number of small MPs particles formed during the weathering of plastic pellets, decreased when exposed to UV light in the absence of the parent LDPE particles. This finding is clear observing the results from Procedure II, which is a continuation of non-irradiated runs for additional three-day periods after removing the pellets (Figure 1.2 experiments marked as Procedure II). This phenomenon affected all particle sizes and suggested that particles < 1 μm were produced during the irradiation of the MPs released during the previous 72 h stirred in darkness (as suggested by flow cytometry plots like the one showed in Fig. S1.3, SM). Besides, in irradiated runs with pellets, the number of fragments in the 5-25 μm range and > 25 μm tended to increase with time. However, in runs for which pellets were removed before irradiation all size ranges decreased, suggesting that UV irradiation is key for the ripping of MP into smaller particles and NPs. It was also noticeable that many small MPs appeared during the first 24 h, showing that the onset of fragmentation is rapid and does not require extensive photooxidation of the polymer surface. This phenomenon is probably due to the plasticizer effect of water (Julienne et al., 2019). The higher number of small MPs produced from LDPE-2 might be due to their higher external surface, 2210 mm^2/g, 15-20 % higher that LDPE-1/3 pellets. The higher generation of small MPs in the case of LDPE-2 was in line with the reduction in the concentration of 1-5 μm fragments when removing the pellets from the reactor. The reason is probably the ongoing degradation of larger particles, including those > 25 μm

like those shown in Fig. S1.5. Overall, and considering all LDPE materials, the small MPs in the 1-25 μm range, quantified by flow cytometry were in the 10^6-10^7 MPs/L range, or, expressed per unit mass of polymer, 10^4-10^5 MPs/g_{PE}, which represented in all cases < 0.01 % of the exposed polymer.

1.3.3 Generation of nanoplastics

The fragmentation of plastic particles does not limit to micron size particles. Little is known about the lower sizes, because of the lack of established analytical methods able to detect them in the environment (Koelmans et al., 2015). In the absence of field data, laboratory studies showed that environmental factors led to the production of nanosized plastic particles (Rios Mendoza et al., 2018; Song et al., 2020). Gigault et al. used a photoreactor emitting UVA + UVB with irradiance 1000 W m^{-2}, essentially the same used in this work, to demonstrate de the formation of NPs from the degradation of marine microplastics. The results, obtained using DLS and TEM for particle characterization, suggested that the smaller NP particles were produced after the initial formation of larger plastic particles (Gigault et al., 2016). In our runs, DLS measurements in the liquid samples taken at different times showed the presence of colloidal submicron particles as indicated in Table 1.2 DLS plots for samples irradiated for 72 h are shown in Fig. S1.8 (SM). Clear peaks in the few hundreds of nm appeared in all DLS plots with a slight tendency to size decrease with time and larger nanoparticles in irradiated samples. This was probably due to the higher input of newly formed nanoparticles, but this assumption must be handled with care because of the limited sensitivity of DLS in the case of polydisperse colloids. As in the case of larger secondary MPs, no aggregation pattern was observed, with stable DLS particle size even when repeating the measurement days after the run. Table 2 also shows the TOC of samples, filtered through 1 μm filters, and without filtration. In all cases, the organic carbon content was higher in irradiated samples and increased with time as expected from the role of UV irradiation in the photodegradation of polymers. As for the

generation of secondary MPs, the release of organic matter was not linear with time, reflecting an early generation of NPs, which is probably related to the presence of surface defects or reactive moieties originated during the processing of storage of pellets.

Table 1.2. *TOC of samples filtered through 1 μm pore size filters and non-filtered (the numbers in brackets represents the concentration of LDPE with the same carbon content); DLS particles size from samples filtered through 1 μm filters.*

		Non-Filtered	Filtered < 1 μm	
		TOC (mg/L)	TOC (mg/L)	DLS Particle size (nm)
Non-irradiated (darkness)	LDPE-1-[24]-NI	1.9 (2.2) ± 0.2	-	258 ± 11
	LDPE-1-[48]-NI	2.1 (2.5) ± 0.3	-	231 ± 14
	LDPE-1-[72]-NI	2.3 (2.7) ± 0.2	1.7 (2.0) ± 0.2	220 ± 12
	LDPE-2-[24]-NI	5.5 (6.4) ± 2.1	-	244 ± 22
	LDPE-2-[48]-NI	7.4 (8.6) ± 2.2	-	242 ± 13
	LDPE-2-[72]-NI	9.2 (10.7) ± 2.4	5.0 (5.8) ± 2.2	142 ± 15
	LDPE-3-[24]-NI	2.4 (2.8) ± 0.5	-	200 ± 24
	LDPE-3-[48]-NI	3.2 (3.7) ± 0.7	-	165 ± 12
	LDPE-3-[72]-NI	3.6 (4.2) ± 0.5	2.7 (3.2) ± 0.7	158 ± 17
Irradiated	LDPE-1-[24]-I	16.2 (18.9) ± 2.1	-	416 ± 20
	LDPE-1-[48]-I	18.2 (21.2) ± 3.2	-	371 ± 16
	LDPE-1-[72]-I	20.5 (23.9) ± 2.2	18.9 (22.1) ± 2.5	328 ± 19
	LDPE-2-[24]-I	24.3 (28.4) ± 5.2	-	636 ± 92
			-	104 ± 17
	LDPE-2-[48]-I	34.6 (40.4) ± 6.1	-	307 ± 17
	LDPE-2-[72]-I	39.6 (46.2) ± 4.2	38.5 (44.9) ± 7.8	279 ± 14

	LDPE-3-[24]-I	6.2 (7.2) ± 1.3	-	192 ± 42
	LDPE-3-[48]-I	7.7 (9.0) ± 1.5	-	167 ± 23
	LDPE-3-[72]-I	8.8 (10.3) ± 1.8	5.0 (5.8) ± 1.5	160 ± 18

The liquid concentrated form filtered aliquots taken at the end of runs was examined to assess the presence of LDPE. The extraction process described in the experimental section yielded small aggregates that could be inspected using micro-FTIR. The results are shown in Fig. 1.3 together with those of pellets dissolved and precipitated using the same procedure. In all cases the characteristics features of PE spectra were clearly observed, namely the peaks at 2920, 2846, 1465 and 719 cm^{-1} as indicated before. Besides, the spectra from LDPE-1, 2 & 3 displayed additional bands most probably due to additives, which appeared magnified in < 1 μm filtrates in irradiated and, to a lesser extent, in non-irradiated runs. Noteworthy, the N-H tensile absorption usually observed as two broad peaks in the 3300-3500 cm^{-1}, the two peaks of C-N stretching at about 1250-1020 cm^{-1}, and the N-H out of plane bending at 793 cm^{-1}, are visible in most spectra, probably indicating the presence of light stabilizers, which are usually based on secondary and tertiary hindered amines and that protect polymers against degradation by acting as free radical scavengers and peroxide decomposers (Beißmann et al., 2014). The presence of additives could be one of the factors explaining the differences among the three LDPE materials observed in this work. Table S1.1 (SM) shows the TOC for NI/NS runs, which was very low compared to the values for stirred runs listed in Table 1.2 indicating that mechanical agitation is needed to release most of the carbon containing substances released by the MPs. The presence of plastic fragments < 1 μm could not be assessed by DLS or spectroscopic analyses in NI/NS samples, indicating that, if produced, they were in very low concentration.

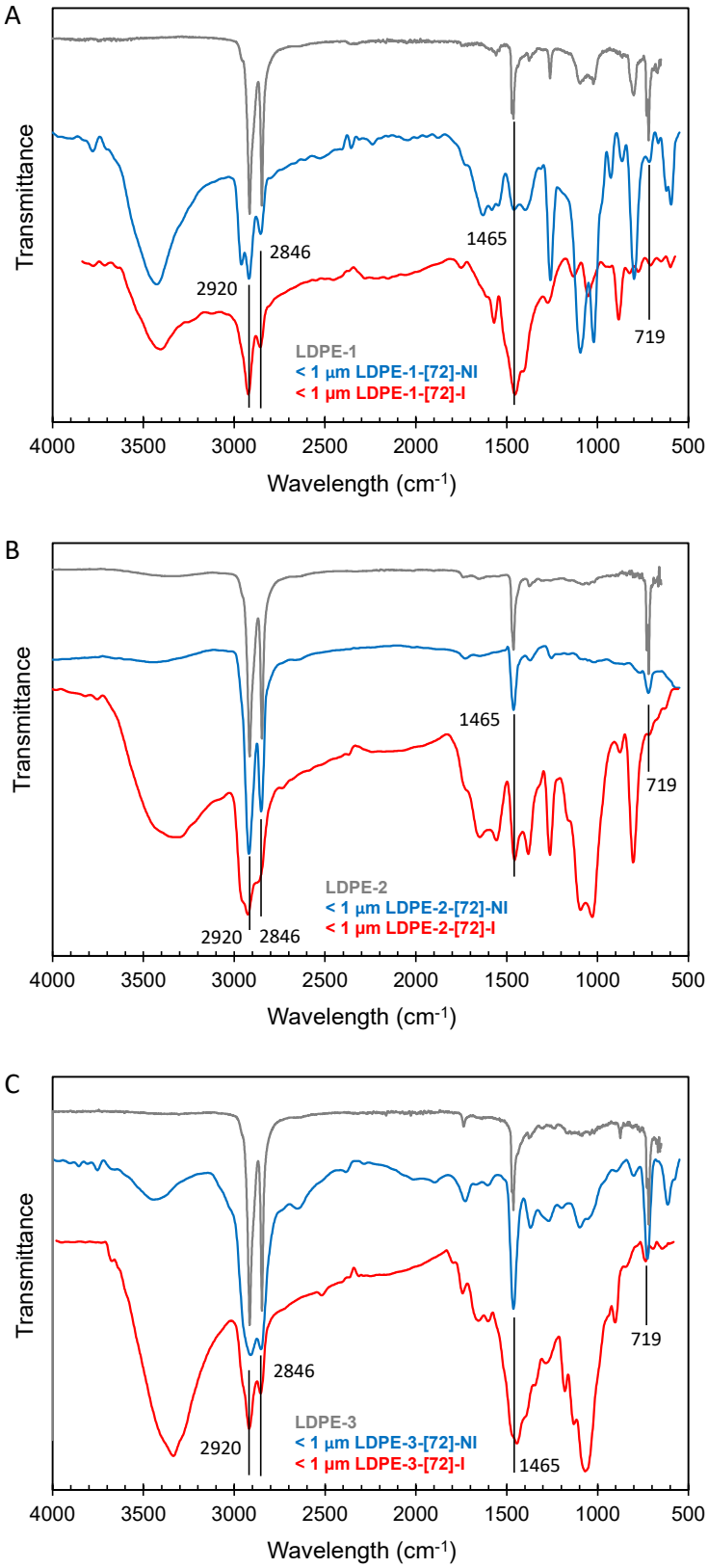
A
Transmittance
2920
2846
1465
719
LDPE-1
< 1 µm LDPE-1-[72]-NI
< 1 µm LDPE-1-[72]-I
4000
3500
3000
2500
2000
1500
1000
500
Wavelength (cm-1)
B
Transmittance
1465
719
2920
2846
LDPE-2
< 1 µm LDPE-2-[72]-NI
< 1 µm LDPE-2-[72]-I
4000
3500
3000
2500
2000
1500
1000
500
Wavelength (cm-1)
C
Transmittance
719
2846
2920
LDPE-3
< 1 µm LDPE-3-[72]-NI
< 1 µm LDPE-3-[72]-I
1465
4000
3500
3000
2500
2000
1500
1000
500
Wavelength (cm-1)

Figure 1.3 *Micro-FTIR spectra for the fragments < 1 μm filters indicating the characteristic peaks of LDPE. The spectra of the original materials LDPE-1 (A), 2 (B) and 3 (C) are also shown.*

If all organic matter consisted only of LDPE, considering the particle size given in Table 1.2 and using the density of PE, the concentration of NP particles would represent about 10^{10} NPs/g_{PE} (~0.10 % of the original mass of the pellet; this calculation assumes spherical particles with the average density of LDPE). The presence of oxidized groups in LDPE-derived NPs was clear from the peaks of carbonyl stretching vibration and other peaks attributed to carbon-oxygen bonds as explained before. This is the first evidence of the formation of NPs from PE under photooxidative conditions. Our results suggest that PE debris are disseminating huge amounts of NPs which are still very difficult or impossible to assess in real environmental matrixes.

1.4 Conclusions

In this work, we studied the hydrolytic, mechanical, and photochemical degradation of three LDPE materials exposed to the UV radiation equivalent to one year of solar UVB + UVA irradiance (280-400 nm). Flow cytometry was used for the first time to quantify the small MPs (1-25 μm) produced during the degradation of LDPE. The results showed the generation of a high number of small MPs with values reaching 10^4-10^5 MPs per gram of PE pellets in the 1-25 μm range. Mechanical degradation led to a rapid production of secondary MPs, while photochemical ageing increased the concentration of NPs (< 1 μm). FTIR studies showed clear signs of oxygenated moieties, particularly

in irradiated runs, which increased with exposure time. The presence of NPs was assessed using micro-FTIR after precipitating the colloidal fraction < 1 μm into larger particles. The size of NPs, measured by DLS, was in the hundreds of nm range, and their number could represent up to 10^{10} NPs per gram of LDPE.

1.5 Supplementary Material

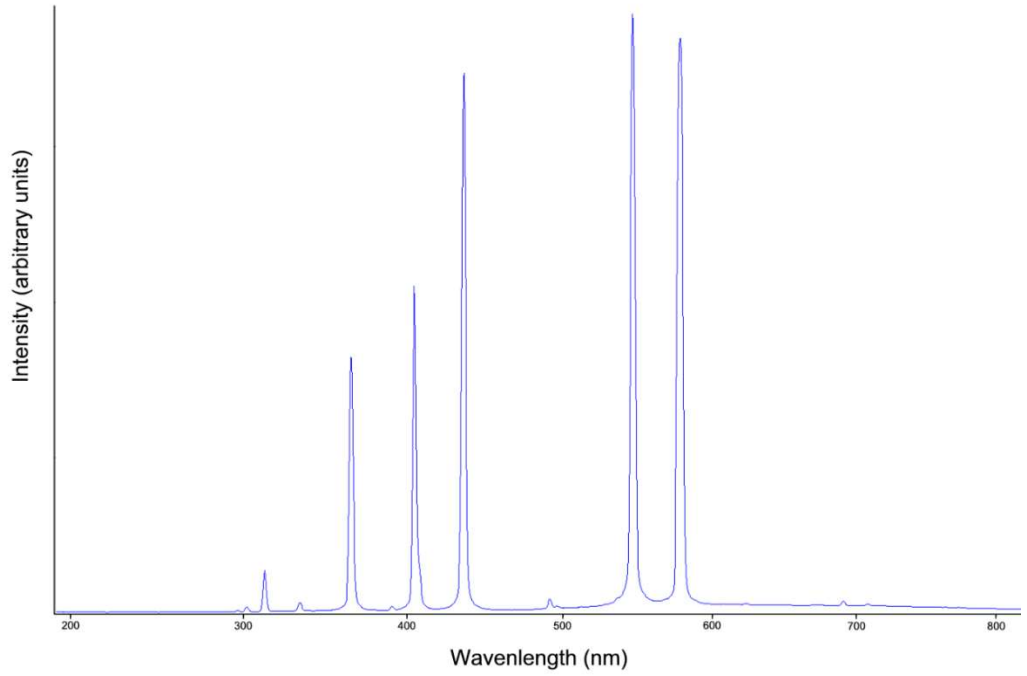

Figure S1.1. *Emission spectrum of the Hg medium pressure lamp used in this study.*

A

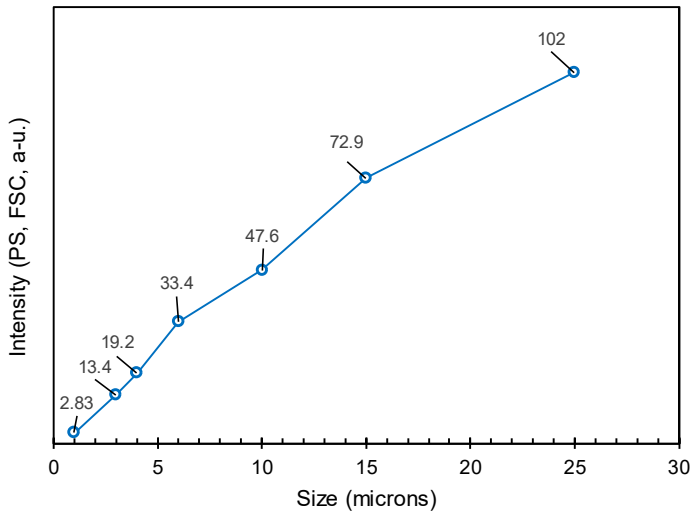
Intensity (PS, FSC, a-u.)
Size (microns)
2.83
13.4
19.2
33.4
47.6
72.9
102
0
5
10
15
20
25
30

B

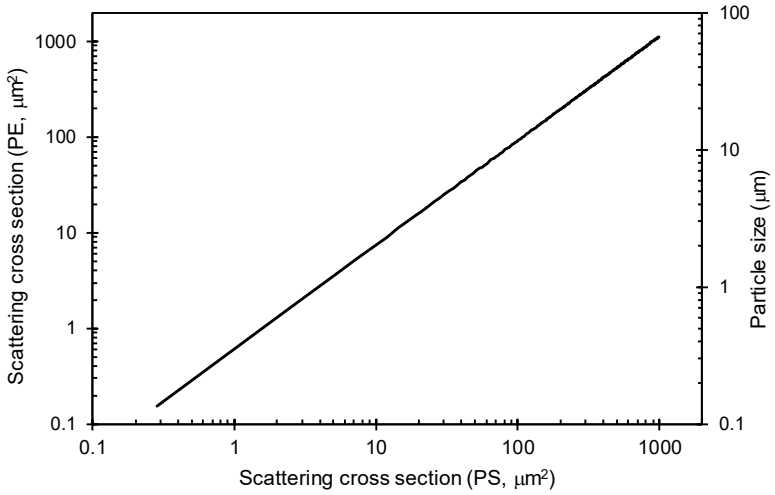
Scattering cross section (PE, µm²)
Scattering cross section (PS, µm²)
Particle size (µm)
0.1
1
10
100
1000

C

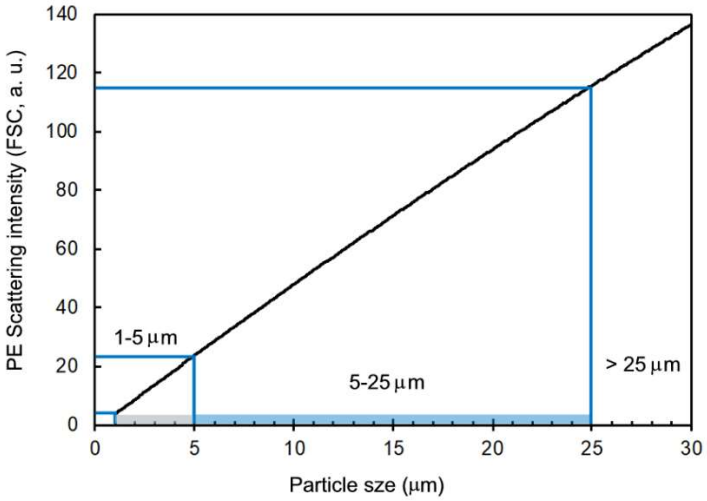
PE Scattering intensity (FSC, a. u.)
Particle size (µm)
1-5 µm
5-25 µm
> 25 µm
0
20
40
60
80
100
120
140
0
5
10
15
20
25
30

Figure S1.2. *Intensity (FSC)-size plot for the 1, 3, 4, 6, 10, 15 and 25 µm latex beads used for calibration (A); scattering cross-sections of LDPE and PS particles as a function of size according to Mie's theory (B); scattering intensities (FSC) calculated for LDPE and ranges of sizes studied in this work (C).*

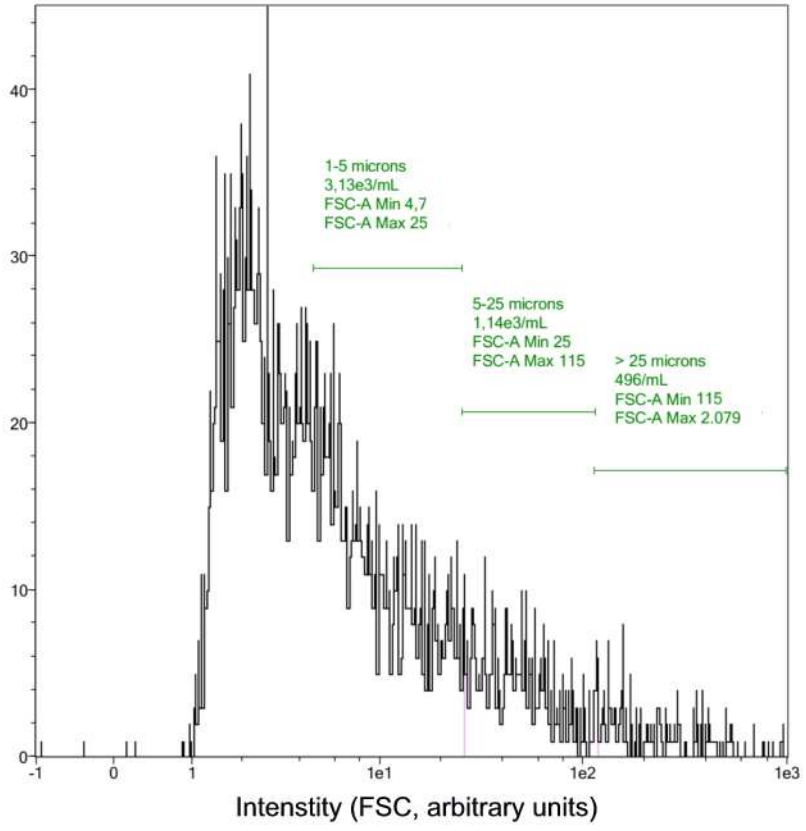

Figure S1.3. *Example of the application of the 1-5-25 µm boundaries to the plot of LDPE-2-[72]-I taken as example.*

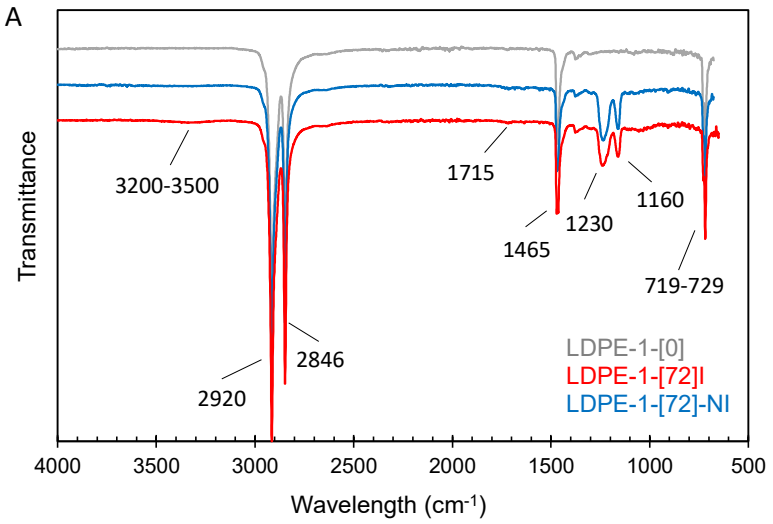
A
Transmittance
3200-3500
1715
1160
1230
1465
719-729
2846
2920
LDPE-1-[0]
LDPE-1-[72]I
LDPE-1-[72]-NI
4000
3500
3000
2500
2000
1500
1000
500
Wavelength (cm-1)

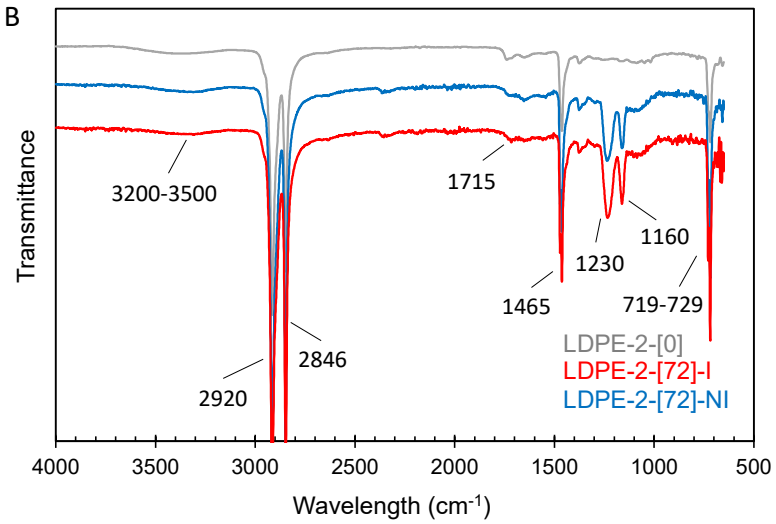
B
Transmittance
3200-3500
1715
1160
1230
1465
719-729
2846
2920
LDPE-2-[0]
LDPE-2-[72]-I
LDPE-2-[72]-NI
4000
3500
3000
2500
2000
1500
1000
500
Wavelength (cm-1)

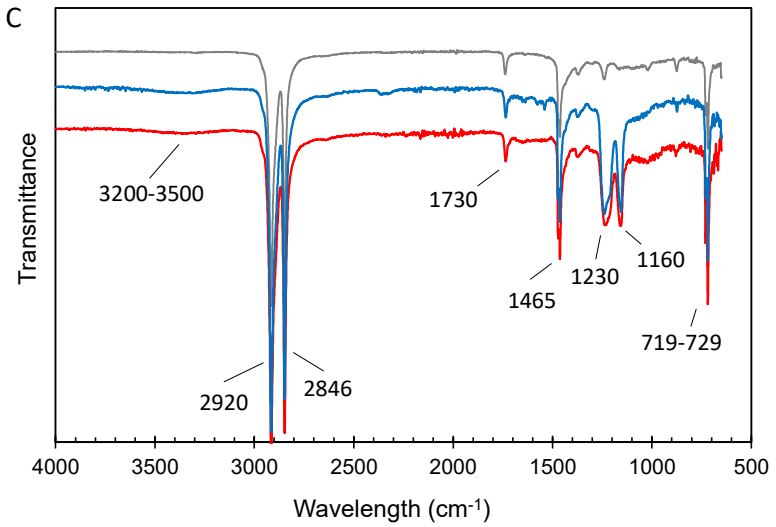
C
Transmittance
3200-3500
1730
1160
1230
1465
719-729
2846
2920
4000
3500
3000
2500
2000
1500
1000
500
Wavelength (cm-1)

Figure S1.4. *ATR-FTIR spectra for the pellets recovered after 72 h from irradiated and non-irradiated experiments: LDPE-1 (A), LDPE-2 (B) and LDPE-3 (C).*

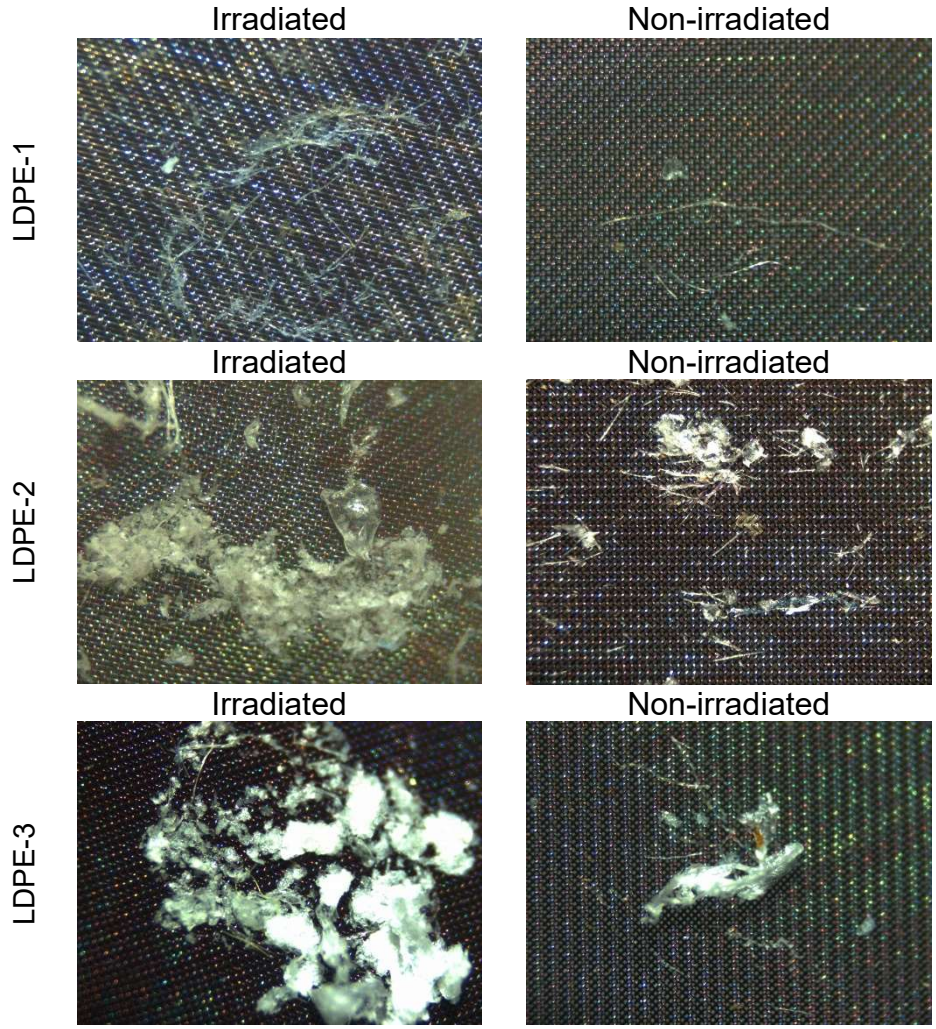

Figure S1.5. *Images of MPs fragments recovered on 25 µm stainless steel filters for samples taken after 72 h in irradiated and non-irradiated runs (LDPE-1/2/3-[72]-I/NI).*

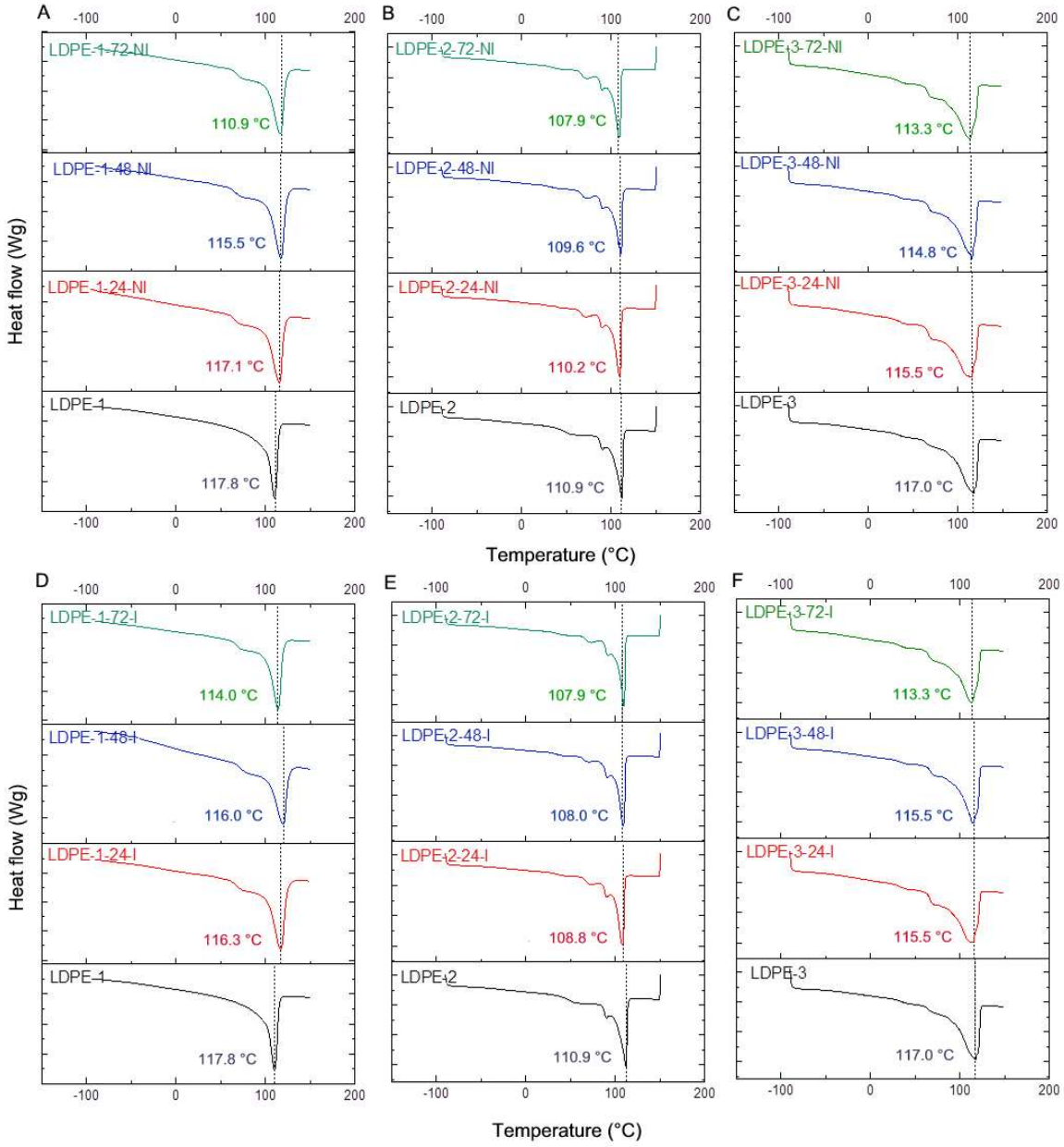

Figure S1.6. *DSC plots of LDPE specimens recovered during the runs.*

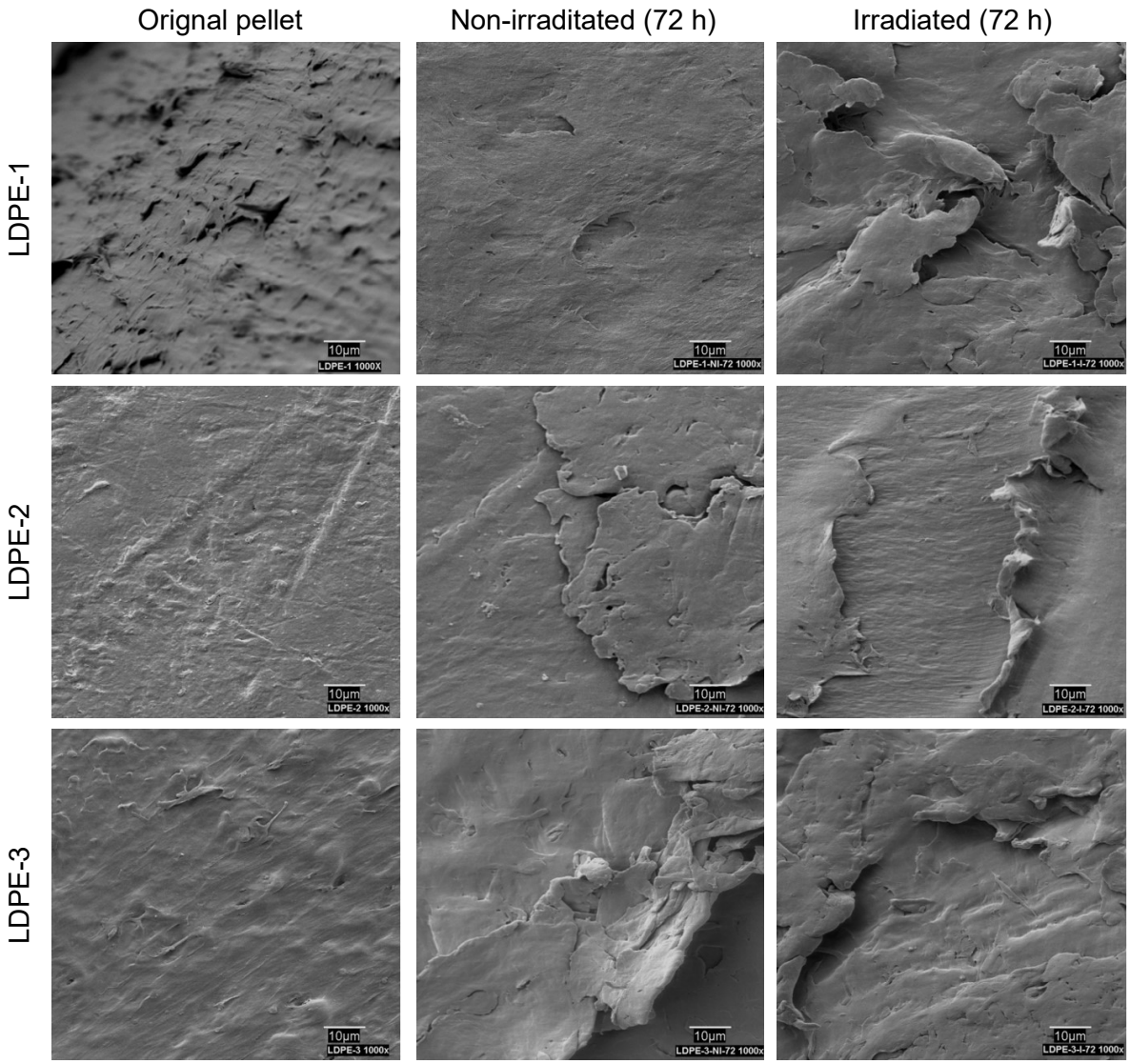

Figure S1.7. *SEM images of the surface of pellets before treatment and after 72 h in irradiated and non-irradiated runs.*

A

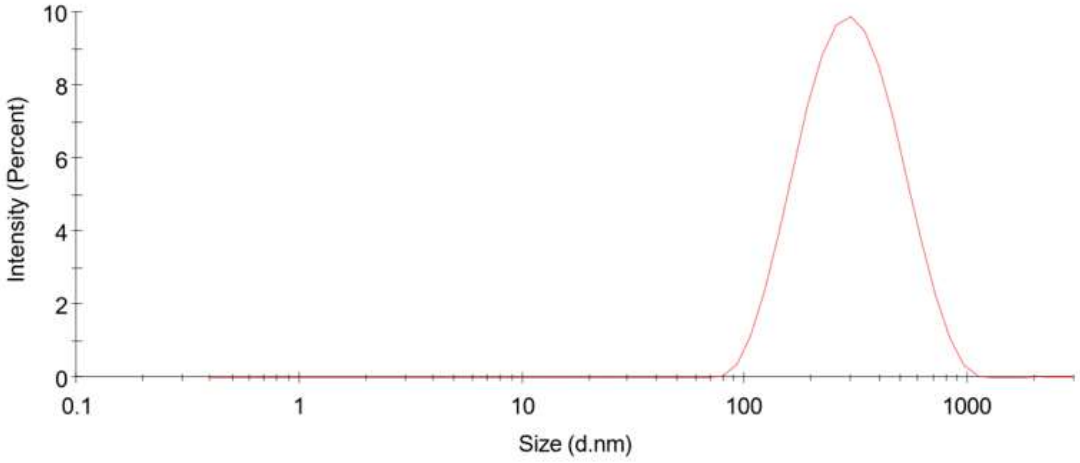
Intensity (Percent)
10
8
6
4
2
0
0.1
1
10
100
1000
Size (d.nm)

B

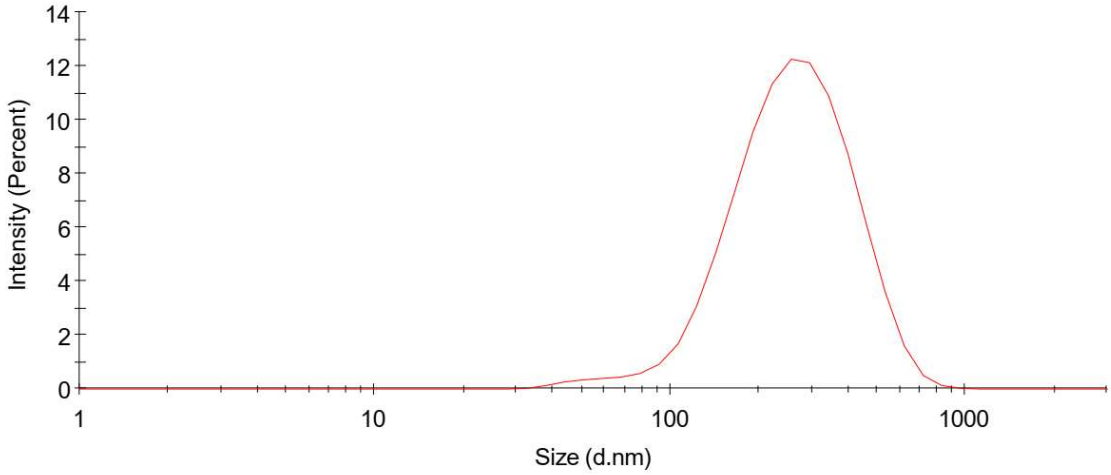
Intensity (Percent)
14
12
10
8
6
4
2
0
1
10
100
1000
Size (d.nm)

C

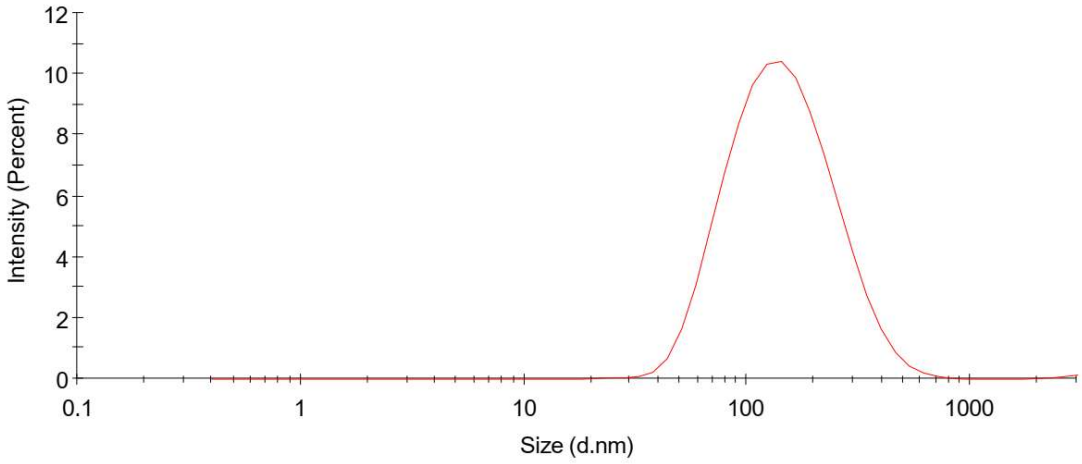
Intensity (Percent)
12
10
8
6
4
2
0
0.1
1
10
100
1000
Size (d.nm)

Figure S1.8. *DLS plot for samples LDPE-1-[72]-I (A), LDPE-2-[72]-I (B), and LDPE-3-[72]-I (C).*

Table S1.1. *TOC of samples filtered through 1 μm pore size filters from non-irradiated/non-stirred runs.*

Sample	24 h	48 h	72 h
LDPE-1-[...]-NI/NS	0.18 ± 0.13	0.37 ± 0.14	0.46 ± 0.15
LDPE-2-[...]-NI/NS	0.54 ± 0.20	0.80 ± 0.22	0.93 ± 0.17
LDPE-3-[...]-NI/NS	0.65 ± 0.12	0.93 ± 0.24	1.17 ± 0.67

1.6 References

Agagliate, J., Röttgers, R., Twardowski, M.S., McKee, D., 2018. Evaluation of a flow cytometry method to determine size and real refractive index distributions in natural marine particle populations. Appl. Opt. 57, 1705-1716. https://doi.org/10.1364/ao.57.001705.

Araujo, C.F., Nolasco, M.M., Ribeiro, A.M.P., Ribeiro-Claro, P.J.A., 2018. Identification of microplastics using Raman spectroscopy: Latest developments and future prospects. Water Res. 142, 426-440. https://doi.org/https://doi.org/10.1016/j.watres.2018.05.060.

Barrowclough, D., Birkbeck, C.D., Christen, J., 2020. Global trade in plastics: insights from the first life-cycle trade database, in: UNCTAD Research Paper No. 53, U.S.R. (Ed.). United Nations Conference on Trade and Development.

Beißmann, S., Reisinger, M., Grabmayer, K., Wallner, G., Nitsche, D., Buchberger, W., 2014. Analytical evaluation of the performance of stabilization systems for polyolefinic materials. Part I: Interactions between hindered amine light stabilizers and phenolic antioxidants. Polym. Degrad. Stab. 110, 498-508. https://doi.org/https://doi.org/10.1016/j.polymdegradstab.2014.09.020.

Bhagat, J., Nishimura, N., Shimada, Y., 2021. Toxicological interactions of microplastics/nanoplastics and environmental contaminants: Current knowledge and future perspectives. J. Hazard. Mater. 405, 123913. https://doi.org/https://doi.org/10.1016/j.jhazmat.2020.123913.

Brandon, J., Goldstein, M., Ohman, M.D., 2016. Long-term aging and degradation of microplastic particles: Comparing in situ oceanic and experimental weathering patterns. Mar. Pollut. Bull. 110, 299-308. https://doi.org/https://doi.org/10.1016/j.marpolbul.2016.06.048.

Carrasco, F., Pagès, P., Pascual, S., Colom, X., 2001. Artificial aging of high-density polyethylene by ultraviolet irradiation. Eur. Polym. J. 37, 1457-1464. https://doi.org/https://doi.org/10.1016/S0014-3057(00)00251-2.

Chamas, A., Moon, H., Zheng, J., Qiu, Y., Tabassum, T., Jang, J.H., Abu-Omar, M., Scott, S.L., Suh, S., 2020. Degradation rates of plastics in the environment. ACS

Sustainable Chem. Eng. 8, 3494-3511. https://doi.org/10.1021/acssuschemeng.9b06635.

Dawson, A.L., Kawaguchi, S., King, C.K., Townsend, K.A., King, R., Huston, W.M., Bengtson Nash, S.M., 2018. Turning microplastics into nanoplastics through digestive fragmentation by Antarctic krill. Nat. Commun. 9, 1001. https://doi.org/10.1038/s41467-018-03465-9.

de Rond, L., Coumans, F.A.W., Nieuwland, R., van Leeuwen, T.G., van der Pol, E., 2018. Deriving extracellular vesicle size from scatter intensities measured by flow cytometry. Current Protocols in Cytometry 86, e43. https://doi.org/https://doi.org/10.1002/cpcy.43.

Eo, S., Hong, S.H., Song, Y.K., Lee, J., Lee, J., Shim, W.J., 2018. Abundance, composition, and distribution of microplastics larger than 20 μm in sand beaches of South Korea. Environ. Pollut. 238, 894-902. https://doi.org/https://doi.org/10.1016/j.envpol.2018.03.096.

Gardette, M., Perthue, A., Gardette, J.-L., Janecska, T., Földes, E., Pukánszky, B., Therias, S., 2013. Photo- and thermal-oxidation of polyethylene: Comparison of mechanisms and influence of unsaturation content. Polym. Degrad. Stab. 98, 2383-2390. https://doi.org/https://doi.org/10.1016/j.polymdegradstab.2013.07.017.

GESAMP, 2015. Sources, fate and effects of microplastic in the marine environment: A global assessment (Part 1), in: Kershaw, P.J. (Ed.). IMO/FAO/UNESCO-IOC/UNIDO/WMO/IAEA/UN/UNEP/UNDP/ISA Joint Group of Experts on the Scientific Aspects of Marine Environmental Protection, p. 220.

GESAMP, 2016. Sources, fate and effects of microplastic in the marine environment: A global assessment (Part 2), in: Kershaw, P.J., Rochman, C.M. (Eds.). (IMO/FAO/UNESCO-IOC/UNIDO/WMO/IAEA/UN/UNEP/UNDP Joint Group of Experts on the Scientific Aspects of Marine Environmental Protection, p. 220.

GESAMP, 2019. Guidelines for the monitoring and assessment of plastic litter in the ocean, in: Kershaw, P.J., Turra, A., Galgani, F. (Eds.). IMO/FAO/UNESCO-IOC/UNIDO/WMO/IAEA/UN/UNEP/UNDP/ISA Joint Group of Experts on the Scientific Aspects of Marine Environmental Protection, p. 130.

Gewert, B., Plassmann, M.M., MacLeod, M., 2015. Pathways for degradation of plastic polymers floating in the marine environment. Environ. Sci. Processes Impacts 17, 1513-1521. https://doi.org/10.1039/C5EM00207A.

Gigault, J., Halle, A.t., Baudrimont, M., Pascal, P.-Y., Gauffre, F., Phi, T.-L., El Hadri, H., Grassl, B., Reynaud, S., 2018. Current opinion: What is a nanoplastic? Environ. Pollut. 235, 1030-1034. https://doi.org/https://doi.org/10.1016/j.envpol.2018.01.024.

Gigault, J., Pedrono, B., Maxit, B., Ter Halle, A., 2016. Marine plastic litter: the unanalyzed nano-fraction. Environ. Sci. Nano 3, 346-350. https://doi.org/10.1039/C6EN00008H.

Gonçalves, J.M., Bebianno, M.J., 2021. Nanoplastics impact on marine biota: A review. Environ. Pollut. 273, 116426. https://doi.org/https://doi.org/10.1016/j.envpol.2021.116426.

González-Pleiter, M., Tamayo-Belda, M., Pulido-Reyes, G., Amariei, G., Leganés, F., Rosal, R., Fernández-Piñas, F., 2019. Secondary nanoplastics released from a biodegradable microplastic severely impact freshwater environments. Environ. Sci. Nano 6, 1382-1392. https://doi.org/10.1039/C8EN01427B.

Gulmine, J.V., Janissek, P.R., Heise, H.M., Akcelrud, L., 2003. Degradation profile of polyethylene after artificial accelerated weathering. Polym. Degrad. Stab. 79, 385-397. https://doi.org/https://doi.org/10.1016/S0141-3910(02)00338-5.

Hamzah, M., Khenfouch, M., Rjeb, A., Sayouri, S., Houssaini, D., Darhouri, M., Srinivasu, V., 2018. Surface chemistry changes and microstructure evaluation of low density nanocluster polyethylene under natural weathering: a spectroscopic investigation. J. Phys. Conf. Ser. 984, 012010.

Hernandez, L.M., Yousefi, N., Tufenkji, N., 2017. Are there nanoplastics in your personal care products? Environ. Sci. Technol. Letters 4, 280-285. https://doi.org/10.1021/acs.estlett.7b00187.

Hiejima, Y., Kida, T., Takeda, K., Igarashi, T., Nitta, K.-h., 2018. Microscopic structural changes during photodegradation of low-density polyethylene detected by Raman spectroscopy. Polym. Degrad. Stab. 150, 67-72. https://doi.org/https://doi.org/10.1016/j.polymdegradstab.2018.02.010.

Julienne, F., Delorme, N., Lagarde, F., 2019. From macroplastics to microplastics: Role of water in the fragmentation of polyethylene. Chemosphere 236, 124409. https://doi.org/https://doi.org/10.1016/j.chemosphere.2019.124409.

Kaile, N., Lindivat, M., Elio, J., Thuestad, G., Crowley, Q.G., Hoell, I.A., 2020. Preliminary results from detection of microplastics in liquid samples using flow cytometry. Front. Mar. Sci. 7. https://doi.org/10.3389/fmars.2020.552688.

Kalogerakis, N., Karkanorachaki, K., Kalogerakis, G.C., Triantafyllidi, E.I., Gotsis, A.D., Partsinevelos, P., Fava, F., 2017. Microplastics generation: onset of fragmentation of polyethylene films in marine environment mesocosms. Front. Mar. Sci. 4. https://doi.org/10.3389/fmars.2017.00084.

Koelmans, A.A., Besseling, E., Shim, W., 2015. Nanoplastics in the aquatic environment. Critical review, in: Bergmann, M., Gutow, L., Klages, M. (Eds.), Marine Anthropogenic Litter, pp. 325-340.

Koelmans, A.A., Kooi, M., Law, K.L., van Sebille, E., 2017. All is not lost: deriving a top-down mass budget of plastic at sea. Environ. Res. Lett. 12, 114028. https://doi.org/10.1088/1748-9326/aa9500.

Larkin, P. Instrumentation and Sampling Methods, in: P. Larkin (Ed.) Infrared and Raman Spectroscopy, Elsevier, Oxford, 2011, pp. 27-54.

Larue, C., Sarret, G., Castillo-Michel, H., Pradas del Real, A.E., 2021. A critical review on the impacts of nanoplastics and microplastics on aquatic and terrestrial photosynthetic organisms. Small 17, 2005834. https://doi.org/https://doi.org/10.1002/smll.202005834.

Mattsson, K., Björkroth, F., Karlsson, T., Hassellöv, M., 2021. Nanofragmentation of expanded polystyrene under simulated environmental weathering (thermooxidative degradation and hydrodynamic turbulence). Front. Mar. Sci. 7. https://doi.org/10.3389/fmars.2020.578178.

Missawi, O., Bousserrhine, N., Belbekhouche, S., Zitouni, N., Alphonse, V., Boughattas, I., Banni, M., 2020. Abundance and distribution of small microplastics (≤ 3 μm) in sediments and seaworms from the Southern Mediterranean coasts and characterisation of their potential harmful effects. Environ. Pollut. 263, 114634. https://doi.org/https://doi.org/10.1016/j.envpol.2020.114634.

Ojeda, T., Freitas, A., Birck, K., Dalmolin, E., Jacques, R., Bento, F., Camargo, F., 2011. Degradability of linear polyolefins under natural weathering. Polym. Degrad. Stab. 96, 703-707. https://doi.org/https://doi.org/10.1016/j.polymdegradstab.2010.12.004.

PlasticsEurope, 2020. Plastics – the Facts 2019: An analysis of European plastics production, demand and waste data. PlasticsEurope: Association of Plastics Manufacturers, Brussels.

Primpke, S., Christiansen, S.H., Cowger, W., De Frond, H., Deshpande, A., Fischer, M., Holland, E.B., Meyns, M., O'Donnell, B.A., Ossmann, B.E., 2020. Critical assessment of analytical methods for the harmonized and cost-efficient analysis of microplastics. Appl. Spectrosc. 74, 1012-1047.

Renner, K.O., Foster, H.A., Routledge, E.J., Scrimshaw, M.D., 2021. A comparison of different approaches for characterizing microplastics in selected personal care products. Environ. Toxicol. Chem. n/a. https://doi.org/https://doi.org/10.1002/etc.5057.

Rios Mendoza, L.M., Karapanagioti, H., Álvarez, N.R., 2018. Micro(nanoplastics) in the marine environment: Current knowledge and gaps. Curr. Opin. Environ. Sci. Health 1, 47-51. https://doi.org/https://doi.org/10.1016/j.coesh.2017.11.004.

Ru, J., Huo, Y., Yang, Y., 2020. Microbial degradation and valorization of plastic wastes. Front. Microbiol. 11. https://doi.org/10.3389/fmicb.2020.00442.

Simon, M., van Alst, N., Vollertsen, J., 2018. Quantification of microplastic mass and removal rates at wastewater treatment plants applying Focal Plane Array (FPA)-based Fourier Transform Infrared (FT-IR) imaging. Water Res. 142, 1-9. https://doi.org/10.1016/j.watres.2018.05.019.

Smith, L.M., Aitken, H.M., Coote, M.L., 2018. The fate of the peroxyl radical in autoxidation: how does polymer degradation really occur? Acc. Chem. Res. 51, 2006-2013. https://doi.org/10.1021/acs.accounts.8b00250.

Song, Y.K., Hong, S.H., Eo, S., Han, G.M., Shim, W.J., 2020. Rapid production of micro- and nanoplastics by fragmentation of expanded polystyrene exposed to sunlight. Environ. Sci. Technol. 54, 11191-11200. https://doi.org/10.1021/acs.est.0c02288.

Song, Y.K., Hong, S.H., Jang, M., Han, G.M., Jung, S.W., Shim, W.J., 2017. Combined effects of UV exposure duration and mechanical abrasion on

microplastic fragmentation by polymer type. Environ. Sci. Technol. 51, 4368-4376. https://doi.org/10.1021/acs.est.6b06155.

Sørensen, L., Groven, A.S., Hovsbakken, I.A., Del Puerto, O., Krause, D.F., Sarno, A., Booth, A.M., 2021. UV degradation of natural and synthetic microfibers causes fragmentation and release of polymer degradation products and chemical additives. Sci. Total Environ. 755, 143170. https://doi.org/https://doi.org/10.1016/j.scitotenv.2020.143170.

Stark, N.M., Matuana, L.M., 2004. Surface chemistry changes of weathered HDPE/wood-flour composites studied by XPS and FTIR spectroscopy. Polym. Degrad. Stab. 86, 1-9. https://doi.org/https://doi.org/10.1016/j.polymdegradstab.2003.11.002.

ter Halle, A., Ladirat, L., Gendre, X., Goudouneche, D., Pusineri, C., Routaboul, C., Tenailleau, C., Duployer, B., Perez, E., 2016. Understanding the fragmentation pattern of marine plastic debris. Environ. Sci. Technol. 50, 5668-5675. https://doi.org/10.1021/acs.est.6b00594.

Thompson, R.C., Moore, C.J., vom Saal, F.S., Swan, S.H., 2009. Plastics, the environment and human health: current consensus and future trends. Philos. Trans. R. Soc. London, Ser. B 364, 2153-2166. https://doi.org/10.1098/rstb.2009.0053.

Wahl, A., Le Juge, C., Davranche, M., El Hadri, H., Grassl, B., Reynaud, S., Gigault, J., 2021. Nanoplastic occurrence in a soil amended with plastic debris. Chemosphere 262, 127784. https://doi.org/https://doi.org/10.1016/j.chemosphere.2020.127784.

WEF, 2016. The new plastics economy: Rethinking the future of plastics, in: Neufeld, L., Stassen, F., Sheppard, R., Gilman, T. (Eds.), World Economic Forum. World Economic Forum, Geneve, Switzerland.

Welsh, J.A., Horak, P., Wilkinson, J.S., Ford, V.J., Jones, J.C., Smith, D., Holloway, J.A., Englyst, N.A., 2020. FCMPASS Software Aids Extracellular Vesicle Light Scatter Standardization. Cytometry Part A 97, 569-581. https://doi.org/https://doi.org/10.1002/cyto.a.23782.

Yang, L., Zhang, Y., Kang, S., Wang, Z., Wu, C., 2021. Microplastics in freshwater sediment: A review on methods, occurrence, and sources. Sci. Total Environ. 754, 141948. https://doi.org/https://doi.org/10.1016/j.scitotenv.2020.141948.

Zhang, K., Hamidian, A.H., Tubić, A., Zhang, Y., Fang, J.K.H., Wu, C., Lam, P.K.S., 2021. Understanding plastic degradation and microplastic formation in the environment: A review. Environ. Pollut. 274, 116554. https://doi.org/https://doi.org/10.1016/j.envpol.2021.116554.

Zhu, W., Zhang, G., Liu, B., Chung, T.C.M., 2018. Polyethylene containing antioxidant moieties exhibiting high thermal-oxidative stability for high temperature applications. Polymer 146, 101-108. https://doi.org/https://doi.org/10.1016/j.polymer.2018.05.019.

2 Ageing and fragmentation of marine microplastics

Abstract

The generation of small fragments from the environmental ageing of microplastics (MPs) is still a poorly known process. This work addresses the fragmentation of MPs obtained from marine debris consisting of polyethylene and polypropylene (PE and PP in environmental mixture) and polystyrene (PS) after exposure to accelerated ageing by irradiation and mechanical stirring. Number particle size distribution in the 1-100 μm range was assessed by combining laser diffractometry with particle counts from flow cytometry. The results showed the generation of a high number of small MP particles, which reached 10^5-10^6 items/mg of plastic with most fragments < 2 μm. The results showed that environmentally aged MPs give rise to a larger number of small MPs in a pattern consistent with progressive fragmentation in the three spatial dimensions. The proportion of small MPs was much higher than that found in current sampling campaigns, suggesting a severe underestimation of the environmental presence of small MPs. We also demonstrated the generation of nanoplastics (NPs) in the fraction < 1 μm from irradiated runs. The results showed that the mechanism that produced nanoplastics (NPs) from MPs was irradiation, which yielded up to 10^{11}-10^{13} NPs/g with particle size in the few hundreds of nm range. Our results are relevant for the assessment of fate and risk of plastic debris in the environment showing that the number of small plastic fragments produced during the ageing of MPs are much larger than expect from the extrapolation of larger size populations.

2.1 Introduction

The use of plastic has transformed our society. Plastics are cheap and lightweight materials suitable to produce a large variety of goods that consume much less energy than alternatives like glass, metals, or paper. So, the use of plastics increased rapidly since the onset of their industrial production in the 1950s. According to Plastics Europe, the global production of plastic raw materials reached 367 million tonnes in 2020. However, the growing use of plastic has been accompanied by a parallel increase of plastic litter. Concerning domestic wastes, plastic ranks third, only after organic waste, paper, and cardboard. The available data show that 29.5 million tonnes of post-consumer plastic wastes were recovered in 2020 (EU27+3), from which 12.4 were incinerated, 10.2 recycled and 6.9 million tonnes were landfilled. Although landfilling is rapidly decreasing (-46.5 % in the 2006-2020 period), large amount of plastic still becomes disseminated in the environment mainly as a consequence of the abuse of non-durable goods and improper waste management practices, but also because of the wearing of plastic items during use and the presence of intentionally added microplastics in some products (Napper and Thompson, 2016).

Plastic particles are defined by their size, which is the main factor that figures out their environmental fate. Conventionally, plastic debris fragments are defined as microplastics (MPs) if their largest dimension is < 5 mm (GESAMP, 2019). The lower boundary of MPs is generally taken as 1 µm below which, the particles are considered nanoplastics (NPs) provided they are produced from the degradation of larger particles and display a colloidal behaviour (Gigault et al., 2018). The 5 mm cut-off is arbitrary and accepted to preserve the information from marine sampling campaigns using plankton nets, but the 1 µm one has physical background as it is the size below which particles tend to exhibit a colloidal behaviour or, if dispersed in air, are subject to Brownian motion rather than gravity sedimentation. However, size definitions are controversial, and some researchers find more natural the < 100 nm boundary in line

with the usual practice for manufactured nanoparticles and the size below particles generally display properties different from bulk samples of the same material (Auffan et al., 2009; Hartmann et al., 2019). Besides, a recent ECHA's proposal to complete a REACH Annex XV restrictions proposal for intentionally added MPs considers as such solid polymers with dimensions in the 0.1-5000 μm range. In this manuscript we will consider NPs secondary fragments with size < 1 μm based on their colloidal behaviour (Jakubowicz et al., 2021; Reynaud et al., 2022).

When exposed to environmental stressors, plastics undergo chemical transformations that lead to the breaking of polymer backbone and the generation of smaller and smaller fragments. The most accepted paradigm is that the degradation process is initiated by photo-oxidation and hydrolysis due to the exposure to sunlight, air, and water (Gerritse et al., 2020). The leaching of stabilisers and the accumulation of polymer chain scissions promote surface cracks and make plastic brittle (Andrady, 2011; Chamas et al., 2020). The physical fragmentation of plastic particles with the generation of MPs is also enhanced by mechanical stress due to waves, friction with sand, and even with the intervention of the biota (Mateos-Cárdenas et al., 2020). However, the degradation of plastics is a complex process, and the exact role of the several factors is controversial. What is clear is that the generation of plastic fragments may give rise to high amount of small plastic particles. It has been shown that the mechanical and photochemical fragmentation of low density polyethylene (LDPE) under UV irradiation simulating one year of solar exposure gives rise to 10^4-10^5 MPs/g and up to 10^{10} NPs/g LDPE (Sorasan et al., 2021).

The environmental alteration of plastics is usually followed by spectroscopic techniques that identify the functional groups arising from the oxidation and hydrolytic reactions of synthetic polymers. The photodegradation of polyolefins is usually assessed by the bands of hydroxyl and carbonyl/carboxyl moieties from their mid-infrared spectra (Gulmine et al., 2003). The photo-oxidation of polyesters has been shown to proceed

by oxidation of the methylene groups adjacent to ester linkages (Fotopoulou and Karapanagioti, 2019). In some cases, the formation of hydrolysis and photooxidation moieties has been found to correlate with the time the plastics were exposed to environmental degradation, but the trend is not generally consistent for different fragments (Brandon et al., 2016; Sorasan et al., 2022). It must be considered that the degradation of plastics is very sensitive to the conditions of their local environmental that may change along the lifecycle of plastic debris (Ioakeimidis et al., 2016). Hiejima et al. showed that the degradation of polyethylene was accompanied by a crystallinity increase as a consequence of the higher reactivity of the amorphous phase (Hiejima et al., 2018). The chemical characteristics of the smaller fragments are different from their larger counterparts because the degradation process makes them more polar and mobile, and, therefore, more prone to interact with the biota (González-Pleiter et al., 2019). Besides, small plastic fragments interact more easily with other pollutants due to their higher specific surface thereby originating a carrier effect for potentially toxic substances (Anastopoulos et al., 2021; Godoy et al., 2019).

This work addresses the fragmentation and degradation of plastic fragments from real marine debris consisting of polyethylene (PE), polypropylene (PP) and polystyrene (PS), when exposed to mechanical agitation and accelerated ageing by means of UV irradiation and mechanical stirring. The irradiation used a medium-pressure mercury lamp delivering the equivalent of up to five years of solar UVA+UVB exposure (280-400 nm). We measured the particle size distribution of the fragments produced during the degradation of MPs down to 1 μm. Our work showed how environmentally aged MPs may produce MPs in the few microns range or below, which is relevant because such small sizes are outside current sampling campaigns. We also focused on NPs and studied the role of irradiation in the mechanism leading to their generation.

2.2 Experimental section

2.2.1 Materials

PE and PP fragments were recovered from the sandy beach Ámbar located in the North coast of La Graciosa Island, Canary Islands (Spain, 29°16′46″ N 13°29′45″ W). La Graciosa Island is part of the Chinijo Archipelago, a highly protected area, declared Biosphere Reserve by UNESCO in 1993. Ámbar is an isolated sandy beach with limited human pressure. However, it receives the wind-driven Canary Current, part of the North Atlantic Gyre, which is responsible for a high level of plastic pollution (Villanova-Solano et al., 2022). The MPs recovered from Ámbar beach were predominantly PE and PP (95 % altogether) as explained elsewhere (Edo et al., 2019). The particles selected for this study were PE and PP mixed in 88:12 ratios in weight, the same proportion found in the environmental samples.

PS foam fragments were recovered from Ilha Desserta (Faro, Portugal, 36°58'06" N 7°52'25" W). The location is close to Cape Saint Mary, the southernmost point of Portugal mainland. In that area, waters from Ria Formosa Natural Park, a protected area of marshes, and sea water from Atlantic Ocean get mixed. The area is generally clean, unpopulated, and preserved from the main currents, only holding touristic activities in summer. The collected materials are expected to have origin in fishing and commercial activities in nearby areas. Once on the island, the materials remain in place, suffering climatic ageing only stopped by cleaning campaigns.

All particles were sieved to select specimens in the 1-5 mm range and were washed carefully with HPLC grade methanol (CAS 67-56-1), and ultrapure water (Milli-Q Q-POD® Ultrapure Water System, resistivity > 18 MΩ cm) before running the

experiments. The washed fragments were dried, weighed, and stored in closed containers until runs and analyses. Fig. S2.1 (Supplementary Material, SM) shows images of the PE-PP and PS fragments used in this work.

2.2.2 Experimental procedure

The degradation runs were performed in a 1 L photochemical reactor thermostated at 24 °C, magnetically stirred (700 min^{-1} equivalent to 26 kJ/day of estimated dissipation power) and equipped with a Novalight TQ150 medium-pressure mercury lamp (Peschl Ultraviolet, 150 W) emitting in the 297-579 nm range. The irradiation experiments were performed using an equivalence with solar radiation calculated as follows. The NASA Surface meteorology and Solar Energy database was used to obtain the monthly averaged insolation for the latitude of Madrid, namely 183 W m^{-2} or 4.4 kWh m^{-2} day^{-1}, 5 % of which corresponds to UVA + UVB (or 280-400 nm). The average irradiance in the photoreactor was 1060 W m^{-2} (UVA + UVB) measured by means of a StellarNet Modular Spectrometer. Accordingly, 1 year of solar UVA+UVB corresponded to approximately 72 h or three days of continuous irradiation. Irradiation runs were conducted for 360 h of continuous irradiation, equivalent to five years of solar UVA+UVB exposure.

All experiments were conducted in simulated seawater prepared according to ASTM D1141-98 (ASTM, 2021). Simulated seawater was filtered with 0.45 μm PTFE Millipore syringe filters. The runs for PE-PP were loaded with a concentration of 40 g/L, while those for PS used 4 g/L (because of the lower density of expanded polystyrene). Two types of runs were performed, irradiated and non-irradiated. Non-irradiated runs provided information on the fragmentation due to mechanical degradation and hydrolysis, while irradiation included photooxidative degradation. All runs were performed twice, and all analyses were replicated. All runs started with 72 h of stirring

without irradiation. Then, irradiated runs proceeded for 360 h more with samples taken for analyses every 72-h equivalent to five and one year of solar exposure respectively. Non-irradiated runs proceeded for 720 h more (720 + 72 h) with an intermediate sample taken at 360 (+72) h. In what follows the samples are identified as PE-PP or PS followed by NI (non-irradiated) or I (irradiated) and a number meaning the hours on stream after the initial 72 h non-irradiated period, for which the corresponding sample is denoted as "0". The liquid was sampled from the central part of the reactor without stopping the stirrer. The samples for the different measurements were filtered through 1 μm PTFE and 100 μm stainless steel filters as indicated below.

2.2.3 Analytical methods

Infrared analyses were performed using Attenuated Total Reflectance Fourier Transform Infrared (ATR-FTIR) spectroscopy in a ThermoScientific Nicolet iS10 equipment with a Smart iTR-Diamond module and OMNIC software in the 650-4000 cm^{-1}. Micro-Fourier Transform Infrared Spectroscopy (micro-FTIR) was performed in a Perkin-Elmer Spotlight 200 Spectrum Two apparatus with MCT detector in transmission mode with spectral range 550-4000 cm^{-1}.

Particle size distribution was measured using a Malvern Mastersizer 2000 laser diffractometer equipped with Hydro 2000MU dispersion unit. The equipment provides particle size distribution in the 0.020-2000 μm according to ISO 13320:2020. The samples for flow cytometry measurements were filtered through 100 μm stainless steel filters to avoid clogs in the fluidic path. Flow cytometry was used to quantify the particles produced in the 1-100 μm range. The calculation was based on relating scattered intensities to the scattering cross-section of the particle derived from particle size using Mie's theory. In this work, we used the intensity of forward-scattered light (FSC) as obtained from the flow cytometer converted into particle size by means of

their refractive index (n = 1.611 for PS and n = 1.505 for PE-PP at 488 nm) using a calibration with latex beads of 1, 3, 4, 6, 10, 15 and 25 μm as explained elsewhere (de Rond et al., 2018; Sorasan et al., 2021). The assumptions underlying the use of flow cytometry calculation for particle size are that particles are homogeneous with known refractive index. As for other characterization techniques, the obtained diameter was that of sphere with the same scattering behaviour and refractive index. The water used for suspending MPs was also analysed to subtract its background signal. Additional details can be found elsewhere (Sorasan et al., 2021).

Total Organic Carbon (TOC) was determined as Non Purgeable Organic Carbon (NPOC) by means of a Shimadzu TOC-VCSH apparatus with ASI-V autosampler. The samples for TOC were filtered using 1 μm pore size Puradisc 25 TF filters. Differential Scanning Calorimetry (DSC) and Thermogravimetric analyses (TGA) were performed in a DSC/DTA/TGA Q600 apparatus from TA Instruments with heating rate 10 °C/min. DLS measurements were performed using a Malvern Zetasizer Nano ZS instrument to assess the size of submicron particles in samples obtained after filtering reactor aliquots through 1 μm Puradisc 25 TF filters. The liquid fraction < 1 μm obtained at the end of the runs was concentrated using a rotary evaporator at 60 °C, then subject to liquid-liquid extraction using xylene (CAS 1330-20-7, Merck) in the case of the experiments with PE-PP, and trichloromethane (CAS 67-66-3, Merck) in the case of PS. A reprecipitation in vacuum oven at 50 °C for 24 h allowed obtaining a precipitate suitable for micro-FTIR analyses, thereby providing spectroscopic identification of the particles in the nanoplastic size range (< 1 μm).

2.3 Results and discussion

2.3.1 Characterization of MPs

Fig. 2.1. shows the ATR-FTIR spectra of the fragments used in degradation runs. They correspond to PE, PP and PS sampled in beaches from Spain and Portugal as indicated before. The spectra present the typical features of the indicated polymers. Fig. 2.1A displays the typical peaks of PE, namely the stretching vibrations of -CH_2 at 2915 cm^{-1} and 2846 cm^{-1}, the scissoring mode of the -CH_2 at 1465 cm^{-1} and the -CH_2 rocking vibration at 719 cm^{-1}. The stretching vibrations of -CH_2 and -CH_3 are clearly visible from PP specimens at 2850, 2920, and 2950 cm^{-1}, together with the symmetrical and asymmetrical bending of -CH_3 bonds at 1376 and 1460 cm^{-1} (Fig.2.1B). The spectra of PS MPs (Fig. 2.1C) show the aromatic and aliphatic stretching vibrations of C-H bonds. The peak at 3025 cm^{-1} (and other smaller peaks at higher wavenumber) corresponded to aromatic C-H vibration. The bands at 2850 and 2918 cm^{-1} are due to symmetric and asymmetric stretching vibration of the methylene groups. The carbon-carbon stretching vibrations of the aromatic ring appear at 1600, 1492, and 1452 cm^{1}. The in-plane C-H bending in the aromatic ring is visible at 1022 cm^{-1}. The out-of-plane bending bands of C-H bonds appear at 756, and 700 cm^{-1} (Olmos et al., 2014). In all cases, peaks corresponding to the moieties associated with environmental degradation were apparent. When exposed to UV-radiation and oxygen, polyolefins undergo photooxidation reactions that start with the formation of O_2-polymer charge transfer complexes. The degradation process leads to the formation of a variety of oxygenated compounds including carboxylic acids, esters, lactones, alcohols and many more (Grause et al., 2020). The photochemical oxidation of PS proceeds in a similar way with the reaction of a photoproduced polystyryl radical with oxygen to produce peroxy radical (Torikai et al., 1986). The bands from oxygenated moieties are clear in PE, PP and PS specimens, especially the broad O-H stretching band in the 3200-3500 cm^{-1}

region and, to a lesser extent, the absorption in the 1760-1660 cm^{-1} range attributed to the stretching vibration of C=O bonds.

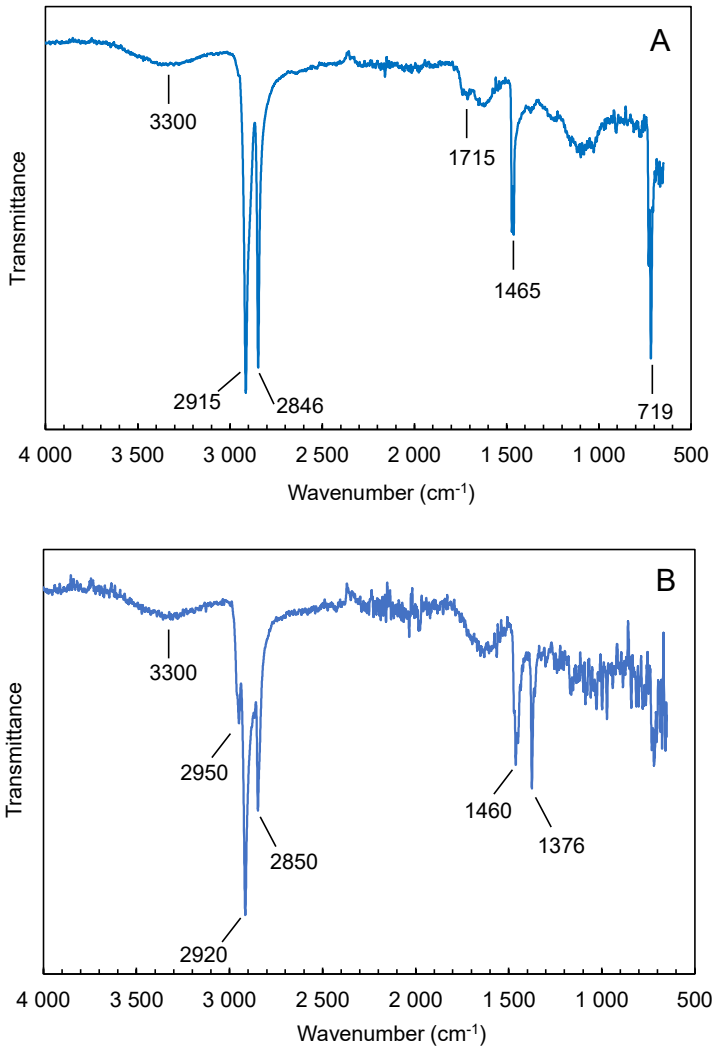

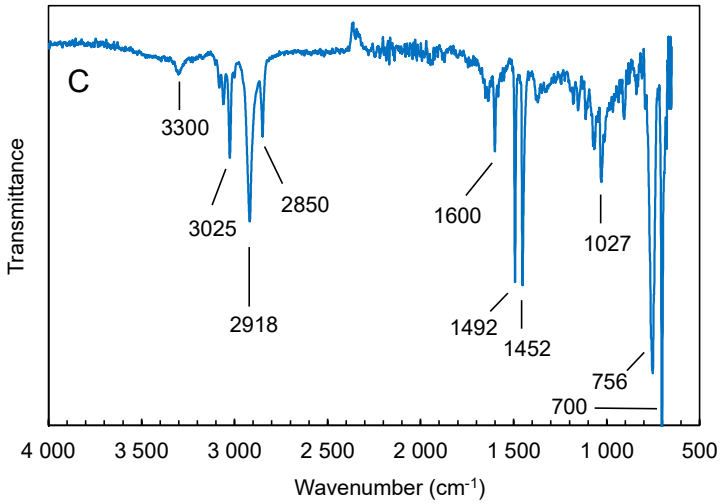

Figure 2.1. *FTIR spectra of fragments as recovered from environmental samples of PE (A), PP (B) and PS (C). (Marked peaks are explained in the text.)*

2.3.2 Fragmentation into small **microplastics (1-100 μm)**

Table 2.1 shows the number of particles in the 1-100 μm range measured by flow cytometry and expressed per unit mass of PE-PP or PS MPs. Particle counts were obtained after subtracting blanks, which provided an estimation of possible particle contamination from laboratory sources. Particle counts in the 1-100 μm for blank runs, however, were always negligible compared to the values obtained from experiments. Simulated seawater was previously filtered through 0.45 μm PTFE filters and, accordingly, the size of the particles entrained with it was below the 1-100 μm range. The results showed particle counts in the 10^5-10^6 particles/mg range for both plastics. After the initial period of 72 h without irradiation, the number of particles detached from PE-PP and PS MPs was already high (1.2-1.8 x 10^5 particles/mg) indicating that the role played by mechanical stress in the fragmentation of MPs was important and that environmentally samples MPs were already prone to detach small MP fragments even if carefully washed before starting the runs.

Plastics in the environment undergo a combination of photochemical and mechanical stresses that lead to their fragmentation in smaller particles. The process is still not completely clarified, although it is generally accepted that shear or tensile stresses combined with a loss of mechanical properties due to photodegradation favour fragmentation (ter Halle et al., 2016). The fragmentation of plastics in the marine environment was also studied for expanded polystyrene (EPS) under oxidative degradation and hydrodynamic mechanical stress. It was found that the fragmentation of mesoplastic fragments into small MPs and NPs occurred at an early stage and was evident only after a few days of ageing (Mattsson et al., 2021). Song et al. performed combined treatments of UV irradiation and mechanical abrasion with LDPE, PP, and EPS, and showed that polyolefins were not substantially fragmented in the absence of irradiation, but UV exposure followed by mechanical abrasion resulted in several thousands of MPs/pellets. On the contrary, EPS underwent fragmentation by mechanical stress alone, although the combined treatment resulted in a higher number of secondary particles including NPs (Song et al., 2017). Rizzo et al. performed *in situ* experiments with high density polyethylene (HDPE) and PS in coastal areas exposed to different hydrodynamic conditions and obtained faster degradation for PS attributed to higher susceptibility to UV-induced photo-oxidation and hydrodynamic activity. Besides, the creation of biofilms under subtidal conditions slowed down degradation probably due to the polymer photo-protection (Rizzo et al., 2021).

Our results showed that the formation of small MPs, takes place very quickly (72 h in darkness) with specimens previously aged under environmental conditions. After the onset of irradiation, the number of MPs produced increased both in the case of PE-PP and PS to decline thereafter, which could be attributed to their conversion into NPs (< 1 μm). Experiments performed in darkness for 720 h showed a slight decrease in the number of fragments form PE-PP and an increase in the case of PS, probably due to the higher resistance of PE-PP pellets to the detachment of small MPs and, probably, to its higher tendency to produce NPs. In a previous work with LDPE we found evidence that the mechanical degradation led to a rapid production of secondary MPs

irrespective of the use of new, used and recycled LDPE MP pellets (Sorasan et al., 2021). In the case of new pellets, however, the number of small MPs produced was three orders of magnitude lower than those found in this work using environmentally aged MPs. The difference was clearly due to the history of environmental ageing suffered from the tested specimens. Fig. S2.2 (SM) shows micrographs of some pellets of PE, PP and PS before irradiation, which evidenced the presence of cracking lines and irregularities suggesting a fragmentation pattern.

Table 2.1. *Particles counts for fragments detached from PE-PP and PS MPs per unit mass of plastic in the 1-100 μm range measured by flow cytometry.*

Particles/mg PE-PP or PS				
	PE-PP (NI)-0[a]	$1.71 \times 10^5 \pm 3.0 \times 10^4$	PS (NI)-0[a]	$1.21 \times 10^5 \pm 2.8 \times 10^4$
Irradiated	PE-PP (I)-72	$2.64 \times 10^5 \pm 2.7 \times 10^4$	PS (I)-72	2.38 x 105 ± 3.7 x 104
	PE-PP (I)-144	$2.75 \times 10^5 \pm 2.0 \times 10^4$	PS (I)-144	4.43 x 105 ± 5.0 x 104
	PE-PP (I)-216	$2.26 \times 10^5 \pm 2.2 \times 10^4$	PS (I)-216	6.84 x 105 ± 4.9 x 104
	PE-PP (I)-288	$1.50 \times 10^5 \pm 2.5 \times 10^4$	PS (I)-288	7.30 x 105 ± 8.3 x 104
	PE-PP (I)-360	$1.07 \times 10^5 \pm 1.2 \times 10^4$	PS (I)-360	5.93 x 105 ± 5.5 x 104
Non-irradiated	PE-PP (NI)-0[a]	$1.77 \times 10^5 \pm 2.4 \times 10^4$	PS (NI)-0a	1.42 x 105 ± 1.2 x 104
	PE-PP (NI)-360	$1.89 \times 10^5 \pm 2.6 \times 10^4$	PS (NI)-360	8.75 x 105 ± 4.8 x 104
	PE-PP (NI)-720	$1.33 \times 10^5 \pm 1.7 \times 10^4$	PS (NI)-720	1.07 x 106 ± 5.9 x 104

[a] (NI)-0 samples taken after stirring in the absence of irradiation for 72 h

The size distribution of plastic fragments is shown in Figs. 2.2A and 2.2B for irradiated runs and Fig. S2.3 for non-irradiated experiments. The figures were built using volumetric particle size distributions from laser diffractometry combined with the particle counts in the 1-100 μm range obtained from flow cytometry. The results showed a high number of particles in the lower size range, with values in the tens of thousands of secondary MPs per mg of PE-PP/PS, 98% of them < 10 μm in all cases. Both for PE-PP and PS, the most abundant secondary MP particles were in the few microns range.

Fig. S2.4 (SM) shows flow cytometry histograms for the runs PE-PE (I)-72/360 and PS (I)-72/360, revealing a common observation in all runs, namely a non-negligible population of particles < 1 μm, which did not appear in laser diffractometry size distribution. This fact can be attributed to the low volume represented by such small fraction compared with larger particles. The integration yielding the number of plastic particles per unit volume was converted into MPs/g of PE-PP and PS with the initial concentration for both types of particles (40 and 4 g/L, respectively).

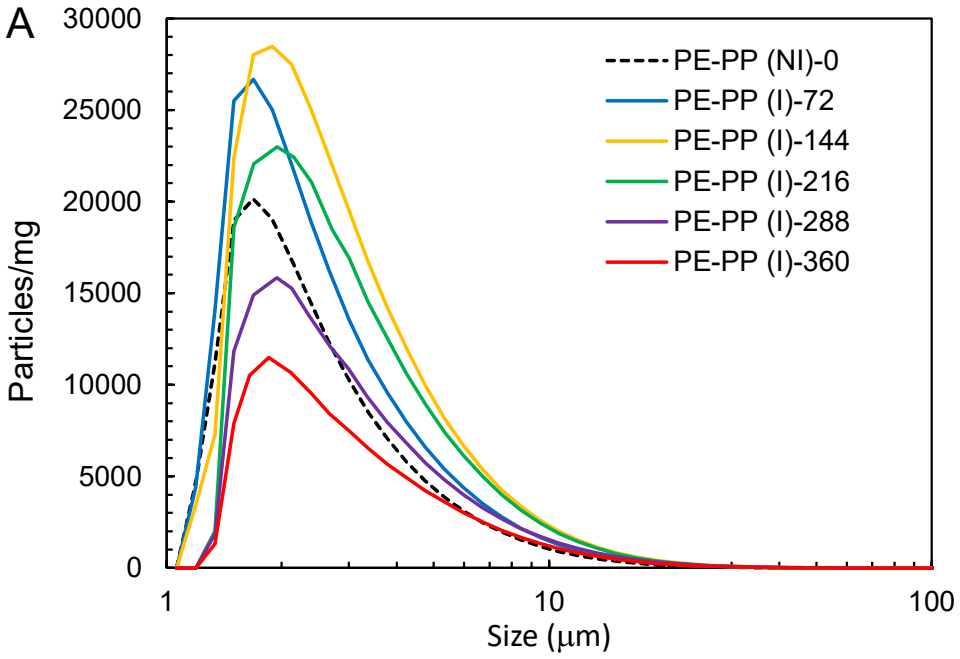

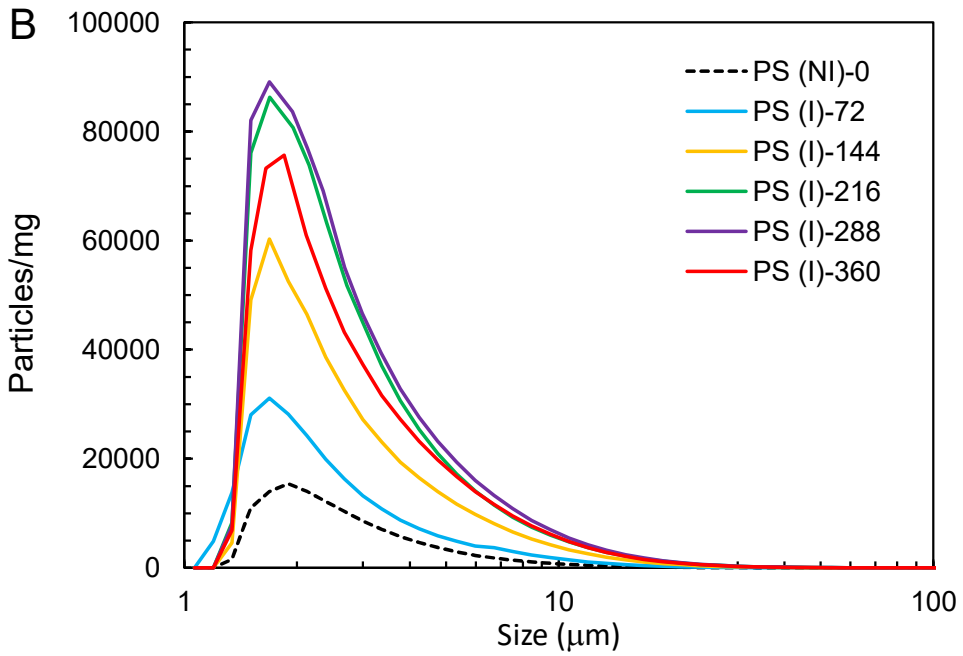

Figure 2.2. *Size distribution for particles produced during the irradiation of PE-PP MPs (A) and PS MPs (B). The lines marked as PE-PP/PS (NI)-0 correspond to samples taken after 72 h under agitation in darkness.*

The particulate material obtained at the end of the runs was separated from pellets, filtered, and analysed using ATR-FTIR. The spectra recorded for PE-PP (I)-360 and PS (I)-360 runs are shown in Fig. 3 while spectra for PE-PP (NI)-720 and PS (NI)-720 are included as SM Fig. S2.5. The spectroscopic information for that particulate material recovered at the end of the reactions displayed the features of PE-PP and PS with clear evidence of photooxidative degradation as shown by the presence of C=O stretching bands at 1740 cm^{-1} and C-O stretching absorptions in the 1050-1310 cm^{-1} range.

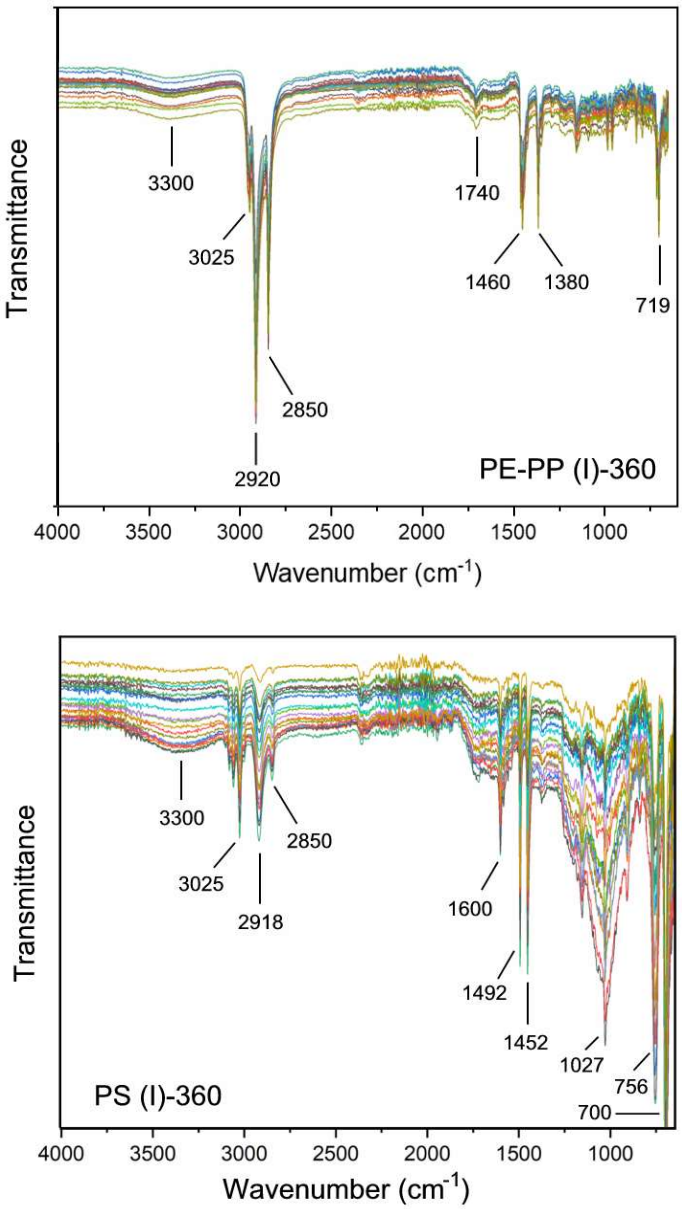

Figure 2.3. ATR-FTIR spectra of the particulate material recovered after PE-PP (I)-360, and PS (I)-360 runs.

Our data showed that most micron-size range particles detached from PE-PP and PS MPs have a rather narrow distribution and that the fragmentation process takes place quickly even without irradiation. As shown in Table 2.1, 72 h of agitation in darkness, corresponding to experiments labelled PE-PP/PS (NI)-0, was enough to produce small MPs in the 10^5 items/mg range both for PE-PP and PS. Our data are consistent with a fragmentation mechanism based on surface detachment of small MPs. Cracks, grooves,

and other irregularities developed on the surface of the plastic particles during degradation, would serve as detaching points upon the action of mechanical forces (Zhang et al., 2021). In a previous work, we studied the generation of small fragments from pre-production pellets of LDPE. The results also showed abundance of secondary MPs in the few microns range, although in much lower concentration. It is reasonable to assume that plastic fragments recovered from marine debris, which have been subject to environmental ageing were much more prone to produce small MPs particles under mechanical stress. On the contrary, the exposure to UV light reduced the number of MP particles in the 1-100 μm range suggesting that smaller particles (NPs, < 1 μm) are being produced from micron-sized MPs upon irradiation. The mass of MPs produced from the pellets may be estimated using the particle size distribution and the total number of particles as determined using flow cytometry. A calculation for each size using an average density of PE-PP and PS gives a mass of PE-PP particles in the 1-100 μm range of up to 2.5 % of the initial load of fragments for PE-PP and about 0.2 % for PS.

Kooi and Koelmans studied the size distribution of 19 sets of data from 11 studies that reported particle sizes in the hundreds or thousands of microns range (Kooi and Koelmans, 2019). The authors found a decrease in particle concentration with increasing size generally following a power law, which can be expressed in logarithmic form as: $\log(\text{abundance}) = c - \alpha \log(\text{size})$, with exponent $\alpha = 1.6$. When applied to our data, the same power law shows good fitting but with higher exponent (Fig. 2.4). We obtained good fitting to power law size distribution with $\alpha = 3.0 \pm 0.3$ with little difference between PE-PP (3.1 ± 0.2) and PS (2.9 ± 0.3). The slope of the power law, in steady state fragmentation equals the spatial dimension of the objects broken down (Cózar et al., 2014). Therefore, our results suggested that the progressive fragmentation of MPs into smaller fragments proceeded in the three spatial dimensions of the objects (Yakimets et al., 2004). Accordingly, the abundance expected for smaller sizes should be much higher in environmental samples (with smaller scaling exponent). The apparent deviation of the power law for the dots in the upper left side of the plots

representing NPs is probably related to the particle size of the background colloid of simulated seawater as explained below.

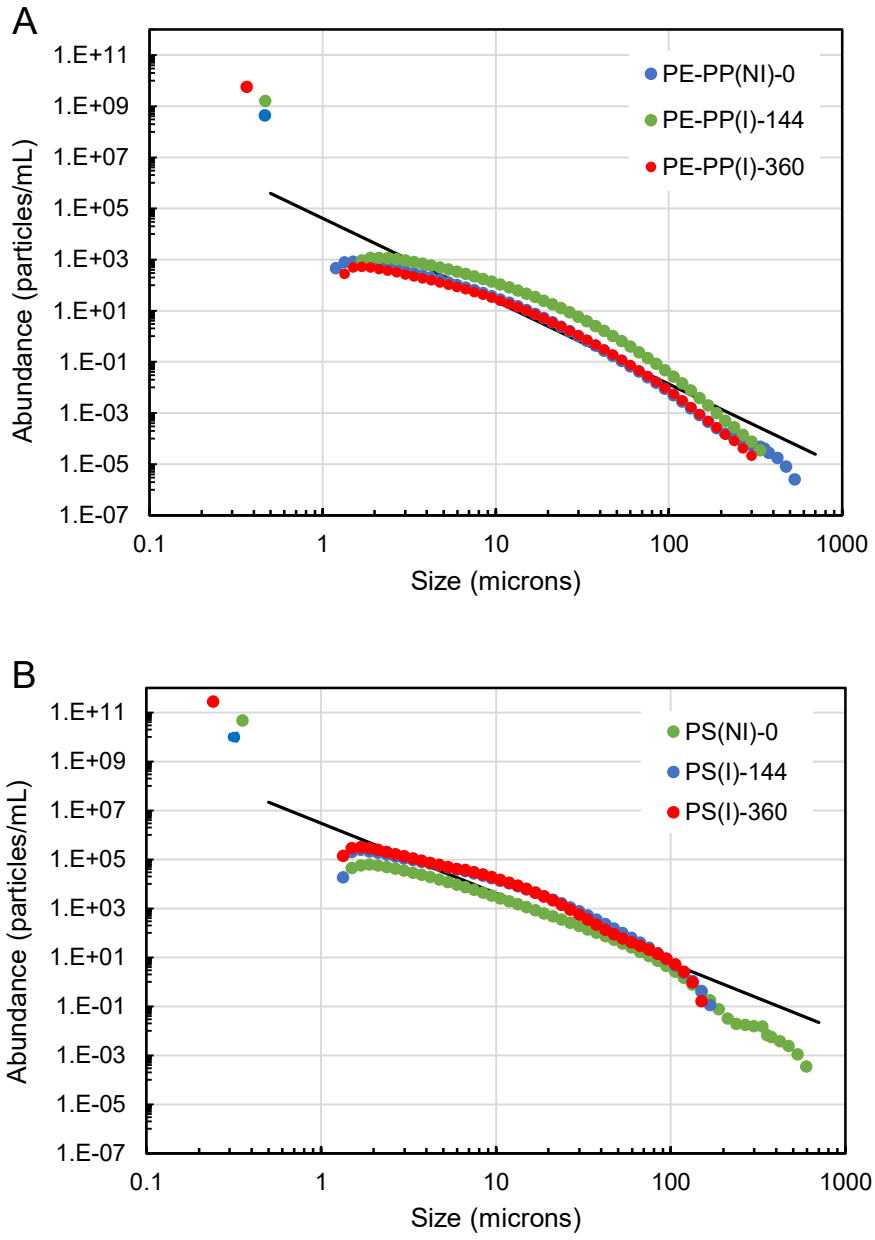

Figure 2.4. *Relative microplastic abundance for different particle sizes in non-irradiated, PE-PP/PS(NI)-0, and irradiated, PE-PP/PS(I)-144 and 360, samples, and average fitting to the power law exponent: 3.1 for PE-PP (A) and 2.9 for PS (B). (The dots in the upper left side of the plots correspond to NPs with abundance calculated from TOC and size from DLS.)*

The degree of alteration of small MPs was assessed using DSC/TGA from the particulate material at the end of the runs once removing the remains of the initial plastic fragments. The results are shown in Fig. S2.6 (SM). The peaks at 124.5 °C corresponded to PE and was accompanied by a small and broader peak at 140.9-142.9 °C compatible with the presence of photodegraded PP in the PE-PP mixture. It has been described that the photodegradation of PP induces a shift in the melting point from about 160 °C to lower temperatures due to the reorganization of macromolecular chains upon chain scission processes (Uheida et al., 2021). The higher resistance to photodegradation of PE compared with PP is well known (Ojeda et al., 2011). The decrease in glass transition temperature of PS from ~100 °C to 50-60 °C can be attributed to the lower molecular weight of the fragments resulting from the photodegradation of the polymeric chains. Finally, TGA data showed that samples were completely organic without residue after heating at 900 °C

2.3.3 Generation of nanoplastics (< 1 μm)

It is a well-known fact that the ageing of plastics in the environment produces particles below the micron size, which are very difficult to identify because they fall beyond most analytical methods. NPs are very challenging because of their size and chemical composition, which is not much different from that of the organic matter. Consequently, the available data on the occurrence of NPs in the environment is very limited. The techniques under study include, among others, pyrolysis gas chromatography/mass spectrometry, centrifugation, and different surface-interaction-based separations (Nguyen et al., 2019; Zhou et al., 2021). In essence, the possibilities are limited to vibrational spectroscopy, and mass spectrometry with results that depend on adequate pre-concentration. In this work, the presence of submicron plastic particles was clear from the TOC results of samples filtered through 1 μm filters shown in Fig. 2.5.

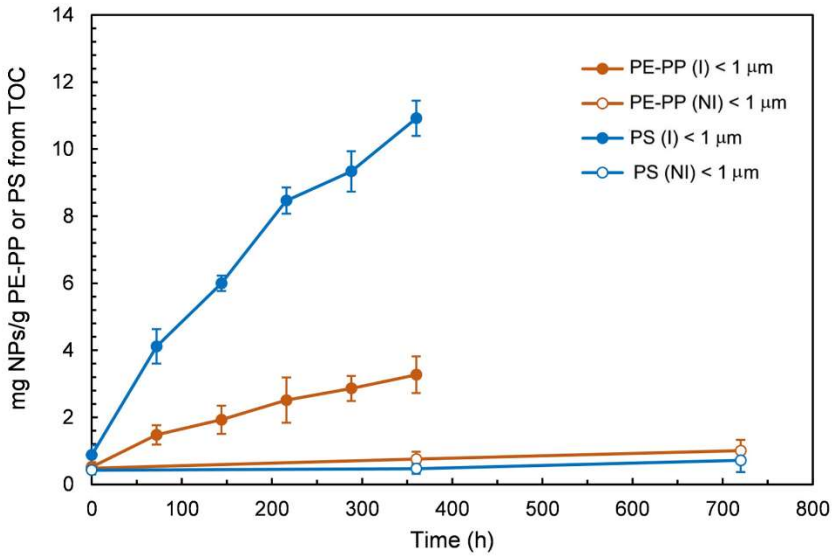

Figure 2.5. *Generation of NPs expressed as mg PE-PP/PS per g of plastic as determined from the TOC of samples filtered through 1 µm pore size filters.*

The organic carbon content, due to PE-PP or PS, was much higher in irradiated samples and increased with time consistent with a role of UV irradiation in the photodegradation and fragmentation of polymers. The NPs mass reached > 10 mg NPs/g of PE-PP and 2.8 mg NPs/g of PS. The results for non-irradiated runs showed a much lower number of NPs. In a laboratory work using a photoreactor emitting UVA+UVB irradiance similar to that used in this work, Gigault et al. showed the generation of NPs upon exposure of marine microplastics (Gigault et al., 2016). The fragmentation of EPS into NPs was also assessed for two year outdoor weathering, which resulted in > 10^8 NPs/cm^2 in the 138–189 nm range (Song et al., 2020). Besides, it has been shown that UV-irradiation not only produces NPs, but can also lead to their mineralization (Tian et al., 2019). In our work, DLS particle size measurements for different irradiation times showed the production of colloidal submicron particles with sizes in the few hundreds of nm range (Table 2.2). The fact that simulated seawater had particles with DLS size of 228 ± 20 nm probably meant that the background colloid tended to grow with the aggregation of polymeric nanoparticles and is the probable

reason for the limited differences observed among samples and for the deviations of the power low observed in submicron fragments as shown in Fig. 2.4 (dots in the upper left side of both panels). It has also to be considered that DLS is not a very sensitive technique for particles with refractive index not too different from that of water and for polydisperse colloids and the presence of smaller NPs in dynamic equilibrium with larger aggregates cannot be excluded.

Table 2.2. *DLS particles size from samples filtered through 1 μm filters.*

DLS particle size				**(nm)**
Simulated sea water (filtered 0.45 μm)				228 ± 20
DLS particle size, filtered < 1 μm				**(nm)**
Irradiated	PE-PP (NI)-0[a]	466 ± 25	(NI)-0[a]	318 ± 59
	PE-PP (I)-72	482 ± 86	PS (I)-72	337 ± 35
	PE-PP (I)-144	466 ± 93	PS (I)-144	356 ± 74
	PE-PP (I)-216	444 ± 69	PS (I)-216	275 ± 16
	PE-PP (I)-288	388 ± 80	PS (I)-288	253 ± 29
	PE-PP (I)-360	365 ± 55	PS (I)-360	242 ± 88
Non-Irradiated	PE-PP (NI)-0[a]	433 ± 19	PS (NI)-0[a]	340 ± 62
	PE-PP (NI)-360	313 ± 61	PS (NI)-360	280 ± 33
	PE-PP (NI)-720	521 ± 85	PS (NI)-720	405 ± 36

[a] (NI)-0 samples were taken after stirring in the absence of irradiation for 72 h

Finally, aliquots from the liquid remaining at the end of runs filtered through 1 μm pore size filters were subject to extraction and reprecipitation as described in the experimental section. The purpose was to obtain small pellets suitable for spectroscopic identification by means of micro-FTIR. The results are presented in Fig. 2.6. PE-PP and PS extracts allowed the identification of the main features of the polymers PE, PP and PS. The main are the stretching vibrations of -CH_2 at 2920 cm^{-1} and 2850 cm^{-1}, common to PE and PP with a shoulder at 2950 cm^{-1} from PP; the bending modes from -CH_3 in

PP at 1376 and from -CH_3 and -CH_2 in PP and PE respectively, the latter unresolved at 1465 cm^{-1}, and the -CH_2 rocking vibration of PE at 719 cm^{-1} are clearly shown in Fig. 2.6A. Fig. 2.6B shows the stretching vibrations of C-H bonds at 2850, 2918 and 3025 cm^{-1}, the peaks between 1600 and 700 cm^{-1} due to the deformations and vibrations of C–H bonds. Besides, the usual peaks from O-H and C=O moieties that were already present in the parent MPs increased in reprecipitated NPs.

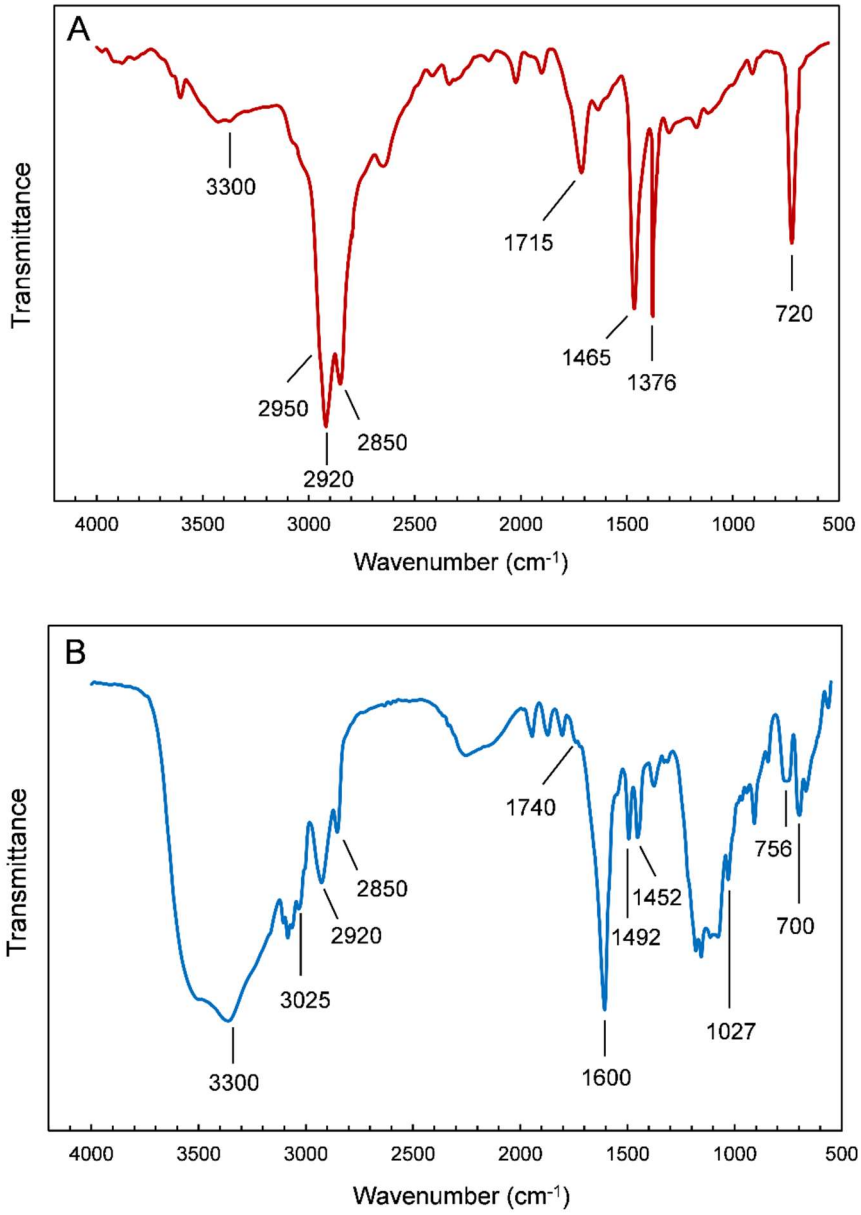

Figure 2.6. *Micro-FTIR spectra for the fragments < 1 µm filters indicating the peaks PE and PS. Experiment PE-PP (I)-360 (A) and PS (I)-360 (B).*

The concentration number of NPs is difficult to determine because of the presence of a background colloid from simulated seawater, but an estimation using the TOC data from Fig. 2.5 and considering particle size in the 200-400 nm range, as found in DLS measurements, yielded a number or NP particles in the 10^{11}-10^{13} NPs/g range. This figure is one to three orders of magnitude higher than that estimated elsewhere for LDPE pellets and is in agreement with the much higher generation of MP particles in the micron size range in the case of pre-aged marine plastic debris (Sorasan et al., 2021).

The fragmentation pattern of plastics in the environment is of outmost importance for the assessment of the environmental fate and possible impact of plastic debris. It is a well-known fact that UV exposure in combination with oxidants can lead to the embrittlement of the plastic surface. Mechanical forces would then act due to the action of currents or abrasion in contact with solid surfaces to induce fragmentation by a combination of surface ablation and particle break-up (Masry et al., 2021). The rate at which plastics degrade by fragmentation depends on the type of polymer EPS being the most easily fragmented and PE the hardest to break (Zhu et al., 2020). Apart from polymer type, shape and the presence of stabilizers affect the rate of fragmentation of plastics. Experiments with PE films without UV absorbing additives showed that UVA irradiation in the presence of atmospheric oxygen make them disappear into "invisible" fragments after a few months of exposure (Kalogerakis et al., 2017). Most environmental studies on plastics size distribution refer to fragments floating on the ocean surface and were conducted using Neuston nets with mesh size about 300 μm. For them, a peak of higher abundance in generally observed about 2 mm, with concentration rapidly declining for sizes < 1 mm (Cózar et al., 2014). However, theoretical fragmentation studies predict abundance-size distributions following a power law with scaling exponent equal to the spatial dimension of the fragments. Detailed characterization of samples collected from the North Atlantic subtropical gyre using mass distribution instead of number distribution confirmed a power-law decay with exponent about 1.5, similar to that found by Kooi and Koelmans for number concentrations (Kooi and Koelmans, 2019; ter Halle et al., 2016). The usual

interpretation of the observed divergence is that it is due to the selective removal of the smallest fragments by sinking upon biological colonization or due to their ingestion by marine organisms.

Clearly, plastic fragments break down into smaller pieces by the application of an energy input. Based on that, Aooki and Furue proposed an alternative explanation to the loss of small plastics by assuming that the energy required for fragmentation increases as particle size decreases (Aoki and Furue, 2021). The mechanism behind fragmentation-induced size distribution was also studied in a recent paper that used a probabilistic model for particle fragmentation. The authors assumed that the fragmentation rate depends on the size of fragments and predicts that downsizing slows down for small sizes due to a lower probability of fragmentation for small MPs (Wang et al., 2021). Therefore, there is theoretical background consistent with the scenario found in some environmental samples. However, our results showed that the degradation of marine debris in controlled environments yielded fragments with size distribution that closely fits into the theoretical three-dimensional scaling law (i.e., with an exponent 3 for the power law) and support the existence of mechanisms that deplete small particles like the biota-interaction theory. Our results also showed that most fragments produced during the ageing of plastic debris would be below current monitoring campaigns. Moreover, fragmentation results in the early production of very small and highly mobile fragments. Size is the most important factor determining the mobility of MPs through soil, and aquatic environments as well as their wind-driven transport in the atmosphere. Accordingly, new techniques are required for the routine monitoring of very small MPs and NPs. There are indications that the ecological risks posed by plastic is largely driven by small particles (Bucci et al., 2020). Small MPs and NPs may be internalized through epithelia, possibly bioaccumulate in tissues, and may undergo transfer through the food chain, eventually causing damage to human beings. Therefore, there is a need to obtain data on the environmental occurrence of plastic particles in the micron and sub-micron range.

2.4 Conclusions

We studied the generation of small MPs and NPs from the mechanical, and photochemical degradation of marine PE, PP and PS MPs debris. The number distribution of particles in the 1-100 μm range was assessed using laser diffractometry combined with flow cytometry. The results showed the generation of up to 10^5-10^6 particles/mg particles, mostly in the few microns size range: modal value < 2 μm, 98 % particles < 10 μm. Number particle size distributions followed a power law, log(abundance) = c – α log(size), with scaling exponent α = 3.0 ± 0.3 consistent with a three-dimensional fragmentation pattern. Photochemical ageing decreased the number of MPs and increased the carbon content of 1 μm filtrates, which was attributed to the generation of NPs and corresponded to particles in the 240-520 nm range. Our results showed that irradiation triggered the generation of NPs from MPs and were consistent with a scenario in which mechanical degradation led to a quick generation of small secondary MPs, subsequently fragmented into NPs by photochemical reactions.

2.5 Supplementary Material

Figure S2.1. *Microplastics used to feed the photoreactor: PE-PP (A), and PS (B).*

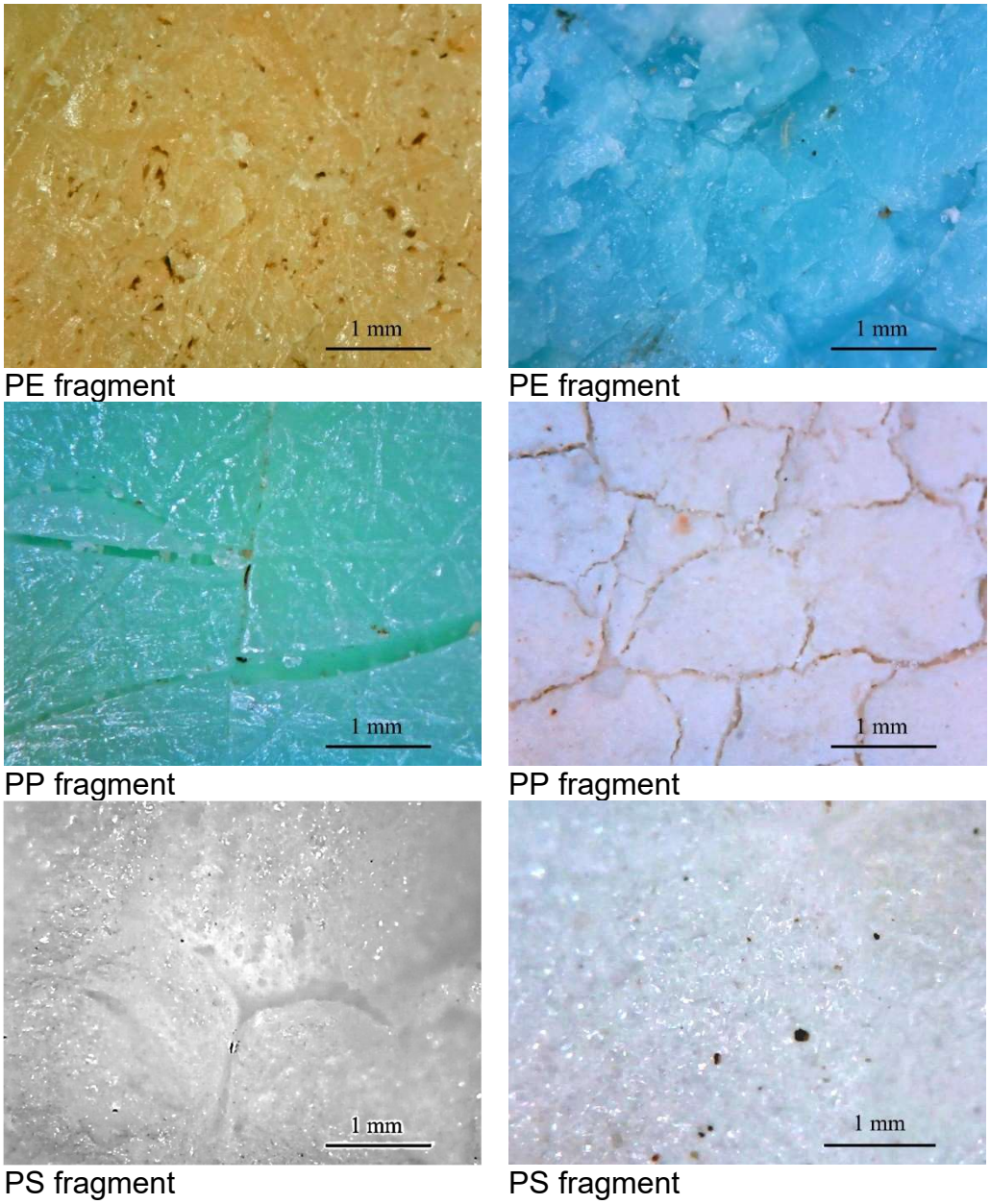

Figure S2.2. *Micrographs of some fragments of PE, PP and PS before irradiation.*

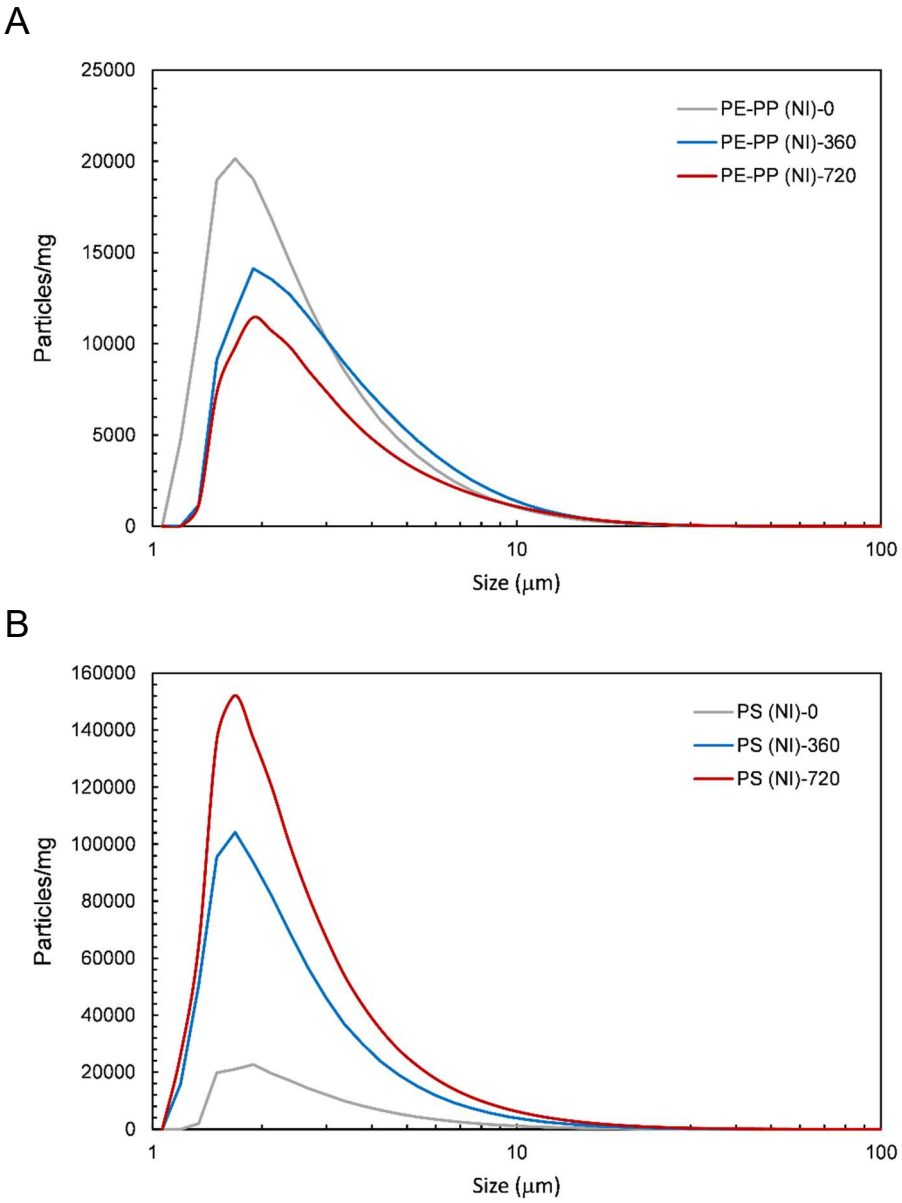

Figure S2.3. *Size distribution for particles produced during non-irradiated runs with PE-PP MPs (A) and PS MPs (B). PE-PP/PS (NI)-0 correspond to samples taken after 72 h under agitation in darkness.*

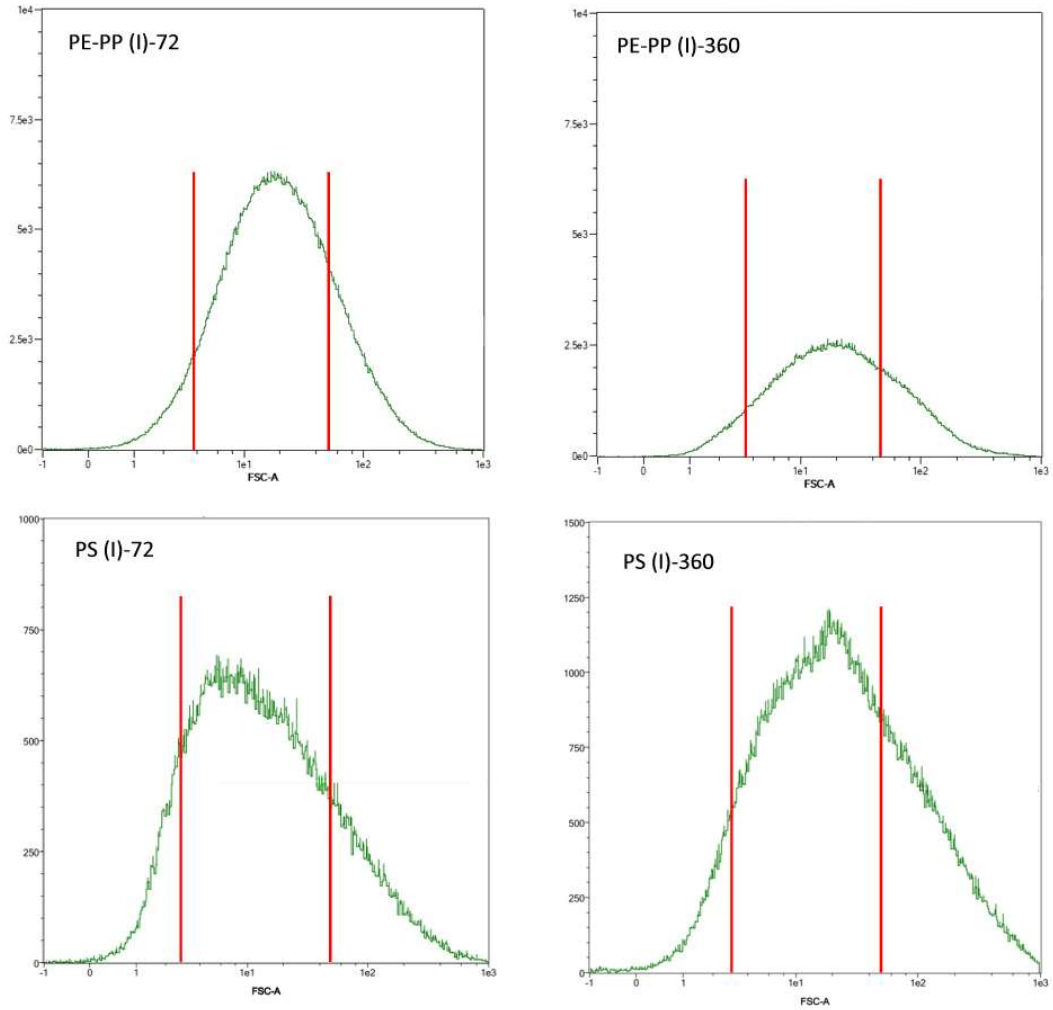

Figure S2.4. *Flow cytometry histograms for irradiated runs performed with PE-PP and PS after 72 h and 360 h. The red lines correspond to 1 µm and 10 µm particles.*

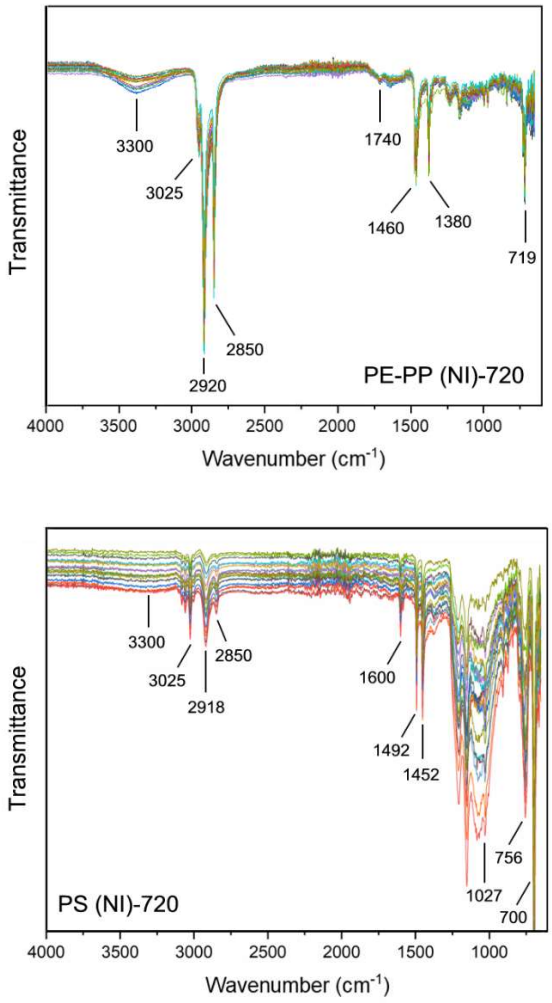

Figure S2.5. *ATR-FTIR spectra of the particulate material recovered after PE-PP (NI)-720, and PS (NI)-720 runs.*

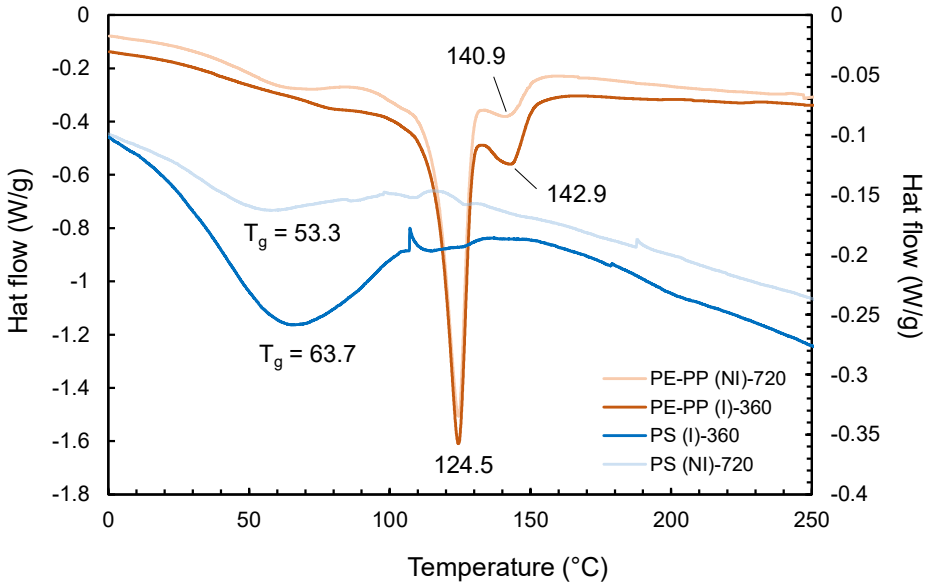

Figure S2.6. *DSC curves for the material recovered after completion of assays PE-PP (I)-360, PE-PP (NI)-720, PS (I)-360 and PS (NI)-720.*

2.6 References

Anastopoulos I, Pashalidis I, Kayan B, Kalderis D. Microplastics as carriers of hydrophilic pollutants in an aqueous environment. Journal of Molecular Liquids 2021: 118182.

Andrady AL. Microplastics in the marine environment. Marine pollution bulletin 2011; 62: 1596-1605.

Aoki K, Furue R. A model for the size distribution of marine microplastics: A statistical mechanics approach. PLOS ONE 2021; 16: e0259781.

ASTM. Standard Practice for Preparation of Substitute Ocean Water, ASTM D1141-98(2021). merican Society for Testing and Materials, 2021.

Auffan M, Rose J, Bottero J-Y, Lowry GV, Jolivet J-P, Wiesner MR. Towards a definition of inorganic nanoparticles from an environmental, health and safety perspective. Nature Nanotechnology 2009; 4: 634-641.

Brandon J, Goldstein M, Ohman MD. Long-term aging and degradation of microplastic particles: Comparing in situ oceanic and experimental weathering patterns. Marine Pollution Bulletin 2016; 110: 299-308.

Bucci K, Tulio M, Rochman CM. What is known and unknown about the effects of plastic pollution: A meta-analysis and systematic review. Ecological Applications 2020; 30: e02044.

Chamas A, Moon H, Zheng J, Qiu Y, Tabassum T, Jang JH, et al. Degradation rates of plastics in the environment. ACS Sustainable Chemistry & Engineering 2020; 8: 3494-3511.

Cózar A, Echevarría F, González-Gordillo JI, Irigoien X, Úbeda B, Hernández-León S, et al. Plastic debris in the open ocean. Proceedings of the National Academy of Sciences 2014; 111: 10239.

de Rond L, Coumans FAW, Nieuwland R, van Leeuwen TG, van der Pol E. Deriving extracellular vesicle size from scatter intensities measured by flow cytometry. Current Protocols in Cytometry 2018; 86: e43.

Edo C, Tamayo-Belda M, Martínez-Campos S, Martín-Betancor K, González-Pleiter M, Pulido-Reyes G, et al. Occurrence and identification of microplastics along a

beach in the Biosphere Reserve of Lanzarote. Marine Pollution Bulletin 2019; 143: 220-227.

Fotopoulou KN, Karapanagioti HK. Degradation of various plastics in the environment. In: Takada H, Karapanagioti HK, editors. Hazardous Chemicals Associated with Plastics in the Marine Environment. Springer International Publishing, Cham, 2019, pp. 71-92.

Gerritse J, Leslie HA, de Tender CA, Devriese LI, Vethaak AD. Fragmentation of plastic objects in a laboratory seawater microcosm. Scientific Reports 2020; 10: 10945.

GESAMP. Guidelines for the monitoring and assessment of plastic litter in the ocean. In: Kershaw PJ, Turra A, Galgani F, editors. Rep. Stud. GESAMP No. 99. IMO/FAO/UNESCO-IOC/UNIDO/WMO/IAEA/UN/UNEP/UNDP/ISA Joint Group of Experts on the Scientific Aspects of Marine Environmental Protection, 2019, pp. 130.

Gigault J, Halle At, Baudrimont M, Pascal P-Y, Gauffre F, Phi T-L, et al. Current opinion: What is a nanoplastic? Environmental Pollution 2018; 235: 1030-1034.

Gigault J, Pedrono B, Maxit B, Ter Halle A. Marine plastic litter: the unanalyzed nano-fraction. Environmental Science: Nano 2016; 3: 346-350.

Godoy V, Blázquez G, Calero M, Quesada L, Martín-Lara MA. The potential of microplastics as carriers of metals. Environmental Pollution 2019; 255: 113363.

González-Pleiter M, Tamayo-Belda M, Pulido-Reyes G, Amariei G, Leganés F, Rosal R, et al. Secondary nanoplastics released from a biodegradable microplastic severely impact freshwater environments. Environmental Science: Nano 2019; 6: 1382-1392.

Grause G, Chien M-F, Inoue C. Changes during the weathering of polyolefins. Polymer Degradation and Stability 2020; 181: 109364.

Gulmine JV, Janissek PR, Heise HM, Akcelrud L. Degradation profile of polyethylene after artificial accelerated weathering. Polymer Degradation and Stability 2003; 79: 385-397.

Hartmann NB, Hüffer T, Thompson RC, Hassellöv M, Verschoor A, Daugaard AE, et al. Are We Speaking the Same Language? Recommendations for a Definition and Categorization Framework for Plastic Debris. Environmental Science & Technology 2019; 53: 1039-1047.

Hiejima Y, Kida T, Takeda K, Igarashi T, Nitta K-h. Microscopic structural changes during photodegradation of low-density polyethylene detected by Raman spectroscopy. Polymer Degradation and Stability 2018; 150: 67-72.

Ioakeimidis C, Fotopoulou KN, Karapanagioti HK, Geraga M, Zeri C, Papathanassiou E, et al. The degradation potential of PET bottles in the marine environment: An ATR-FTIR based approach. Scientific Reports 2016; 6: 23501.

Jakubowicz I, Enebro J, Yarahmadi N. Challenges in the search for nanoplastics in the environment—A critical review from the polymer science perspective. Polymer Testing 2021; 93: 106953.

Kalogerakis N, Karkanorachaki K, Kalogerakis GC, Triantafyllidi EI, Gotsis AD, Partsinevelos P, et al. Microplastics generation: onset of fragmentation of polyethylene films in marine environment mesocosms. Frontiers in Marine Science 2017; 4.

Kooi M, Koelmans AA. Simplifying microplastic via continuous probability distributions for size, shape, and density. Environmental Science & Technology Letters 2019; 6: 551-557.

Masry M, Rossignol S, Gardette J-L, Therias S, Bussière P-O, Wong-Wah-Chung P. Characteristics, fate, and impact of marine plastic debris exposed to sunlight: A review. Marine Pollution Bulletin 2021; 171: 112701.

Mateos-Cárdenas A, O'Halloran J, van Pelt FNAM, Jansen MAK. Rapid fragmentation of microplastics by the freshwater amphipod *Gammarus duebeni* (Lillj.). Scientific Reports 2020; 10: 12799.

Mattsson K, Björkroth F, Karlsson T, Hassellöv M. Nanofragmentation of expanded polystyrene under simulated environmental weathering (thermooxidative degradation and hydrodynamic turbulence). Frontiers in Marine Science 2021; 7.

Napper IE, Thompson RC. Release of synthetic microplastic plastic fibres from domestic washing machines: Effects of fabric type and washing conditions. Marine Pollution Bulletin 2016; 112: 39-45.

Nguyen B, Claveau-Mallet D, Hernandez LM, Xu EG, Farner JM, Tufenkji N. Separation and analysis of microplastics and nanoplastics in complex environmental samples. Accounts of Chemical Research 2019; 52: 858-866.

Ojeda T, Freitas A, Birck K, Dalmolin E, Jacques R, Bento F, et al. Degradability of linear polyolefins under natural weathering. Polymer Degradation and Stability 2011; 96: 703-707.

Olmos D, Martín EV, González-Benito J. New molecular-scale information on polystyrene dynamics in PS and PS–BaTiO3 composites from FTIR spectroscopy. Physical Chemistry Chemical Physics 2014; 16: 24339-24349.

PlasticsEurope. Plastics – the Facts 2021: An analysis of European plastics production, demand and waste data. PlasticsEurope: Association of Plastics Manufacturers, Brussels, 2021.

Reynaud S, Aynard A, Grassl B, Gigault J. Nanoplastics: From model materials to colloidal fate. Current Opinion in Colloid & Interface Science 2022; 57: 101528.

Rizzo M, Corbau C, Lane B, Malkin SY, Bezzi V, Vaccaro C, et al. Examining the dependence of macroplastic fragmentation on coastal processes (Chesapeake Bay, Maryland). Marine Pollution Bulletin 2021; 169: 112510.

Sharma KD, Jain S. Municipal solid waste generation, composition, and management: the global scenario. Social Responsibility Journal 2020; 16: 918-948.

Song YK, Hong SH, Eo S, Han GM, Shim WJ. Rapid production of micro- and nanoplastics by fragmentation of expanded polystyrene exposed to sunlight. Environmental Science & Technology 2020; 54: 11191-11200.

Song YK, Hong SH, Jang M, Han GM, Jung SW, Shim WJ. Combined effects of UV exposure duration and mechanical abrasion on microplastic fragmentation by polymer type. Environmental Science & Technology 2017; 51: 4368-4376.

Sorasan C, Edo C, González-Pleiter M, Fernández-Piñas F, Leganés F, Rodríguez A, et al. Generation of nanoplastics during the photoageing of low-density polyethylene. Environmental Pollution 2021; 289: 117919.

Sorasan C, Ortega-Ojeda FE, Rodríguez A, Rosal R. Modelling the photodegradation of marine microplastics by means of infrared spectrometry and chemometric techniques. Microplastics 2022; 1.

ter Halle A, Ladirat L, Gendre X, Goudouneche D, Pusineri C, Routaboul C, et al. Understanding the fragmentation pattern of marine plastic debris. Environmental Science & Technology 2016; 50: 5668-5675.

Tian L, Chen Q, Jiang W, Wang L, Xie H, Kalogerakis N, et al. A carbon-14 radiotracer-based study on the phototransformation of polystyrene nanoplastics in water versus in air. Environmental Science: Nano 2019; 6: 2907-2917.

Torikai A, Takeuchi A, Fueki K. The effect of temperature on the photo-degradation of polystyrene. Polymer Degradation and Stability 1986; 14: 367-375.

Uheida A, Mejía HG, Abdel-Rehim M, Hamd W, Dutta J. Visible light photocatalytic degradation of polypropylene microplastics in a continuous water flow system. Journal of Hazardous Materials 2021; 406: 124299.

Villanova-Solano C, Díaz-Peña FJ, Hernández-Sánchez C, González-Sálamo J, González-Pleiter M, Vega-Moreno D, et al. Microplastic pollution in sublittoral coastal sediments of a North Atlantic island: The case of La Palma (Canary Islands, Spain). Chemosphere 2022; 288: 132530.

Wang L, Li P, Zhang Q, Wu W-M, Luo J, Hou D. Modeling the Conditional Fragmentation-Induced Microplastic Distribution. Environmental Science & Technology 2021; 55: 6012-6021.

Yakimets I, Lai D, Guigon M. Effect of photo-oxidation cracks on behaviour of thick polypropylene samples. Polymer Degradation and Stability 2004; 86: 59-67.

Zhang K, Hamidian AH, Tubić A, Zhang Y, Fang JKH, Wu C, et al. Understanding plastic degradation and microplastic formation in the environment: A review. Environmental Pollution 2021; 274: 116554.

Zhou X-X, He S, Gao Y, Li Z-C, Chi H-Y, Li C-J, et al. Protein corona-mediated extraction for quantative analysis of nanoplastics in environmental waters by pyrolysis gas chromatography/mass spectrometry. Analytical Chemistry 2021; 93: 6698-6705.

Zhu L, Zhao S, Bittar TB, Stubbins A, Li D. Photochemical dissolution of buoyant microplastics to dissolved organic carbon: Rates and microbial impacts. Journal of Hazardous Materials 2020; 383: 121065.

3 Modelling the photodegradation of marine microplastics by means of infrared spectrometry and chemometric techniques

Abstract

This work investigated the structural and chemical changes of plastics undergoing accelerated ageing upon irradiation that simulated the ultraviolet part of solar radiation for a five-year period. The plastics selected were polyethylene (PE) and polypropylene (PP) microplastic debris sampled from a sandy beach as well as pure pellets and fragments of objects made of the same polymers. We recorded Fourier Transform Infrared (FTIR) spectra at prescribed intervals during the irradiation procedure. The spectra were used to study the evolution of the absorption peaks usually associated with the environmental ageing of polyolefins, namely the peaks of hydroxyl and carbonyl stretching, the peaks relating to the presence of double bonds, and those associated to the crystallinity of PE and the tacticity of PP. The results showed that none of the usual degradation indexes followed a clear trend with increasing exposure and that the evolution of absorption peaks was not consistent among different fragments. We used the Orthogonal Partial Least Squares Discriminant Analysis (OPLS-DA) method to process the whole information contained in FTIR spectra in response to the chemical changes occurring during photochemical ageing. The results showed that FTIR spectra contained sufficient information to cluster samples according to the irradiation received. Variable Importance of the Projection (VIP) analyses showed that the information for discriminating among different exposures was mainly contained in the absorption peaks corresponding to the

hydroxyl and carbonyl stretching absorptions. The chemometric models had large determination coefficients, despite the large number of variables involved and could be applied to assess the environmental fate of plastics under environmental stressors.

3.1 Introduction

The worldwide production of the different types of plastic has been steadily increasing since the onset of their industrial manufacture to reach a maximum of 368 million tonnes in 2019. In 2020, the production slightly dropped to 367 million tonnes, only one million tonnes less, but this was the first decrease recorded in the history of the plastics industry (PlasticsEurope, 2021). Despite the efforts made to close the plastic cycle, the annual rate of plastic entering the environment is still estimated at about 40 million tonnes from which 11 million tonnes correspond to macro- and microplastic (MP) waste that reaches the ocean(Lau et al., 2020). Another calculation estimated that two-thirds of the plastic ever produced has already been released to the environment. The same study highlighted the unnecessary abuse of plastic by the fact that about 40% of the global plastic production is meant for packaging, mostly for immediate or near immediate disposal (Pinto-da-Costa et al., 2020). Some sources of plastic pollution are more difficult to avoid, like the spreading of plastic fragments and synthetic fibres due to the wearing of goods during use (Napper et al., 2016). The presence of intentionally added MPs in certain products is another source of pollution, but the accumulation of plastic in environmental compartments is by far a problem of inadequate waste management rather than a limitation associated to plastic itself (OECD, 2022). In fact, synthetic polymers are extremely useful materials, with unique properties and relatively low energy content making prohibitive the environmental cost of replacing them by alternatives like glass, paper, or natural substances (North et al., 2013).

Plastic disseminated into the environment accumulates due to its chemical persistence, but eventually undergoes degradation and fragmentation processes under environmental stressors. Previous studied have shown that the MPs floating on the sea surface were brittle, which was attributed to the leaching of plasticizers (Carpenter et al., 1972). It has been generally established that photoinitiated oxidative degradation is the main mechanism by which plastics suffer environmental ageing (Chamas et al., 2020). Photochemical degradation combined with different hydrolysis and oxidation reactions results in the formation of oxygenated moieties like carboxylic end groups in the fragments resulting from the breaking of polymer backbones (Gewert et al., 2015). Another problem is that

the loss of stabilizer additives affects degradation rate in a different way depending on the exact composition of each plastic item, making it difficult to predict the degradation rates of fragments with different chemical history (Chamas et al., 2020).

Vibrational spectroscopy, in this case infrared (IR), is an ideal tool extensively used for the elucidation of chemical and physical properties of polymers, the qualitative and quantitative analysis of polymer blends, and the tracking of their degradation processes (Gopanna et al., 2019). Bond indexes calculated from FTIR spectra have been used to assess the changes suffered by plastics during weathering. However, their usefulness is limited because of the large variability observed for different plastics and ageing conditions (Brandon et al., 2016). Our hypothesis is that the information contained in the spectra of aged plastics can be revealed using chemometric modelling. In this work, we used MPs from marine origin and exposed them to accelerated ageing simulating up to five years of additional UV solar exposure. The MPs consisted of polyethylene (PE) and polypropylene (PP), sampled from a sandy beach as well as pure pellets and fragments of PE and PP obtained from plastic goods. The purpose of this study was to assess the possibility of obtaining information about the environmental history of polyolefin MPs using mid-IR spectroscopy and chemometric techniques.

3.2 Materials and Methods

3.2.1 Materials and experimental procedure

The environmental plastic fragments used were MPs collected from the sandy beach Ámbar, located in the North coast of La Graciosa, a small island belonging to the Chinijo Archipelago, Canary Islands, Spain. La Graciosa Island is a specially protected area, declared Biosphere Reserve by UNESCO. Accordingly, the beach has very limited human pressure, but it suffers from severe plastic pollution driven with the Canary Current from the North Atlantic Gyre. The MPs sampled in from Ámbar beach were mostly PE and PP, which represented 84% and 11% of all plastic particles identified as shown elsewhere (Edo et al., 2019). A total number of 30 marine MP samples (23 PE and 7 PP) were selected with different shapes and colours from the Ámbar beach. Two pure Goodfellow commercial pellets (one low-density polyethylene, LDPE, and one PP) free of additives or charges, natural colour, 2-3 mm were also studied. In addition, 4 fragments of PE (LDPE and high-density polyethylene, HDPE) and PP obtained from commercial goods were also used for simulated ageing experiments. The samples were carefully washed with HPLC grade methanol (CAS 67-56-1, Merck) and ultrapure water (Milli-Q Q-POD Ultrapure Water System) and distributed in four 90 mm diameter glass containers filled with 250 mL simulated seawater, which was prepared according to ASTM D1141-98 using pure chemicals (Merck and Fisher Scientific) to reach a final density of 1.025 g/mL measured at 15 °C (ASTM D1141-98 Standard, 2021). The containers were placed on a gyratory shaker operating at 30 rpm for uniform exposure.

Accelerated ageing was simulated using a 150 W medium-pressure mercury lamp (Peschl Ultraviolet NovaLight TQ150) emitting in the 297-579 nm range. The exposure time was calculated from NASA's EarthData readings for the Canary Islands (https://power.larc.nasa.gov/data-access-viewer/), namely 5.62 kWh m^{-2} day^{-1} (234 W m^{-2}), 5% of which corresponds to UVA+UVB (or 280-400 nm). Lamp irradiance was 1350 W m^{-2} (UVA+UVB or 280-400 nm) measured using a StellarNet Modular Spectrometer equipped with SpectraWiz OS v5.33 software. Therefore, the system needed 74 h of exposure to simulate one year of solar UV irradiation, which were approximated by 3 days

of continuous irradiation. The near-UV light quanta (400–290 nm) have energies from 3.1 to 4.3 eV which correspond to 72–97 kcal/mol, which was sufficient for breaking most of the chemical bonds in the polymer samples (Rånby, 1989). The study was carried for out over a total irradiation time of 360 h, simulating five-year of solar UVA+UVB exposure.

3.2.2 Analyses

Measurements were taken on each specimen every 72 h. Samples are denoted in what follows as zero (Y0, initial), and Y1 (72 h) to Y5 (360 h). After every 72-h period, the samples were washed with ultrapure water, dried at 50 °C for 12 h, and stabilized at room temperature for another 12 h before recording FTIR spectra. The spectra were obtained in a Nicolet iS10 Attenuated Total Reflectance Fourier Transform Infrared (ATR-FTIR), apparatus (ThermoFisher) with a Smart iTR-Diamond module, and OMNIC software. The operating parameters were: 4000-650 cm^{-1} range; 4 cm^{-1} resolution; and 16 acquisitions (co-added scans). Seven spectra were taken for each sample; hence, 252 spectra were generated for every irradiation time, which resulted in 1512 spectra/sample. This created a matrix of 1512 rows (number of observations/items/objects) and 6950 columns (number of variables/wavelengths) that was analysed using chemometrics tools. The spectra corresponding to Y0 (or initial) were recorded from specimens directly taken from the beach, after cleaning and drying. All changes due to simulated ageing were recorded on that basis and for every individual fragment.

The photodegradation of polyolefins has been shown to start by the photolytic cleavage of chemical bonds in the polymer backbone to form radical pairs (Norrish Type I reaction) or pairs of saturated and unsaturated chain ends (Norrish Type II reaction) (Jabarin et al., 1994; Sing et al., 2008). The process is followed by the reaction with molecular oxygen to produce peroxy radicals, which abstract hydrogen atoms to form hydroperoxide groups. Hydroperoxides break forming pairs of alkoxy and hydroxyl radicals, which proceed via

radical chain mechanisms in complex series of initiation, propagation, chain branching, and termination reactions (Agboola et al., 2017). The degradation produces a large variety of oxygenated moieties. Specifically concerning PE, the relevant absorbance peaks in the mid-IR correspond to the ester carbonyl bond at 1740 cm^{-1}, the keto-carbonyl bond at 1715 cm^{-1}, and the terminal and internal double bonds at 1650 cm^{-1} and 908 cm^{-1} respectively. The absorbance intensities (I) were computed relative to the methylene bond peak (in plane CH_2 deformation) at 1465 cm^{-1} using the following expressions (Albertsson et al., 1987):

- Keto-Carbonyl Bond Index (KCBI) = I_{1715}/ I_{1465}
- Ester-Carbonyl Bond Index (ECBI) = I_{1740}/I_{1465}
- Vinyl Bond Index (VBI) = I_{1650}/I_{1465}
- Internal Double Bond Index (IDBI) = I_{908}/I_{1465}

Crystallinity, $X(\%)$ was measured for PE using the following expression in which I_a and I_b are the absorbance for the bands at 1474 cm^{-1} and 1464 cm^{-1}, respectively (Zerbi et al., 1989):

$$X(\%) = 100\left[1 - \left(\frac{I_b - \frac{I_a}{1.233}}{I_a + I_b}\right)\right] \quad (2)$$

Concerning PP, the photodegradation process was tracked using the absorbance intensities of ester (1748 cm^{-1}) and methyl (1377 cm^{-1}) groups. The absorbance intensity corresponding to the bending of methylene group at 1456 cm^{-1} was used as a reference because, as in the case of the 1465 cm^{-1} peak for PE, the absorbance recorded for the same fragments did not show significant differences (p-value < 0.05). Besides, the isotacticity index of PP was computed using the bands as 997 cm^{-1} and 973 cm^{-1} (Arkatkar et al., 2009) . Accordingly, the following parameters were calculated:

- Ester-Carbonyl Bond Index (ECBI): I_{1748}/I_{1456}

- Methyl Group Index (MGI): I_{1377}/I_{1456}
- Isotacticity, I(%) computed as (I_{997}/I_{973}) x100

The generation of hydroxyl groups during the photodegradation process was assessed by monitoring the evolution of the hydroxyl group band from 3100 cm^{-1} to 3800 cm^{-1} (Adothu et al., 2021). Specifically, we defined three hydroxyl indexes (OHi) computed using the same absorption peak as reference, which was taken at 1465 cm^{-1} for PE and 1456 cm^{-1} for PP. The selected wavenumber ranges were: 3360 cm^{-1} for OH stretching in the case of intramolecular hydrogen bonding, and 3637 cm^{-1} and 3623 cm^{-1} for primary and non-primary OH groups.

Before data analysis, all the spectra received a pre-processing transformation using the following sequence: baseline and offset correction, standard normal variate (SNV) normalization, and Savitzky-Golay smoothing (2nd order polynomial and 7 points with symmetric Kernel), using The Unscrambler v10.4 software (AspenTech, Massachusetts, USA).

3.2.3 Statistics

The spectral data were analysed using orthogonal partial least squares discriminant analysis (OPLS-DA). OPLS-DA is a statistical modelling tool that provides insights into the separations among experimental groups, in this case, based on data containing high-dimensional spectral measurements with multicollinear and noisy variables (Chung et al., 2019; Worley et al., 2016). This method combines orthogonal signal correction (OSC) and partial least squares discriminant analysis. The goodness of fitting is assessed by means of the cross-validation parameters, R^2X, R^2Y and Q^2, representing the explained variance and the predictive capability of the model. R^2X and R^2Y indicate the fraction of variance of the

X and Y matrices, and Q^2 gives the predictive power of the model. The confidence level of the parameters was set to 95%, and the significance level for the Hotelling's T^2 was set to 0.05 (Bylesjö et al., 2006). The software also returns the analysis of Variable Importance of the Projection (VIP). These plots summarize the importance of the variables to explain X and correlate Y, the part of X related to Y, and the part of X orthogonal to Y.

3.3 Results and discussion

3.3.1 Photodegradation indexes

The evolution of degradation indexes, crystallinity, and isotacticity was tracked using seven FTIR spectra per sample and per irradiation time as indicated in the preceding section. The results are shown in Figure S3.1, and in Tables S3.1 and S3.2 (Supplementary Materials, SM) for PE and PP respectively. Samples before treatment are represented as Y0, while YN stands for samples after irradiation equivalent to N (1 to 5) years of solar UV exposure. The values for the outliers were identified and shown in Table S3.3 (SM). (Representative spectra before and after irradiation are shown in Figure S3.2, SM.) High values of KCBI and ECBI are observed, for example, for sample PE-Mar-22, for which the intensity was high throughout all the irradiation time. However, most MP fragments did not follow a clear trend, although a maximum in KCBI and ECBI was usually observed after the first 72 h of irradiation, equivalent to one year of solar exposure. The results also showed a slight tendency of PE crystallinity to decrease (Figure S3.1e). Generally, the crystalline content is expected to increase because of the higher susceptibility of the amorphous fraction to the photooxidation (Hiejima et al., 2018). However, the results available in the literature do not always show crystallinity increase with ageing, and in some cases the opposite behaviour has been observed, which could be due to the formation of bulky groups that decrease polymer packing (Carrasco et al., 2001). Concerning PP isotacticity (Figure S3.1h) the results showed a decrease with irradiation time. This result can be interpreted as the consequence of the formation under oxidation conditions of tertiary radicals in carbon atoms, which temporarily lose their sp^3 configurations and, therefore, their stereospecificity (Iedema et al., 2021).

The effect of photochemical ageing on degradation indexes was clearer when depicting changes in indexes, rather than absolute values. Figures 3.1a and b show Δ(KCBI+ECBI)

and Δ(VBI) between two consecutive measurements. A complex pattern could be observed in which carbonyl indexes increased at the beginning and the end of irradiation with a decrease for intermediate exposures. The evolution of OH indexes displayed a slightly downward trend, difficult to appreciate in Figure S3.1, but clearer depicted in the incremental form of Figure 3.1c, that shows the differences in OHi-3360+3623+3637 between two consecutive one-year irradiation periods. Most of the variability was due to OHi-3360 associated to intramolecular hydrogen bonding, while OH stretching from primary and non-primary alcohols remained with slight changes. A similar absence of obvious pattern was seen for PP isotacticity (Figure 3.1d).

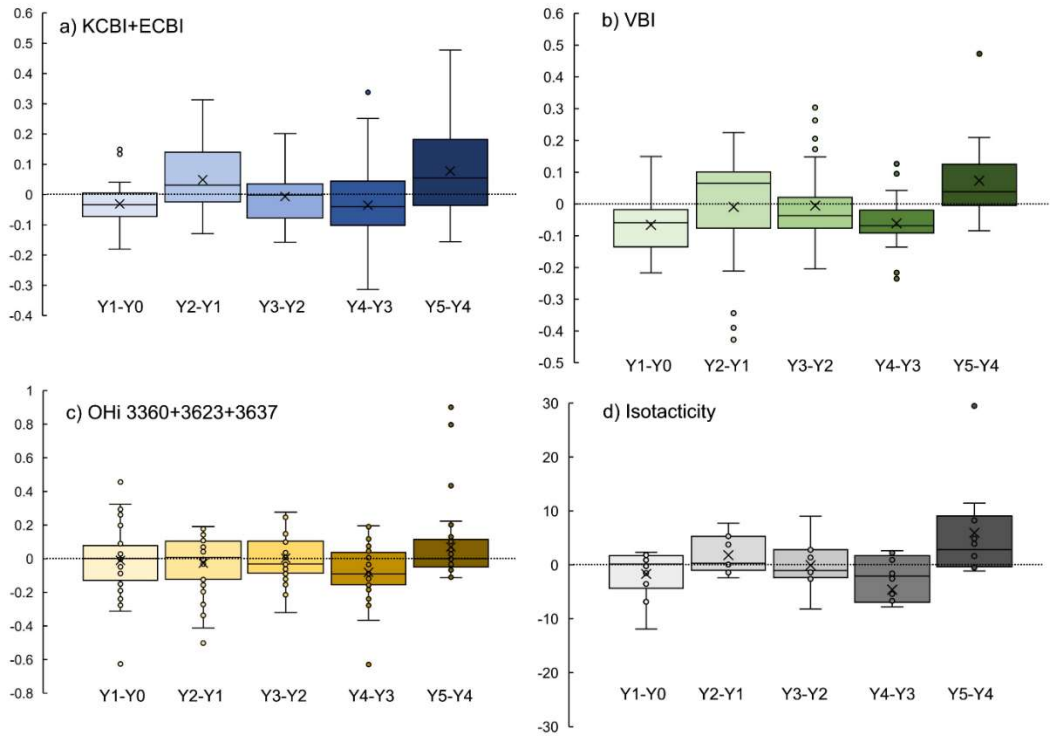

Figure 3.1. *Variation of degradation indexes every 72 h of irradiation (equivalent to one year of solar exposure) for a) KCBI – Keto Carbonyl Bond Index + ECBI – Ester Carbonyl Bond Index for PE; and b) VBI – Vinyl Bond Index for PE; c) Variation of Hydroxyl Bond Indexes for PE and PP (all specimens); and d) Changes in PP Isotacticity.*

3.3.2 Orthogonal Partial Least Square-Discriminant Analysis (OPLS-DA)

This study used OPLS-DA with unit variance autoscaling, cross-validation, and autofit modes in search for the maximum number of valid predictive and orthogonal components. Several models were created using the following classes: Polymer (PE and PP), Origin (new pellets, fragments of objects, and marine debris), Colour (red, green, blue, black, white, and translucent), Irradiation Time (Y0 and YN), and Shape (Fragment [3D], plate [2D], and rod [1D]) (Rosal et al., 2021). The models calculated for all samples had a root mean square error of estimation (RMSEE) in the 0.033-0.250 range, and a root mean square error of cross validation (RMSECV) in the 0.051-0.367 range. Additional models were calculated for the classes Origin (commercial pellets, fragments of objects, and marine debris) and Polymer (PE and PP). The results are shown in Table 3.1.

Table 3.1. *OPLS-DA parameters obtained from the different models for all the samples and their subsets by Origin (commercial pellets, fragments of objects, and marine debris) and Polymer (PE and PP).*

Id.	Group class	Spectra	Descriptive components	Orthogonal components	R^2X (cum)	R^2Y (cum)	Q^2 (cum)	RMSEE	RMSECV
1	*All Samples*								
Polymer		1512	6	16	0.931	0.749	0.710	0.094	0.102
Origin		1512	2	13	0.912	0.946	0.938	0.051	0.051
Color		1512	5	14	0.926	0.576	0.534	0.250	0.259
Irradiation Time		1512	5	17	0.932	0.714	0.679	0.186	0.201
Shape		1512	2	14	0.915	0.967	0.962	0.033	0.367
2	*Commercial pellets*								
Polymer		84	1	3	0.793	0.977	0.970	0.079	0.087
Irradiation Time		84	5	5	0.925	0.714	0.602	0.246	0.264
3	*Fragments of objects*								
Polymer		168	2	6	0.950	0.943	0.912	0.130	0.157
Color		168	1	3	0.882	0.970	0.958	0.088	0.103
Irradiation Time		168	5	3	0.943	0.568	0.497	0.271	0.275

4	***Marine debris***							
Polymer	1260	1	5	0.832	0.836	0.819	0.178	0.187
Color	1260	5	14	0.933	0.565	0.519	0.161	0.185
Irradiation time	1260	5	17	0.939	0.752	0.710	0.161	0.180
5	***PE***							
Polymer	1050	3	15	0.921	0.948	0.935	0.044	0.046
Origin	1050	2	13	0.907	0.962	0.954	0.048	0.049
Irradiation Time	1050	5	22	0.942	0.888	0.848	0.078	0.110
Color	1050	5	13	0.924	0.611	0.556	0.228	0.024
Shape	1050	2	13	0.906	0.964	0.957	0.046	0.048
6	***PP***							
Polymer	462	2	11	0.907	0.947	0.916	0.050	0.067
Origin	462	2	11	0.907	0.947	0.916	0.050	0.067
Irradiation Time	462	5	16	0.930	0.849	0.774	0.162	0.184
Color	462	3	9	0.902	0.755	0.693	0.185	0.210
Shape	462	1	10	0.896	0.979	0.957	0.042	0.060

The effect of photo-oxidative degradation was clear in the models with the group class Irradiation Time. Figures 3.2a (a1, a2, and a3) show the OPLS-DA score scatter plots for PE+PP, PE, and PP at different irradiation times. The plots write down that the information contained in the FTIR spectra allowed grouping the specimens as a function of UV exposure or irradiation time. This result was showed by a relationship between polymer type (projected X dataset) and exposure (Y, categorical variable).

a.1) PE + PP **a.2) PE** **a.3) PP**

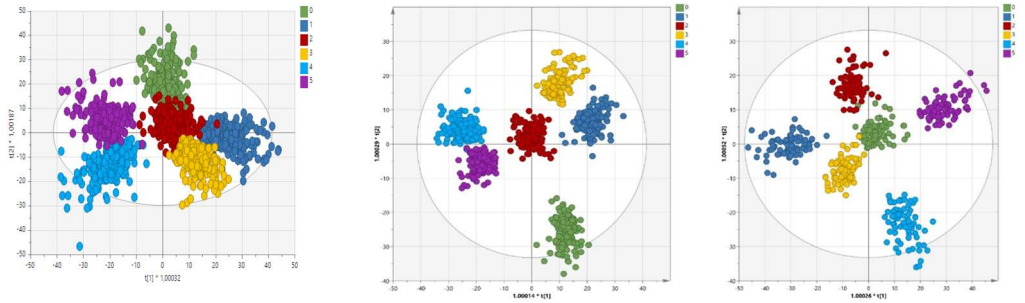

b.1) PE + PP **b.2) PE** **b.3) PP**

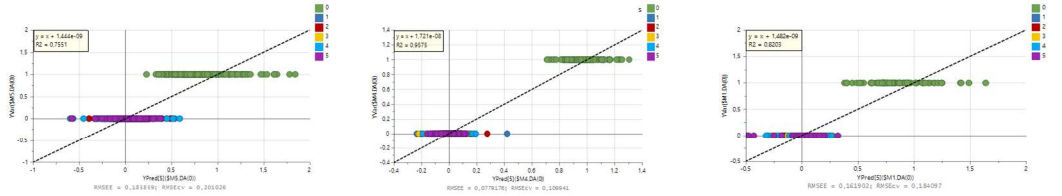

c.1) PE + PP

PE+PP	SS	DF	MS	F	p	SD
Total corr.	7555	7555	1			1
Regression	5151,96	220	23,418	71,4808	0	4,83922
Residual	2403,04	7335	0,327612			0,572374

c.2) PE

PE	SS	DF	MS	F	p	SD
Total corr.	5245	5245	1			1
Regression	4424,68	270	16,3877	99,3862	0	4,04817
Residual	820,323	4975	0,164889			0,406065

c.3) PP

PP	SS	DF	MS	F	p	SD
Total corr.	2305	2305	1			1
Regression	1754,44	210	8,35447	31,7905	0	2,89041
Residual	550,561	2095	0,262798			0,512638

Figure 3.2. *OPLS-DA score scatter plots for the models with PE and PP together (a1), PE (a2), and PP (a3); OPLS-DA Predicted vs. Observed plots for the PE+PP (b1), PE (b2), and PP (b3) models; and CV-ANOVA parameters for the models PE+PP (c1), PE (c2), and PP (c3) models.*

Figures 3.2b (b1, b2, and b3) show the OPLS-DA predicted vs. observed regression plots for the models. For the PE+PP model, the determination coefficient (R^2) was 0.7551, RMSEE was 0.1859, and RMSECV was 0.2010. The fitting parameters improved for PE (R^2 = 0.9575, RMSEE = 0.0779, and RMSECV = 0.1099), and PP (R^2 = 0.8203, RMSEE = 0.1614, and RMSECV = 0.1841). These results showed that the OPLS-DA models were rather robust, with good data fitting. Figures 3.2c (c1, c2, and c3) display the results for CV-ANOVA analyses based on the cross-validation process for the estimation of independent predictors and predictive residuals. The three models showed CV-ANOVA

p-value < 0.05 confirming the existence of significant differences and supporting the validity and robustness of the three models. Next, the data representing different extent of the photo-oxidation process were selected one by one (Y1, Y2, Y3, Y4, and Y5) and a comparative analysis was performed group by group, against the data before irradiation (Y0). This comparison procedure is summarised in Figures 3.3b1 to 3.3b5 for PE, and Figures 3.4b1 to 3.4b5 for PP, respectively. These difference plots indicate how much every band (in the respective group) contributed to the model, the larger the band's bar, the larger its contribution to the model. The contribution threshold was set to 0.5 as default, hence, contribution values > 0.5 are marked in blue for Y0, red for Y1 to Y5, and orange if the bars contribution values are larger than 3StdDev (three times the overall standard deviation).

The developed models shed light on the information contained in the absorbance peaks used for the calculation of the degradation indexes. Figure 3.3 (for PE) and Figure 3.4 (for PP) show the main changes in the spectra explaining the observed variability. For PE, the differences regarding the bands at 3623 cm^{-1} and 3637 cm^{-1} (OH stretching), were significant (Score contribution > 0.5) for Y1 and reached its maximum for Y3 (Score contribution > 0.75). The opposite correlation was observed for the absorption at 1650 cm^{-1} attributed to the terminal double bonds. In the case of PP, the absorption corresponding to the OH stretching was very significant after Y1 (Score contribution > 0.75) to decreased thereafter until a negative correlation at Y5. Besides, the carbonyl stretching absorption at 1748 cm^{-1} reached scores > 0.75 for PP after the first year of equivalent exposure (Y1) to follow a complex pattern thereafter.

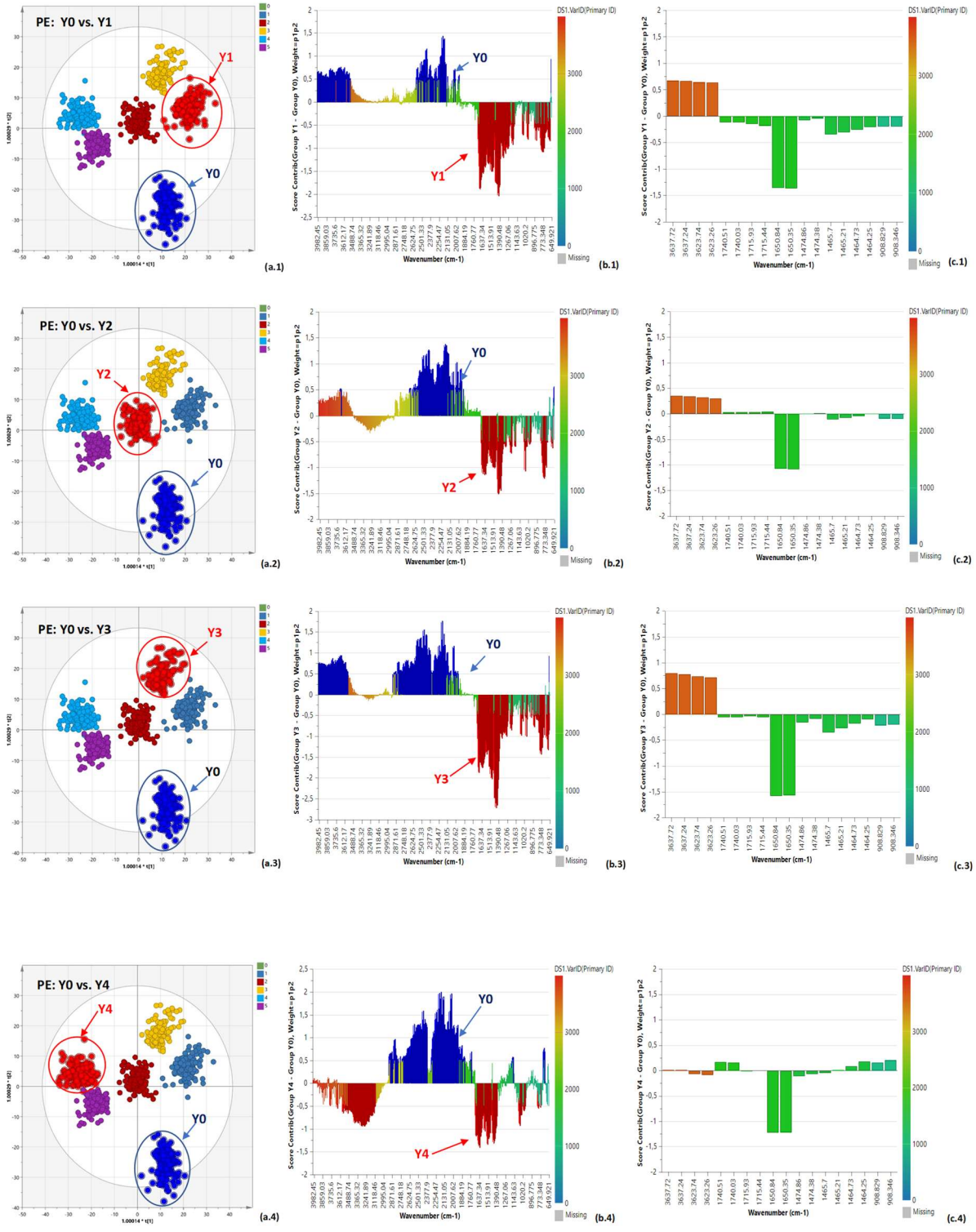
PE: Y0 vs. Y1
Y1
Y0
(a.1)
Y0
Y1
(b.1)
(c.1)
PE: Y0 vs. Y2
Y2
Y0
(a.2)
Y0
Y2
(b.2)
(c.2)
PE: Y0 vs. Y3
Y3
Y0
(a.3)
Y0
Y3
(b.3)
(c.3)
PE: Y0 vs. Y4
Y4
Y0
(a.4)
Y0
Y4
(b.4)
(c.4)
Wavenumber (cm-1)
Missing

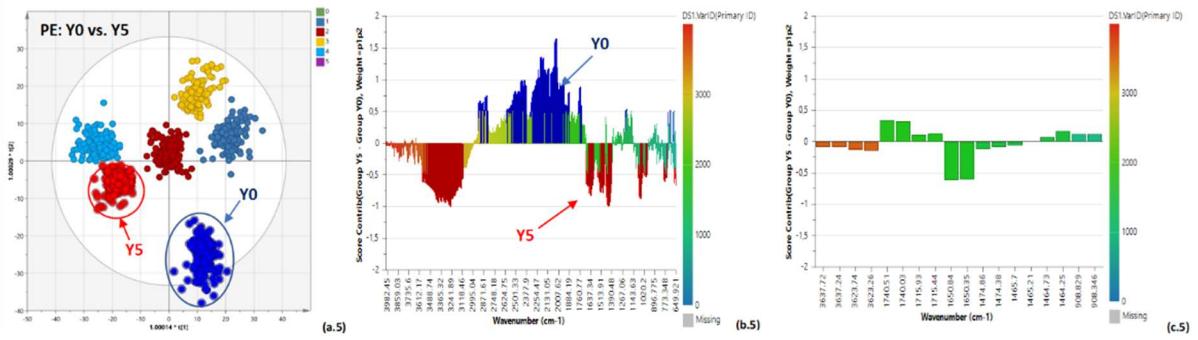

Figure 3.3. *Discrimination sequence for the PE models (rows). OPLS-DA score scatter plots showing the two selected groups being compared (left column); contribution (comparison) plots for the pair of selected groups (centre column), where the most important bands (contribution values > 0.5) are marked in blue for Y0, red for Y1 to Y5, and orange if the bars contribution values are larger than 3StdDev (StdDev = overall standard deviation); and contribution (comparison) plots for the selected variables from every group (right column). According to that sequence, the PE groups were compared as follows (from top of bottom): Y0 vs. Y1 (3.3[a1-b1-c1]), Y0 vs. Y2 (3.3[a2-b2-c2]), Y0 vs. Y3 (3.3[a3-b3-c3]), Y0 vs. Y4 (3.3[a4-b4-c4]), and Y0 vs. Y5 (3.3[a5-b5-c5]).*

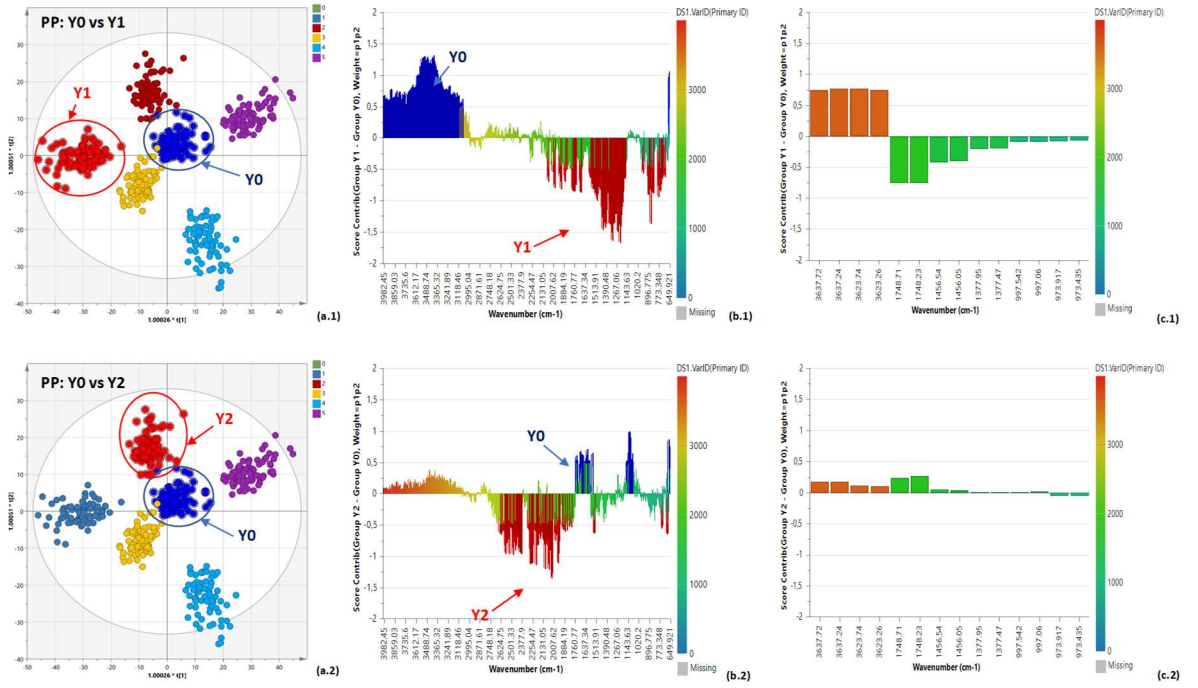

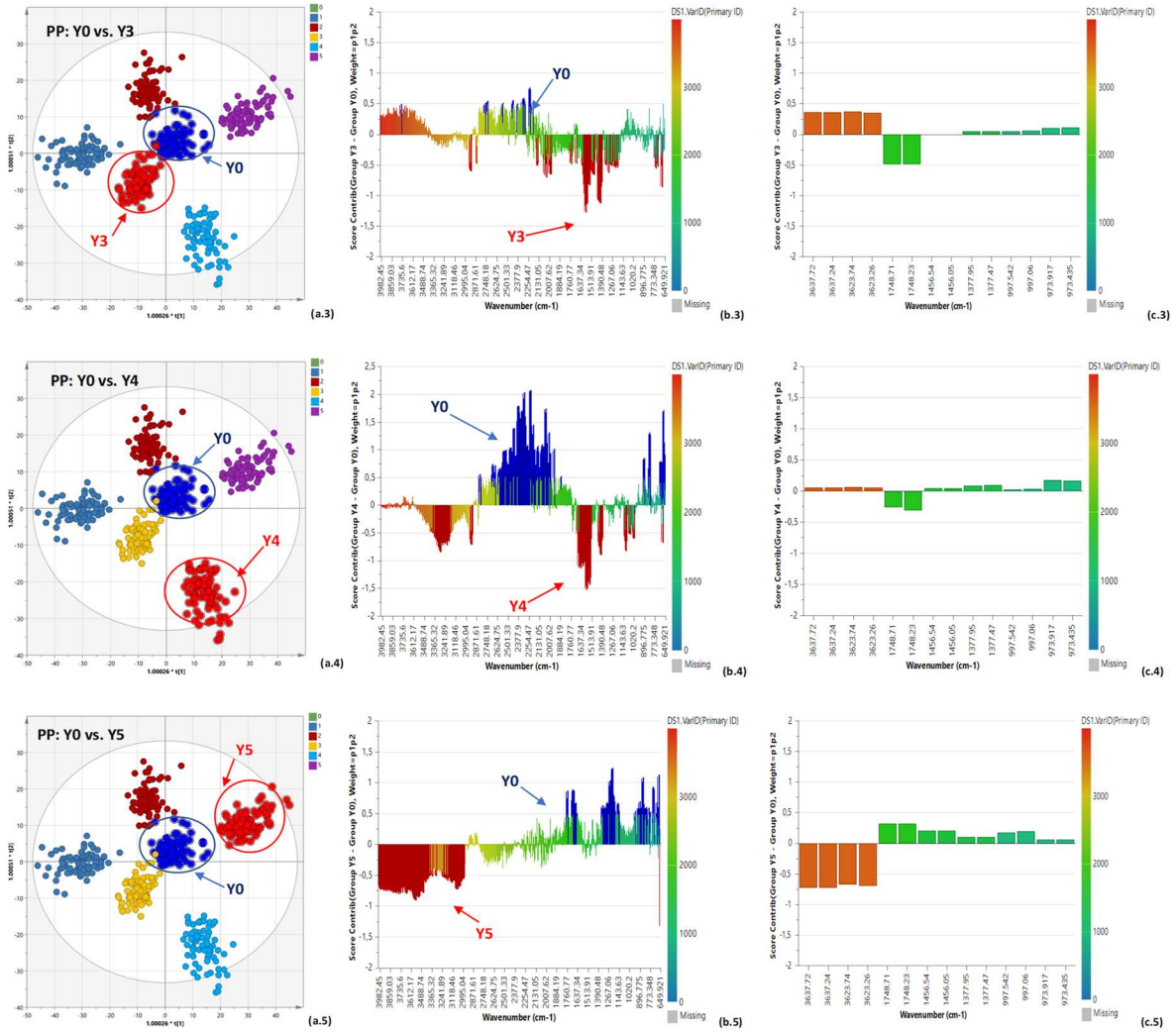

Figure 3.4. *Discrimination sequence for the PP models (rows). OPLS-DA score scatter plots showing the two selected groups being compared (left column); contribution (comparison) plots for the pair of selected groups (centre column), where the most important bands (contribution values > 0.5) are marked in blue for Y0, red for Y1 to Y5, and orange if the bars contribution values are larger than 3StdDev (StdDev = overall standard deviation); and contribution (comparison) plots for the selected variables from every group (right column). According to that sequence, the PP groups were compared as follows (from top of bottom): Y0 vs. Y1 (3.4[a1-b1-c1]), Y0 vs. Y2 (3.4[a2-b2-c2]), Y0 vs. Y3 (3.4[a3-b3-c3]), Y0 vs. Y4 (3.4[a4-b4-c4]), and Y0 vs. Y5 (3.4[a5-b5-c5])*

An added insight into the drivers of the variance was provided by VIP plots. Figures 3.5 (a1, b1, and c1) represent the VIP total plot for the Polymer and Irradiation Time classes in the case of PE+PP, PE, and PP, respectively. Figures 3.5 (a2, b2, and c2) represent the VIP predictive plots for the same models. Figures 3.5 (a3, b3, and c3) represent VIP orthogonal plots.

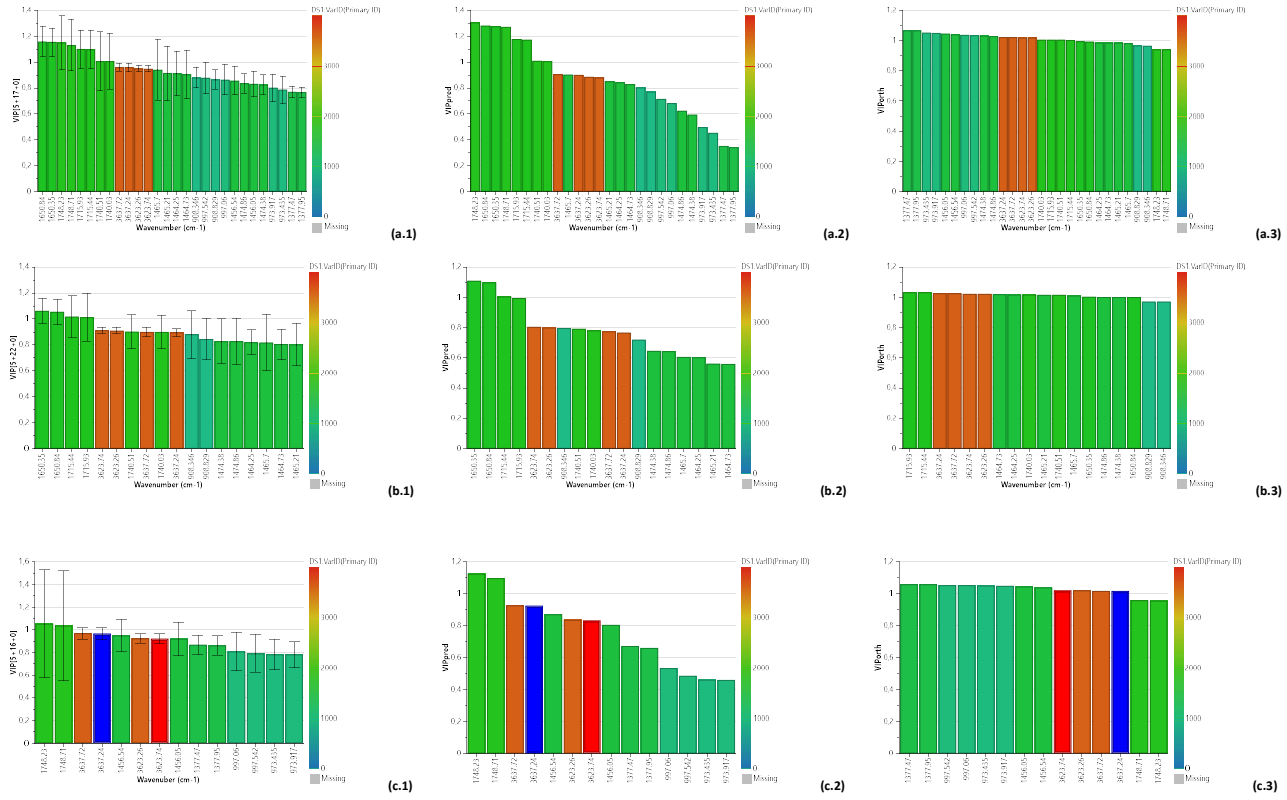

Figure 3.5. *Discrimination sequence for every model (row): VIP total plot (left column), VIP predictive plot (central column), and VIP orthogonal plot (right column). The compared models were (from top to bottom): PE+PP-Irradiation Time (3.5[a1-a2-a3]), PE-Irradiation Time (3.5[b1-b2-b2]), and PP-Irradiation Time (3.5[c1-c2-c3]). The most important bands (contribution values > 0.5) are sorted in descendent order and marked in blue for Y0, red for Y1 to Y5, and orange if the bars contribution values are larger than 3StdDev (StdDev = overall standard deviation).*

The next step was to quantitatively decide the discriminating power of wavenumber in the classification process. VIP plots required selecting the peaks used for index's calculation in their respective models (PE+PP, PE, and PP). Peaks with VIP > 1, were considered explanatory for the model. VIP total plot showed that the explanatory peaks were those at 1650 cm^{-1}, 1715 cm^{-1}, and 1740 cm^{-1} for PE, and 1748 cm^{-1} for PP. However other peaks, with VIP in the 0.5-1 range could be considered moderately significant. This was the case of 1377 cm^{-1} for PE+PP and 973 cm^{-1} for PP, both used in the PP indexes' calculation (MGI and Isotacticity). None of the reference peaks (1465 cm^{-1}, 1456 cm^{-1}, and 973 cm^{-1}) conveyed degradation information, which confirmed that their selection was correct.

Our results showed that the information provided by the degradation indexes based on certain peaks of the FTIR spectra cannot be directly correlated with the environmental photodegradation history, at least for different plastic particles. A maximum in the degradation indexes associated to the carbonyl bond stretching was produced as an intermediate degradation step, but further irradiation led to a non-uniform evolution of indexes based on that absorption band. Likewise, the hydroxyl bond-related indexes did not follow a clear pattern except when tracking the evolution of individual particles. So, our results showed that simple degradation indexes, although extensively used in the past to assess the extent of plastic photodegradation, cannot be generally accepted as an indication of the accumulated exposure of plastic debris to photochemical ageing. The use of specific IR bands to quantitatively assess the oxidation extent of polyolefins has already been criticized because the evolution of chemical bonds upon weathering do not change linearly with time (Brandon et al., 2016). The mere evolution of certain peaks cannot be related in a straightforward way with the environmental stress suffered by the plastic except when analysing the same fragment due to the huge variability observed for different plastics (even with the same polymer), weathering conditions, and bond type determined. However, the information about plastic ageing is still contained in the mid-infrared spectra and can be revealed using OPLS-DA models, which allowed discriminating among samples depending on the irradiation received in accelerated ageing experiments. The relationship

between photochemical ageing and individual FTIR bands was not simple, and several peaks were involved. Nevertheless, the samples with different exposure time were clearly discriminated from each other. The information for the discrimination was contained mostly in the absorption bands mainly corresponding to the hydroxyl and carbonyl bond stretching. The use of full spectral information combination offers the possibility of sorting plastic debris as a function of their irradiation history.

3.4 Conclusions

Infrared Spectrometry and Chemometric techniques were used to model the photodegradation of marine litter polymers. The selected materials were PE and PP microplastics recovered from a sandy beach as well as pure pellets and fragments of objects made of the same polymers, which were subject to accelerated ageing that delivered UV irradiation equivalent to up to five years or solar exposure.

Degradation indexes were calculated by tracking the absorbance peaks from carbonyl, hydroxyl, and double bonds, as well as peak ratios measuring crystallinity (PE) and tacticity (PP). The results showed that none of the degradation indicators yielded a clear trend as a function of UV exposure. Even without considering outliers, the evolution of IR absorption peaks was different for different specimens and did not follow a simple pattern.

OPLS-DA models were used to process all the information contained in ATR-FTIR spectra. The models allowed clustering both polymers in different classes according to the irradiation received in accelerated ageing experiments. VIP analyses showed that the information for the discrimination was mainly contained in the absorption peaks corresponding to the hydroxyl and carbonyl stretching absorptions, with lower contribution from the peaks associated to vinyl bonds (PE) and tacticity (PP). Although the models were derived from a large set of variables, the chemometric models presented good fitting and can be used for prediction.

3.5 Supplementary Materials

a) KCBI – (PE)

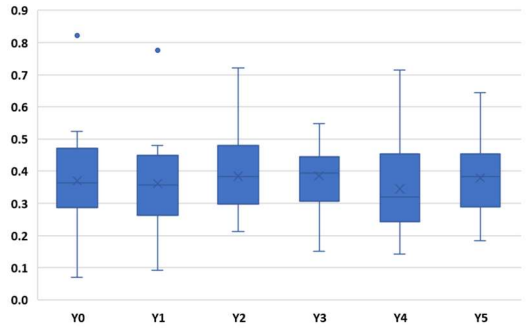

b) ECBI – (PE)

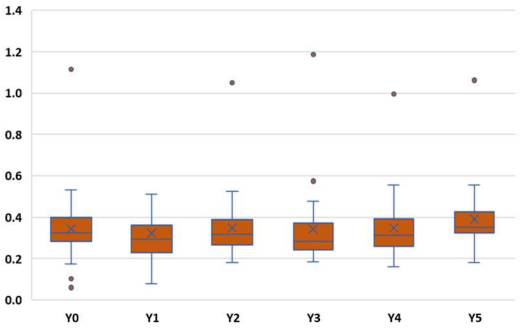

c) VBI – (PE)

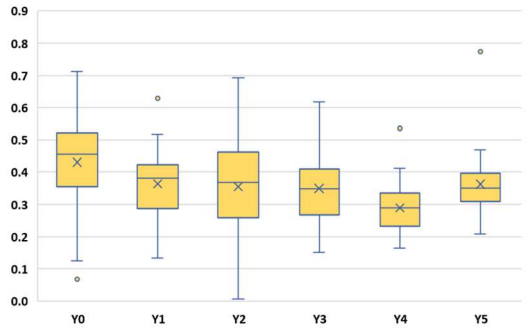

d) IDBI – (PE)

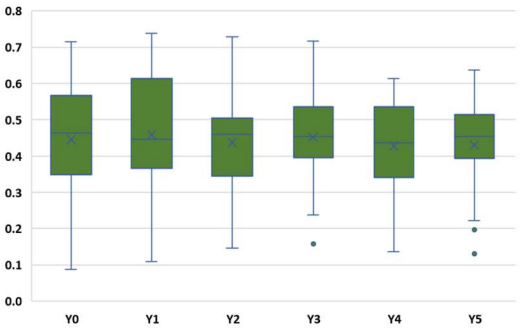

e) *X* (%) – Crystallinity (PE)

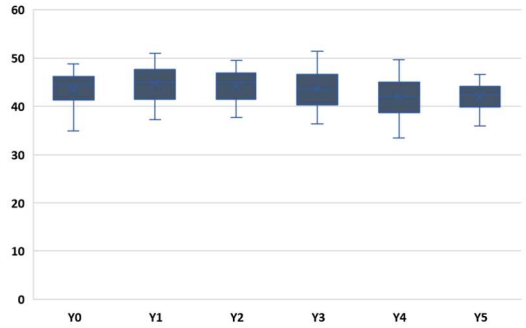

f) ECBI – (PP)

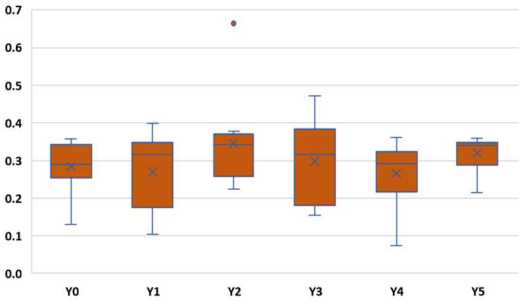

g) MGI – (PP)

h) *I* (%) – Isotacticity (PP)

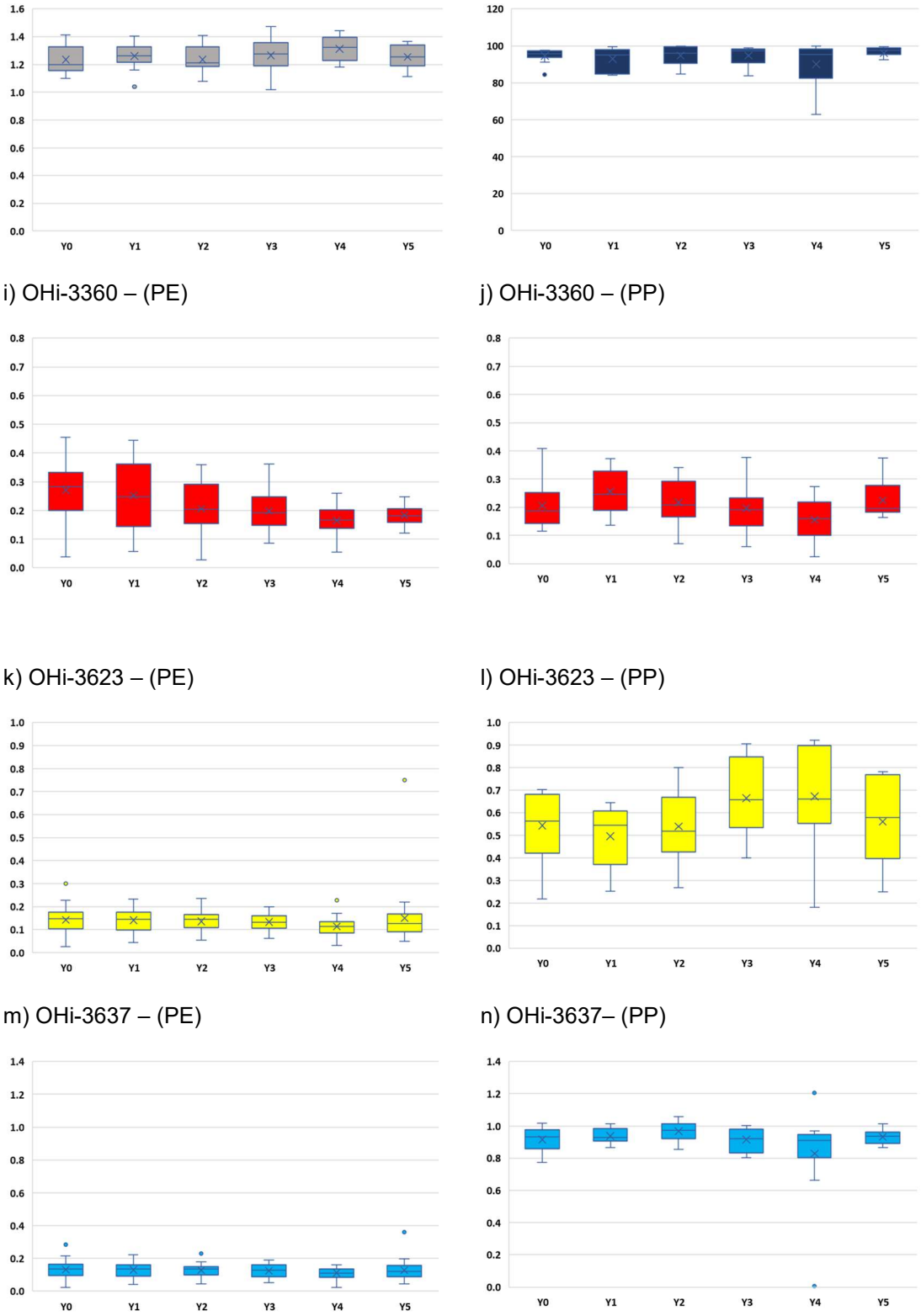

Figure S3.1. *Degradation indexes for PE samples as a function of the years of simulated solar exposure. a) KCBI – Keto Carbonyl Bond Index; b) ECBI – Ester Carbonyl Bond Index; c) VBI – Vinyl Bond Index; d) IDBI – Internal Double Bond Index; e) X(%) –*

Crystallinity; i) OHi-3360 – Hydroxyl Bond Index at 3360 cm^{-1}; k) OHi-3623 – Hydroxyl Bond Index at 3623 cm^{-1}; m) OHi-3637 – Hydroxyl Bond Index at 3637 cm^{-1}; and for PP samples: f) ECBI – Ester Carbonyl Index; g) MGI – Methyl Group Index; h) I(%) – Isotacticity; j) OHi-3360 – Hydroxyl Bond Index at 3360 cm^{-1}; l) OHi-3623 – Hydroxyl Bond Index at 3623 cm^{-1}; and n) OHi-3637 – Hydroxyl Bond Index at 3637 cm^{-1}. Y0 represents samples at the beginning of the runs, and YN after UVA+UVB irradiation equivalent to N years of solar exposure.

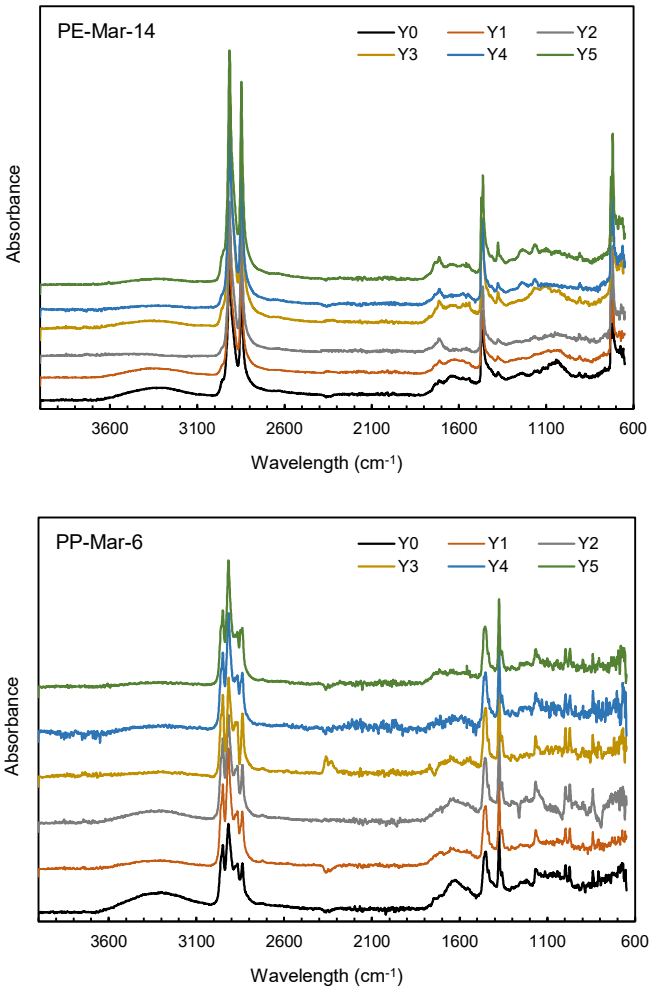

Figure S3.2. *Representative FTIR spectra of PE and PP fragments before (Y0) and after (Y1-Y5) irradiation.*

Table S3.1. *Fourier transform infrared analysis of PE samples photodegraded for 360 h equivalent to five years of exposure. (KCBI – Keto Carbonyl Bond Index; ECBI – Ester Carbonyl Bond Index; VBI – Vinyl Bond Index; IDBI – Internal Double Bond Index); Crystallinity, X (%); OHi – Hydroxyl Index at 3360, 3623, and 3637 cm-1. (Fr = fragment, Pe = pure pellet.)*

PE Samples	Year	KCBI		ECBI		VBI		IDBI		X(%)		OHi					
			sd±		sd±		sd±		sd±		sd±	3360	sd±	3623	sd±	3637	sd±
HDPE-Fr	Y0	0.2564	0.0100	0.2634	0.0496	0.3082	0.0672	0.2614	0.0251	42.38	1.21	0.1724	0.1462	0.1086	0.0404	0.0968	0.0372
HDPE-Fr	Y1	0.2419	0.0154	0.2165	0.0386	0.3354	0.0555	0.2663	0.0236	41.46	1.45	0.4247	0.0383	0.1434	0.0288	0.1345	0.0250
HDPE-Fr	Y2	0.2296	0.0159	0.2681	0.0498	0.2007	0.0764	0.2257	0.0276	41.47	1.45	0.1144	0.1434	0.0917	0.0420	0.0852	0.0380
HDPE-Fr	Y3	0.2336	0.0161	0.2711	0.0499	0.1868	0.0742	0.2375	0.0284	40.25	1.47	0.1037	0.1421	0.0804	0.0419	0.0787	0.0380
HDPE-Fr	Y4	0.2242	0.0153	0.3548	0.0236	0.1640	0.0686	0.2375	0.0284	38.51	0.83	0.0660	0.1354	0.0319	0.0289	0.0317	0.0262
HDPE-Fr	Y5	0.2151	0.0126	0.2725	0.0500	0.2084	0.0773	0.1965	0.0173	40.61	1.49	0.1208	0.1440	0.0691	0.0408	0.0657	0.0370
LDPE-Pe	Y0	0.0709	0.0476	0.0595	0.0645	0.0671	0.1004	0.1041	0.0666	34.87	1.57	0.0380	0.0426	0.0366	0.0179	0.0356	0.0184
LDPE-Pe	Y1	0.0920	0.0553	0.0791	0.0723	0.1329	0.1242	0.1086	0.0682	40.40	1.33	0.1168	0.0698	0.0428	0.0196	0.0399	0.0193
LDPE-Pe	Y2	0.2130	0.0496	0.2348	0.0744	0.3575	0.1189	0.2526	0.0711	37.77	2.09	0.1889	0.0664	0.0814	0.0163	0.0778	0.0144
LDPE-Pe	Y3	0.1510	0.0622	0.1871	0.0836	0.1927	0.1343	0.1577	0.0787	36.37	2.02	0.1166	0.0698	0.0626	0.0208	0.0510	0.0203
LDPE-Pe	Y4	0.1430	0.0623	0.1648	0.0848	0.3194	0.1284	0.2663	0.0666	38.30	2.05	0.2021	0.0632	0.0426	0.0196	0.0358	0.0184
LDPE-Pe	Y5	0.1956	0.0556	0.2364	0.0739	0.3440	0.1228	0.2218	0.0775	36.87	2.08	0.1906	0.0661	0.0751	0.0186	0.0696	0.0178
LDPE-Fr	Y0	0.0959	0.0343	0.1031	0.0586	0.1246	0.0365	0.0869	0.0156	35.20	1.65	0.0903	0.1452	0.0252	0.0287	0.0236	0.0232
LDPE-Fr	Y1	0.1663	0.0571	0.1663	0.0800	0.2743	0.0603	0.1524	0.0302	37.22	1.58	0.4252	0.1098	0.0933	0.0278	0.0769	0.0222
LDPE-Fr	Y2	0.2399	0.0476	0.2607	0.0798	0.2601	0.0632	0.1453	0.0310	37.73	1.43	0.1595	0.1573	0.0535	0.0338	0.0451	0.0269
LDPE-Fr	Y3	0.2282	0.0514	0.3038	0.0676	0.2779	0.0594	0.1697	0.0256	36.51	1.69	0.3616	0.1377	0.0960	0.0267	0.0776	0.0220
LDPE-Fr	Y4	0.1690	0.0573	0.2622	0.0795	0.1955	0.0640	0.1358	0.0314	33.49	1.00	0.1139	0.1505	0.0312	0.0305	0.0234	0.0231
LDPE-Fr	Y5	0.1836	0.0576	0.1811	0.0822	0.2184	0.0660	0.1298	0.0311	35.94	1.71	0.1263	0.1528	0.0487	0.0335	0.0464	0.0270
PE-Mar-1	Y0	0.2927	0.0449	0.3131	0.0791	0.4194	0.0403	0.4668	0.0560	46.20	1.64	0.2670	0.0332	0.1227	0.0183	0.1336	0.0220
PE-Mar-1	Y1	0.3287	0.0569	0.2340	0.0621	0.2640	0.0417	0.4376	0.0496	49.79	0.72	0.1089	0.0400	0.1474	0.0187	0.1338	0.0220
PE-Mar-1	Y2	0.3814	0.0601	0.3267	0.0794	0.3724	0.0564	0.4632	0.0555	47.02	1.70	0.1942	0.0565	0.1402	0.0196	0.1260	0.0221
PE-Mar-1	Y3	0.3662	0.0606	0.2751	0.0747	0.3271	0.0586	0.4648	0.0557	47.24	1.69	0.1678	0.0563	0.1106	0.0139	0.0924	0.0093
PE-Mar-1	Y4	0.4524	0.0388	0.4406	0.0473	0.3451	0.0590	0.5538	0.0459	46.19	1.64	0.1768	0.0568	0.1602	0.0147	0.1512	0.0186
PE-Mar-1	Y5	0.3819	0.0601	0.3556	0.0775	0.3145	0.0573	0.5572	0.0444	45.46	1.48	0.1814	0.0569	0.1357	0.0197	0.1378	0.0217
PE-Mar-2	Y0	0.3665	0.0306	0.3227	0.0663	0.5390	0.1175	0.5985	0.0654	44.66	1.56	0.3280	0.0831	0.1674	0.0295	0.1639	0.0258
PE-Mar-2	Y1	0.3757	0.0319	0.2885	0.0589	0.5136	0.1235	0.6409	0.0483	45.61	1.31	0.3575	0.0719	0.1725	0.0281	0.1573	0.0279
PE-Mar-2	Y2	0.3843	0.0323	0.3124	0.0648	0.3779	0.1283	0.5431	0.0720	45.12	1.47	0.2184	0.0939	0.1632	0.0305	0.1492	0.0296
PE-Mar-2	Y3	0.4299	0.0210	0.4549	0.0372	0.5503	0.1141	0.4757	0.0618	43.07	1.57	0.2487	0.0950	0.1213	0.0302	0.1040	0.0264
PE-Mar-2	Y4	0.4056	0.0303	0.3882	0.0650	0.3150	0.1153	0.4979	0.0676	42.40	1.42	0.1550	0.0815	0.1315	0.0318	0.1238	0.0304
PE-Mar-2	Y5	0.3489	0.0255	0.3384	0.0678	0.2887	0.1061	0.5039	0.0687	42.27	1.37	0.1571	0.0822	0.1013	0.0231	0.1002	0.0251
PE-Mar-3	Y0	0.2471	0.0326	0.1905	0.0585	0.2629	0.0525	0.2527	0.0668	39.73	1.71	0.1864	0.0190	0.0909	0.0112	0.0880	0.0065
PE-Mar-3	Y1	0.2528	0.0337	0.1934	0.0590	0.2472	0.0517	0.3154	0.0761	40.42	1.51	0.1591	0.0251	0.0900	0.0113	0.0795	0.0080
PE-Mar-3	Y2	0.2490	0.0330	0.1800	0.0566	0.2877	0.0508	0.2658	0.0702	38.47	1.83	0.1664	0.0245	0.0882	0.0115	0.0804	0.0080
PE-Mar-3	Y3	0.3147	0.0265	0.2426	0.0597	0.3167	0.0437	0.4105	0.0574	39.40	1.77	0.1514	0.0249	0.0941	0.0106	0.0776	0.0079
PE-Mar-3	Y4	0.2581	0.0345	0.1965	0.0594	0.1809	0.0265	0.2764	0.0724	36.20	1.30	0.1179	0.0136	0.0866	0.0115	0.0838	0.0076
PE-Mar-3	Y5	0.3103	0.0285	0.3229	0.0243	0.2864	0.0510	0.3947	0.0639	37.06	1.64	0.1572	0.0251	0.0655	0.0029	0.0668	0.0041
PE-Mar-4	Y0	0.3373	0.0325	0.3325	0.0356	0.4878	0.1894	0.4717	0.0508	44.44	1.73	0.3141	0.0162	0.1359	0.0224	0.1299	0.0167
PE-Mar-4	Y1	0.2879	0.0357	0.2416	0.0212	0.3493	0.1822	0.4229	0.0467	45.43	1.48	0.2203	0.0492	0.1169	0.0234	0.1037	0.0193
PE-Mar-4	Y2	0.3476	0.0288	0.3237	0.0374	0.4165	0.1895	0.4882	0.0489	44.39	1.74	0.2248	0.0493	0.1513	0.0175	0.1337	0.0153
PE-Mar-4	Y3	0.3114	0.0368	0.2813	0.0376	0.3766	0.1861	0.5346	0.0315	43.93	1.79	0.2216	0.0492	0.1259	0.0236	0.1031	0.0192
PE-Mar-4	Y4	0.2858	0.0354	0.3049	0.0393	0.3003	0.1717	0.4296	0.0482	41.91	1.55	0.2064	0.0478	0.1152	0.0233	0.1079	0.0196
PE-Mar-4	Y5	0.2613	0.0281	0.3282	0.0366	0.7734	0.0708	0.4190	0.0457	41.30	1.30	0.1858	0.0434	0.0889	0.0149	0.0875	0.0149
PE-Mar-5	Y0	0.3535	0.0378	0.5303	0.0257	0.4097	0.1090	0.3555	0.0138	41.44	1.63	0.2434	0.0598	0.0863	0.0204	0.0832	0.0161
PE-Mar-5	Y1	0.3396	0.0383	0.5114	0.0205	0.3794	0.1102	0.3843	0.0199	41.43	1.63	0.2323	0.0606	0.1035	0.0199	0.0945	0.0151
PE-Mar-5	Y2	0.3610	0.0368	0.5248	0.0248	0.4995	0.0886	0.3919	0.0192	41.52	1.61	0.2946	0.0467	0.1220	0.0133	0.1059	0.0110
PE-Mar-5	Y3	0.3852	0.0299	0.5745	0.0198	0.4610	0.1009	0.3860	0.0198	40.23	1.76	0.2484	0.0592	0.0913	0.0207	0.0713	0.0145
PE-Mar-5	Y4	0.3227	0.0370	0.5557	0.0255	0.2534	0.0858	0.3677	0.0184	38.77	1.58	0.1401	0.0400	0.0876	0.0205	0.0842	0.0161
PE-Mar-5	Y5	0.2859	0.0234	0.5564	0.0254	0.2759	0.0944	0.4058	0.0150	37.84	1.19	0.1828	0.0565	0.0668	0.0150	0.0670	0.0130
PE-Mar-6	Y0	0.1911	0.0408	0.2508	0.0845	0.4232	0.0794	0.3074	0.0365	43.29	1.53	0.2751	0.0431	0.0723	0.0199	0.0538	0.0136
PE-Mar-6	Y1	0.1767	0.0367	0.1843	0.0687	0.2107	0.1043	0.2509	0.0373	44.25	1.33	0.1022	0.0678	0.0507	0.0159	0.0590	0.0146
PE-Mar-6	Y2	0.2125	0.0436	0.2383	0.0830	0.3012	0.1107	0.2507	0.0372	44.06	1.39	0.1730	0.0751	0.0813	0.0194	0.0656	0.0149
PE-Mar-6	Y3	0.2242	0.0437	0.2748	0.0859	0.1503	0.0851	0.2740	0.0400	42.49	1.55	0.0853	0.0624	0.0636	0.0193	0.0544	0.0138
PE-Mar-6	Y4	0.2275	0.0436	0.3131	0.0838	0.2455	0.1095	0.3340	0.0253	40.55	0.97	0.1583	0.0753	0.0659	0.0196	0.0669	0.0149
PE-Mar-6	Y5	0.2894	0.0219	0.4090	0.0475	0.3555	0.1035	0.2479	0.0366	42.00	1.50	0.1799	0.0747	0.1027	0.0113	0.0898	0.0061
PE-Mar-7	Y0	0.2753	0.0520	0.3086	0.0646	0.4144	0.0837	0.4270	0.0134	45.34	1.93	0.2683	0.0407	0.1253	0.0261	0.1072	0.0165
PE-Mar-7	Y1	0.2815	0.0542	0.2400	0.0421	0.2904	0.0869	0.4889	0.0292	46.67	1.59	0.1350	0.0501	0.1193	0.0252	0.1193	0.0190

PE-Mar-7	Y2	0.4174	0.0465	0.4172	0.0471	0.4488	0.0722	0.5005	0.0269	45.68	1.87	0.2288	0.0549	0.1662	0.0207	0.1445	0.0164
PE-Mar-7	Y3	0.3504	0.0627	0.3658	0.0635	0.2442	0.0734	0.4748	0.0301	44.53	1.98	0.1438	0.0528	0.1234	0.0259	0.1179	0.0189
PE-Mar-7	Y4	0.3302	0.0627	0.3302	0.0660	0.2868	0.0862	0.4960	0.0280	41.87	1.33	0.1629	0.0567	0.1128	0.0237	0.1155	0.0185
PE-Mar-7	Y5	0.3851	0.0579	0.3353	0.0660	0.3858	0.0891	0.4694	0.0298	43.13	1.82	0.2066	0.0581	0.1651	0.0211	0.1501	0.0140
PE-Mar-8	Y0	0.5246	0.0728	0.4135	0.0238	0.5418	0.0899	0.5550	0.0630	45.86	2.13	0.2982	0.0990	0.1528	0.0365	0.1376	0.0285
PE-Mar-8	Y1	0.4607	0.0840	0.3322	0.0266	0.4812	0.1011	0.6239	0.0389	47.56	1.73	0.4284	0.0595	0.1946	0.0298	0.1798	0.0230
PE-Mar-8	Y2	0.4873	0.0814	0.3866	0.0324	0.5505	0.0871	0.5120	0.0637	45.51	2.16	0.3304	0.0960	0.1453	0.0361	0.1311	0.0275
PE-Mar-8	Y3	0.4902	0.0809	0.3796	0.0333	0.3983	0.0978	0.5429	0.0641	46.01	2.12	0.2150	0.0921	0.1428	0.0359	0.1455	0.0290
PE-Mar-8	Y4	0.3183	0.0463	0.3410	0.0297	0.3105	0.0662	0.4851	0.0595	41.84	1.14	0.1855	0.0838	0.1080	0.0255	0.1146	0.0227
PE-Mar-8	Y5	0.4005	0.0804	0.3673	0.0337	0.4343	0.1018	0.4617	0.0524	44.38	2.12	0.2410	0.0967	0.1914	0.0309	0.1768	0.0241
PE-Mar-9	Y0	0.2898	0.0710	0.1732	0.0643	0.2074	0.0933	0.3521	0.0498	47.15	2.12	0.0736	0.0723	0.0619	0.0651	0.0567	0.0489
PE-Mar-9	Y1	0.2619	0.0669	0.1499	0.0589	0.1504	0.0812	0.2795	0.0358	51.02	0.87	0.0653	0.0707	0.0725	0.0667	0.0722	0.0520
PE-Mar-9	Y2	0.3110	0.0717	0.2298	0.0664	0.2525	0.0948	0.3061	0.0457	45.99	1.97	0.1308	0.0760	0.0682	0.0661	0.0705	0.0518
PE-Mar-9	Y3	0.3961	0.0537	0.2346	0.0659	0.2577	0.0946	0.3811	0.0455	48.09	2.10	0.1490	0.0744	0.1146	0.0681	0.1237	0.0520
PE-Mar-9	Y4	0.2266	0.0558	0.1606	0.0618	0.1832	0.0897	0.3422	0.0500	46.07	1.99	0.0550	0.0681	0.0698	0.0663	0.0796	0.0530
PE-Mar-9	Y5	0.3693	0.0637	0.3086	0.0398	0.3928	0.0457	0.3986	0.0398	46.53	2.07	0.2340	0.0422	0.2202	0.0212	0.1845	0.0255
PE-Mar-10	Y0	0.4796	0.0173	0.3247	0.0540	0.4495	0.0553	0.6799	0.0273	46.57	2.01	0.2348	0.0692	0.1753	0.0140	0.1635	0.0136
PE-Mar-10	Y1	0.4418	0.0158	0.2975	0.0428	0.3082	0.0372	0.6110	0.0417	50.03	0.52	0.0574	0.0294	0.1376	0.0161	0.1398	0.0129
PE-Mar-10	Y2	0.4786	0.0176	0.4001	0.0603	0.4414	0.0574	0.5644	0.0283	45.86	1.98	0.2034	0.0740	0.1358	0.0155	0.1381	0.0123
PE-Mar-10	Y3	0.4439	0.0166	0.4354	0.0528	0.4400	0.0577	0.6227	0.0421	45.61	1.96	0.2391	0.0682	0.1683	0.0165	0.1689	0.0119
PE-Mar-10	Y4	0.4572	0.0193	0.3898	0.0611	0.3815	0.0612	0.6131	0.0419	45.67	1.96	0.1682	0.0744	0.1592	0.0181	0.1612	0.0141
PE-Mar-10	Y5	0.4759	0.0182	0.4212	0.0567	0.3712	0.0601	0.6369	0.0413	45.14	1.88	0.1953	0.0745	0.1460	0.0179	0.1461	0.0143
PE-Mar-11	Y0	0.3701	0.0584	0.2971	0.0690	0.3273	0.0672	0.3972	0.0441	48.57	2.15	0.2038	0.0269	0.1236	0.0131	0.1192	0.0169
PE-Mar-11	Y1	0.4463	0.0695	0.3701	0.0806	0.3808	0.0675	0.5124	0.0685	49.34	1.97	0.1893	0.0288	0.1377	0.0152	0.1172	0.0164
PE-Mar-11	Y2	0.3926	0.0648	0.3811	0.0805	0.3400	0.0685	0.4678	0.0676	47.22	2.26	0.2059	0.0264	0.1222	0.0126	0.1260	0.0181
PE-Mar-11	Y3	0.4218	0.0690	0.3022	0.0707	0.3049	0.0632	0.5398	0.0646	48.36	2.19	0.1346	0.0099	0.1389	0.0152	0.1278	0.0183
PE-Mar-11	Y4	0.4566	0.0690	0.3924	0.0799	0.3107	0.0645	0.4761	0.0685	46.83	2.24	0.1854	0.0289	0.1461	0.0145	0.1477	0.0166
PE-Mar-11	Y5	0.5477	0.0362	0.4944	0.0454	0.4686	0.0302	0.5736	0.0540	43.66	1.03	0.1863	0.0289	0.1581	0.0104	0.1582	0.0121
PE-Mar-12	Y0	0.3396	0.0387	0.3488	0.0511	0.5468	0.0626	0.4143	0.0582	45.87	1.70	0.3859	0.0566	0.1482	0.0146	0.1338	0.0151
PE-Mar-12	Y1	0.2631	0.0492	0.2595	0.0618	0.3552	0.1043	0.4382	0.0535	46.11	1.62	0.1844	0.1006	0.0922	0.0204	0.0799	0.0141
PE-Mar-12	Y2	0.2569	0.0484	0.2663	0.0624	0.4555	0.0999	0.3581	0.0572	44.78	1.87	0.2925	0.0972	0.1134	0.0237	0.1065	0.0208
PE-Mar-12	Y3	0.2425	0.0455	0.2040	0.0465	0.3735	0.1057	0.4342	0.0546	44.76	1.88	0.1923	0.1015	0.1293	0.0222	0.1216	0.0194
PE-Mar-12	Y4	0.2482	0.0468	0.2638	0.0622	0.2898	0.0906	0.2985	0.0327	42.45	1.58	0.1669	0.0978	0.0971	0.0217	0.1061	0.0208
PE-Mar-12	Y5	0.3375	0.0397	0.3471	0.0518	0.3221	0.0992	0.3953	0.0597	42.14	1.45	0.1457	0.0931	0.1053	0.0232	0.0990	0.0202
PE-Mar-13	Y0	0.4450	0.0601	0.3959	0.0614	0.5040	0.0748	0.4864	0.0911	45.86	1.05	0.3193	0.0844	0.1899	0.0241	0.1790	0.0172
PE-Mar-13	Y1	0.4368	0.0613	0.3933	0.0619	0.4483	0.0930	0.6989	0.0184	44.53	1.16	0.3757	0.0605	0.1743	0.0275	0.1539	0.0214
PE-Mar-13	Y2	0.4149	0.0627	0.3896	0.0626	0.3918	0.0992	0.4695	0.0881	46.46	0.80	0.2250	0.0930	0.1442	0.0262	0.1487	0.0210
PE-Mar-13	Y3	0.4364	0.0613	0.2853	0.0547	0.3461	0.0970	0.5149	0.0938	43.67	0.97	0.1685	0.0836	0.1841	0.0257	0.1726	0.0194
PE-Mar-13	Y4	0.2995	0.0116	0.2685	0.0472	0.2451	0.0632	0.5052	0.0932	44.27	1.12	0.1759	0.0856	0.1239	0.0183	0.1249	0.0130
PE-Mar-13	Y5	0.4403	0.0608	0.3818	0.0639	0.3738	0.0991	0.5069	0.0933	44.56	1.16	0.2074	0.0913	0.1621	0.0282	0.1561	0.0214
PE-Mar-14	Y0	0.3782	0.1278	0.3782	0.0880	0.4947	0.1213	0.3376	0.0508	43.00	2.68	0.3206	0.0411	0.1504	0.0349	0.1376	0.0229
PE-Mar-14	Y1	0.4735	0.1188	0.4206	0.0810	0.4090	0.1343	0.4449	0.0736	44.17	2.65	0.2322	0.0539	0.1815	0.0317	0.1619	0.0224
PE-Mar-14	Y2	0.4117	0.1271	0.3620	0.0889	0.4996	0.1200	0.4174	0.0731	46.94	1.85	0.2901	0.0514	0.1504	0.0349	0.1504	0.0236
PE-Mar-14	Y3	0.4513	0.1229	0.2708	0.0767	0.3850	0.1348	0.5318	0.0516	43.32	2.68	0.2592	0.0551	0.1990	0.0251	0.1827	0.0143
PE-Mar-14	Y4	0.1637	0.0372	0.2455	0.0666	0.1690	0.0619	0.4054	0.0720	39.46	1.60	0.2402	0.0547	0.1141	0.0270	0.1296	0.0212
PE-Mar-14	Y5	0.4438	0.1240	0.4430	0.0742	0.3682	0.1344	0.4756	0.0705	43.45	2.68	0.1782	0.0367	0.1320	0.0327	0.1285	0.0209
PE-Mar-15	Y0	0.3995	0.0172	0.3327	0.0215	0.4527	0.0780	0.5034	0.0172	41.01	1.09	0.2906	0.0577	0.1465	0.2761	0.1355	0.1043
PE-Mar-15	Y1	0.3990	0.0173	0.3274	0.0228	0.4133	0.0913	0.4788	0.0274	40.72	1.18	0.2831	0.0609	0.1568	0.2771	0.1498	0.1054
PE-Mar-15	Y2	0.3953	0.0177	0.2926	0.0218	0.2024	0.0672	0.4548	0.0291	39.92	1.30	0.1413	0.0665	0.1310	0.2744	0.1287	0.1036
PE-Mar-15	Y3	0.4000	0.0171	0.2944	0.0223	0.3506	0.0999	0.4335	0.0254	39.89	1.30	0.1952	0.0747	0.1360	0.2750	0.1309	0.1038
PE-Mar-15	Y4	0.3587	0.0040	0.2904	0.0212	0.2891	0.0965	0.4425	0.0277	38.70	1.18	0.1519	0.0692	0.1104	0.2718	0.1066	0.1003
PE-Mar-15	Y5	0.3905	0.0179	0.3353	0.0207	0.3199	0.0997	0.4474	0.0284	37.98	0.90	0.1604	0.0709	0.7499	0.0175	0.3597	0.0156
PE-Mar-16	Y0	0.5166	0.0348	0.4026	0.1227	0.5153	0.2245	0.6148	0.0943	48.78	3.55	0.3101	0.1443	0.1754	0.0470	0.1643	0.0400
PE-Mar-16	Y1	0.4404	0.0307	0.3583	0.1218	0.5026	0.2273	0.7392	0.0842	48.01	3.60	0.4445	0.0928	0.2253	0.0307	0.2031	0.0288
PE-Mar-16	Y2	0.5102	0.0363	0.3187	0.1168	0.0757	0.0755	0.7287	0.0872	49.58	3.43	0.0508	0.1172	0.1673	0.0477	0.1536	0.0407
PE-Mar-16	Y3	0.4400	0.0305	0.2317	0.0878	0.3793	0.2423	0.7168	0.0900	51.49	2.89	0.2070	0.1511	0.1559	0.0479	0.1643	0.0400
PE-Mar-16	Y4	0.4960	0.0385	0.5132	0.1023	0.3452	0.2429	0.5381	0.0733	44.05	3.07	0.1704	0.1483	0.1060	0.0385	0.1035	0.0315
PE-Mar-16	Y5	0.5027	0.0377	0.5082	0.1041	0.4087	0.2405	0.5794	0.0878	43.23	2.74	0.1734	0.1487	0.1184	0.0428	0.1149	0.0357
PE-Mar-17	Y0	0.5075	0.0331	0.3657	0.0688	0.4595	0.1792	0.5455	0.0177	47.24	2.06	0.2680	0.0954	0.1622	0.0259	0.1496	0.0234
PE-Mar-17	Y1	0.4589	0.0339	0.3392	0.0719	0.3953	0.1945	0.4976	0.0175	47.54	2.04	0.2811	0.0907	0.1753	0.0230	0.1652	0.0208
PE-Mar-17	Y2	0.4951	0.0353	0.2791	0.0679	0.0517	0.0963	0.5031	0.0194	48.48	1.91	0.0281	0.0833	0.1642	0.0256	0.1572	0.0226
PE-Mar-17	Y3	0.4859	0.0360	0.2474	0.0586	0.2572	0.2045	0.5285	0.0217	49.20	1.70	0.1379	0.1106	0.1586	0.0263	0.1590	0.0222
PE-Mar-17	Y4	0.4283	0.0213	0.2936	0.0703	0.2324	0.2033	0.5404	0.0194	46.01	1.97	0.0876	0.1035	0.1124	0.0166	0.1100	0.0134
PE-Mar-17	Y5	0.5128	0.0317	0.4248	0.0474	0.3774	0.1975	0.5155	0.0217	44.06	1.22	0.1757	0.1112	0.1306	0.0243	0.1306	0.0221
PE-Mar-18	Y0	0.4106	0.0387	0.2887	0.0640	0.4947	0.1493	0.4436	0.0150	46.32	2.03	0.3468	0.0532	0.1717	0.0353	0.1596	0.0303
PE-Mar-18	Y1	0.3943	0.0415	0.2904	0.0636	0.3972	0.1772	0.4149	0.0180	46.85	2.00	0.2632	0.0902	0.1485	0.0389	0.1388	0.0334
PE-Mar-18	Y2	0.3710	0.0419	0.1998	0.0610	0.0073	0.1041	0.4145	0.0180	47.11	1.97	0.1353	0.0901	0.1645	0.0369	0.1457	0.0329
PE-Mar-18	Y3	0.3913	0.0417	0.1821	0.0555	0.2702	0.1863	0.3997	0.0134	48.51	1.57	0.1549	0.0936	0.1642	0.0370	0.1623	0.0296
PE-Mar-18	Y4	0.3084	0.0153	0.2153	0.0642	0.2327	0.1840	0.4289	0.0184	44.68	1.87	0.1375	0.0906	0.0854	0.0247	0.0874	0.0221
PE-Mar-18	Y5	0.4054	0.0399	0.3312	0.0509	0.3392	0.1847	0.4388	0.0166	43.44	1.39	0.1584	0.0941	0.1103	0.0354	0.1072	0.0303
PE-Mar-19	Y0	0.3617	0.0116	0.2936	0.0186	0.5923	0.0604	0.5993	0.0257	44.55	0.51	0.4551	0.0370	0.2182	0.0104	0.1963	0.0096
PE-Mar-19	Y1	0.3276	0.0231	0.3224	0.0239	0.4066	0.1033	0.4465	0.0909	42.86	1.08	0.2784	0.0960	0.1625	0.0253	0.1516	0.0199
PE-Mar-19	Y2	0.3181	0.0228	0.3104	0.0232	0.4824	0.1015	0.4218	0.0904	43.13	1.07	0.2992	0.0963	0.1704	0.0260	0.1643	0.0207
PE-Mar-19	Y3	0.3124	0.0221	0.3218	0.0239	0.4442	0.1045	0.3980	0.0880	41.93	0.97	0.2821	0.0961	0.1492	0.0221	0.1414	0.0172

PE-Mar-19	Y4	0.3293	0.0230	0.3587	0.0122	0.3560	0.0949	0.3861	0.0860	42.28	1.04	0.2263	0.0892	0.1711	0.0260	0.1590	0.0207
PE-Mar-19	Y5	0.3012	0.0191	0.3199	0.0239	0.3366	0.0892	0.3883	0.0864	42.12	1.01	0.2154	0.0865	0.1756	0.0261	0.1635	0.0208
PE-Mar-20	Y0	0.4694	0.0173	0.4096	0.0235	0.5568	0.0643	0.6076	0.0527	44.62	0.81	0.3597	0.0502	0.2262	0.0174	0.2141	0.0187
PE-Mar-20	Y1	0.4801	0.0169	0.4394	0.0273	0.5166	0.0721	0.6753	0.0304	44.15	0.95	0.3478	0.0529	0.2325	0.0165	0.2246	0.0177
PE-Mar-20	Y2	0.4932	0.0131	0.4421	0.0272	0.5337	0.0697	0.6123	0.0523	44.00	0.97	0.3584	0.0505	0.2355	0.0158	0.2302	0.0164
PE-Mar-20	Y3	0.4776	0.0172	0.4767	0.0155	0.5293	0.0704	0.5771	0.0521	42.51	0.82	0.3183	0.0557	0.1965	0.0117	0.1885	0.0129
PE-Mar-20	Y4	0.4669	0.0171	0.4115	0.0241	0.4108	0.0579	0.5621	0.0498	43.61	1.00	0.2608	0.0470	0.2281	0.0172	0.2253	0.0176
PE-Mar-20	Y5	0.4469	0.0104	0.4331	0.0274	0.4087	0.0570	0.5404	0.0436	42.45	0.80	0.2478	0.0416	0.2057	0.0157	0.1980	0.0167
PE-Mar-21	Y0	0.5158	0.0480	0.4380	0.0332	0.5110	0.0272	0.5395	0.0527	38.83	1.61	0.3845	0.0287	0.2991	0.0498	0.2844	0.0447
PE-Mar-21	Y1	0.4667	0.0326	0.3070	0.0431	0.2944	0.0736	0.3988	0.0488	49.04	4.31	0.1478	0.0889	0.0992	0.0670	0.0949	0.0587
PE-Mar-21	Y2	0.5904	0.0378	0.3681	0.0528	0.3636	0.0836	0.4838	0.0636	48.99	4.32	0.1591	0.0913	0.1702	0.0808	0.1805	0.0739
PE-Mar-21	Y3	0.5471	0.0484	0.3704	0.0527	0.3567	0.0834	0.4236	0.0575	46.46	4.52	0.1891	0.0953	0.1231	0.0743	0.1326	0.0698
PE-Mar-21	Y4	0.5662	0.0456	0.3169	0.0464	0.3325	0.0815	0.5339	0.0547	49.72	4.18	0.2010	0.0961	0.2272	0.0772	0.2118	0.0714
PE-Mar-21	Y5	0.5151	0.0479	0.3771	0.0523	0.3417	0.0825	0.4637	0.0635	46.28	4.52	0.2163	0.0965	0.1754	0.0810	0.1575	0.0731
PE-Mar-22	Y0	0.8221	0.0572	1.1134	0.0733	0.7117	0.0933	0.7139	0.0866	38.92	0.37	0.3955	0.0709	0.1908	0.0331	0.1728	0.0309
PE-Mar-22	Y1	0.7758	0.0693	1.1246	0.0719	0.6289	0.1089	0.6892	0.0916	37.79	0.66	0.3729	0.0779	0.2028	0.0289	0.1880	0.0257
PE-Mar-22	Y2	0.7205	0.0705	1.0503	0.0715	0.6926	0.0990	0.7094	0.0877	38.02	0.66	0.3444	0.0834	0.1633	0.0370	0.1514	0.0337
PE-Mar-22	Y3	0.7858	0.0677	1.1864	0.0520	0.6184	0.1094	0.6654	0.0944	37.51	0.62	0.2896	0.0853	0.1597	0.0370	0.1476	0.0338
PE-Mar-22	Y4	0.7134	0.0696	0.9959	0.0545	0.5357	0.1025	0.5552	0.0828	38.06	0.66	0.2347	0.0762	0.1260	0.0318	0.1173	0.0293
PE-Mar-22	Y5	0.6433	0.0459	1.0620	0.0731	0.4518	0.0695	0.5143	0.0652	37.19	0.53	0.2052	0.0652	0.1207	0.0299	0.1106	0.0269
PE-Mar-23	Y0	0.3121	0.0250	0.2897	0.0259	0.3635	0.0530	0.4587	0.0701	41.80	1.34	0.1868	0.0678	0.1246	0.0344	0.1286	0.0316
PE-Mar-23	Y1	0.3234	0.0229	0.2899	0.0258	0.3827	0.0471	0.4959	0.0606	42.44	1.30	0.2991	0.0318	0.1754	0.0284	0.1635	0.0274
PE-Mar-23	Y2	0.3219	0.0233	0.2868	0.0266	0.3563	0.0545	0.4288	0.0729	42.77	1.24	0.2085	0.0670	0.1569	0.0335	0.1543	0.0298
PE-Mar-23	Y3	0.2934	0.0251	0.2275	0.0185	0.2915	0.0551	0.4421	0.0721	43.22	1.11	0.1720	0.0671	0.1596	0.0330	0.1545	0.0297
PE-Mar-23	Y4	0.3027	0.0256	0.2526	0.0275	0.2806	0.0529	0.3990	0.0719	40.32	1.05	0.1378	0.0616	0.1169	0.0333	0.1138	0.0297
PE-Mar-23	Y5	0.2622	0.0128	0.2580	0.0282	0.2584	0.0458	0.3058	0.0359	40.50	1.13	0.1344	0.0607	0.0922	0.0248	0.0905	0.0208

Table S3.2. *Fourier transform infrared analysis of PP samples photodegraded for 360 h equivalent to five years of exposure. ECI – Ester Carbonyl Index; MGI – Methyl Group Index; Isotacticity, I (%), OHi – Hydroxyl Index at 3360, 3623, and 3637 cm^{-1}. (Fr = fragment, Pe = pure pellet.)*

PP Samples	Year	ECI		MGI		*I* (%)		OHi					
			sd±		sd±		sd±	3360	sd±	3623	sd±	3637	sd±
PP-Pe	Y0	0.1304	0.3090	1.3904	0.1205	94.62	3.08	0.1152	0.1184	0.5877	0.2294	0.9135	0.1599
PP-Pe	Y1	1.0000	0.1257	1.0390	0.1492	93.10	3.30	0.3727	0.1186	0.3277	0.1908	1.0150	0.1462
PP-Pe	Y2	0.2867	0.3386	1.1957	0.1672	90.70	3.53	0.1879	0.1344	0.4440	0.2206	1.0565	0.1337
PP-Pe	Y3	0.4723	0.3439	1.0178	0.1427	92.06	3.41	0.3761	0.1175	0.6749	0.2214	0.8045	0.1524
PP-Pe	Y4	0.2447	0.3331	1.3110	0.1508	62.86	1.44	0.1079	0.1159	0.8993	0.1367	0.6643	0.0984
PP-Pe	Y5	0.3408	0.3433	1.1138	0.1638	92.35	3.39	0.3056	0.1337	0.4379	0.2196	0.9174	0.1598
PP-Fr-1	Y0	0.2551	0.0678	1.3067	0.0793	84.42	5.66	0.1359	0.0891	0.2182	0.0795	0.7775	0.0607
PP-Fr-1	Y1	0.1036	0.0700	1.2942	0.0795	84.20	5.66	0.1577	0.0880	0.2508	0.0827	0.9841	0.0345
PP-Fr-1	Y2	0.2250	0.0759	1.1761	0.0442	91.96	3.67	0.2478	0.0624	0.2687	0.0828	0.8541	0.0758
PP-Fr-1	Y3	0.1852	0.0803	1.3082	0.0792	83.76	5.66	0.0602	0.0801	0.3986	0.0347	0.8345	0.0745
PP-Fr-1	Y4	0.0736	0.0577	1.3991	0.0563	75.97	3.50	0.0244	0.0671	0.1807	0.0703	0.8491	0.0756
PP-Fr-1	Y5	0.2139	0.0777	1.2958	0.0795	84.23	5.66	0.1633	0.0874	0.2493	0.0827	0.8651	0.0758
PP-Fr-2	Y0	0.2543	0.0837	1.1877	0.0329	91.20	5.07	0.1895	0.1149	0.5401	0.1629	0.9271	0.0387
PP-Fr-2	Y1	0.1248	0.0621	1.2354	0.0341	84.38	4.93	0.1357	0.1132	0.3868	0.1604	0.9839	0.0166
PP-Fr-2	Y2	0.2427	0.0844	1.2014	0.0353	84.60	4.98	0.1362	0.1133	0.4375	0.1660	0.9007	0.0374
PP-Fr-2	Y3	0.1551	0.0741	1.2565	0.0276	87.42	5.33	0.1166	0.1108	0.7183	0.0986	0.8973	0.0369
PP-Fr-2	Y4	0.3246	0.0670	1.2324	0.0346	84.85	5.03	0.0940	0.1064	0.4725	0.1671	0.8881	0.0348
PP-Fr-2	Y5	0.2783	0.0805	1.1724	0.0278	96.31	2.91	0.3746	0.0353	0.2774	0.1286	0.9214	0.0389
PP-Mar-1	Y0	0.3429	0.0654	1.1278	0.0396	95.15	2.52	0.4081	0.0392	0.4205	0.1412	0.8867	0.1301
PP-Mar-1	Y1	0.2949	0.0750	1.2358	0.0666	96.82	2.44	0.2259	0.0900	0.5762	0.1702	0.8654	0.1244
PP-Mar-1	Y2	0.2624	0.0759	1.2242	0.0668	95.40	2.52	0.2870	0.0901	0.4641	0.1547	1.0452	0.1384
PP-Mar-1	Y3	0.1704	0.0518	1.2948	0.0551	98.19	2.09	0.1857	0.0829	0.8358	0.1083	0.9225	0.1369
PP-Mar-1	Y4	0.2216	0.0709	1.2760	0.0609	91.55	1.22	0.2350	0.0908	0.5790	0.1703	1.2046	0.0789
PP-Mar-1	Y5	0.3401	0.0663	1.1969	0.0649	96.43	2.48	0.1993	0.0860	0.6960	0.1614	1.0134	0.1412
PP-Mar-2	Y0	0.2599	0.1948	1.1005	0.0939	96.57	5.83	0.1436	0.0586	0.4193	0.1367	0.7742	0.0435
PP-Mar-2	Y1	0.1930	0.1851	1.2614	0.1063	84.67	3.60	0.2002	0.0513	0.5237	0.1529	0.9068	0.0676
PP-Mar-2	Y2	0.6638	0.0541	1.0786	0.0853	89.98	5.73	0.0699	0.0399	0.8001	0.0647	0.9513	0.0556

PP-Mar-2	Y3	0.2560	0.1944	1.2127	0.1104	99.03	5.27	0.1859	0.0549	0.4854	0.1497	0.8299	0.0656
PP-Mar-2	Y4	0.2032	0.1871	1.3321	0.0865	93.63	6.06	0.1037	0.0533	0.5889	0.1516	0.8894	0.0694
PP-Mar-2	Y5	0.3286	0.1972	1.2552	0.1072	97.55	5.65	0.1870	0.0547	0.4596	0.1459	0.8926	0.0692
PP-Mar-3	Y0	0.3580	0.0436	1.1848	0.0218	97.18	0.89	0.2541	0.0496	0.6755	0.1569	0.9650	0.4309
PP-Mar-3	Y1	0.3979	0.0304	1.2672	0.0236	97.71	0.84	0.3223	0.0196	0.5635	0.1358	0.9213	0.4351
PP-Mar-3	Y2	0.3433	0.0449	1.2283	0.0320	96.86	0.87	0.2080	0.0478	0.7743	0.1543	1.0026	0.4263
PP-Mar-3	Y3	0.3396	0.0450	1.2227	0.0319	95.76	0.44	0.2206	0.0496	0.5552	0.1330	0.9943	0.4274
PP-Mar-3	Y4	0.2952	0.0386	1.2137	0.0311	97.99	0.77	0.2129	0.0486	0.9213	0.1085	0.0069	0.0328
PP-Mar-3	Y5	0.2906	0.0370	1.2497	0.0297	97.50	0.87	0.2066	0.0475	0.7780	0.1538	0.9526	0.4323
PP-Mar-4	Y0	0.3409	0.0160	1.1654	0.0331	97.66	2.03	0.2520	0.0393	0.7025	0.1238	0.9872	0.0267
PP-Mar-4	Y1	0.3447	0.0170	1.1605	0.0328	94.14	0.94	0.3434	0.0346	0.6045	0.1139	0.9317	0.0212
PP-Mar-4	Y2	0.3678	0.0176	1.1895	0.0316	99.45	1.72	0.3411	0.0356	0.5706	0.1040	0.9642	0.0288
PP-Mar-4	Y3	0.3838	0.0116	1.1209	0.0191	97.16	2.03	0.2697	0.0432	0.6421	0.1206	1.0026	0.0214
PP-Mar-4	Y4	0.3617	0.0183	1.1792	0.0329	98.68	1.92	0.2733	0.0437	0.8607	0.0835	0.9708	0.0288
PP-Mar-4	Y5	0.3472	0.0175	1.2079	0.0262	97.55	2.04	0.2688	0.0431	0.7812	0.1142	0.9476	0.0267
PP-Mar-5	Y0	0.3150	0.0257	1.2077	0.0190	97.30	1.16	0.2138	0.0335	0.6994	0.1258	0.9747	0.0224
PP-Mar-5	Y1	0.3450	0.0317	1.3057	0.0605	99.63	1.20	0.2659	0.0155	0.6453	0.1147	0.9363	0.0200
PP-Mar-5	Y2	0.3777	0.0276	1.3264	0.0601	99.99	1.08	0.2078	0.0334	0.6343	0.1114	0.9851	0.0194
PP-Mar-5	Y3	0.3865	0.0242	1.3434	0.0582	98.60	1.34	0.2135	0.0335	0.8864	0.1074	0.9770	0.0219
PP-Mar-5	Y4	0.3241	0.0287	1.3369	0.0591	97.01	1.05	0.1794	0.0285	0.8961	0.1036	0.9398	0.0211
PP-Mar-5	Y5	0.3456	0.0317	1.3560	0.0557	98.71	1.34	0.1896	0.0312	0.7659	0.1292	0.9472	0.0227
PP-Mar-6	Y0	0.2881	0.0206	1.2722	0.0408	96.13	0.94	0.1863	0.0707	0.6362	0.1600	0.9405	0.0435
PP-Mar-6	Y1	0.3587	0.0256	1.3941	0.0736	97.97	1.31	0.3174	0.0169	0.4663	0.1205	0.9021	0.0392
PP-Mar-6	Y2	0.3421	0.0295	1.4088	0.0726	98.05	1.31	0.1755	0.0702	0.6070	0.1579	0.9866	0.0340
PP-Mar-6	Y3	0.3154	0.0295	1.4741	0.0551	97.09	1.25	0.1411	0.0651	0.9052	0.0877	0.9694	0.0398
PP-Mar-6	Y4	0.3156	0.0295	1.3927	0.0736	98.02	1.31	0.1621	0.0689	0.7016	0.1588	0.9391	0.0435
PP-Mar-6	Y5	0.3535	0.0272	1.3648	0.0730	99.67	0.84	0.1687	0.0697	0.6425	0.1602	0.8837	0.0324
PP-Mar-7	Y0	0.2933	0.0271	1.4116	0.0491	95.13	1.76	0.1622	0.0588	0.5352	0.0922	1.0182	0.0274
PP-Mar-7	Y1	0.3381	0.0307	1.4025	0.0502	96.00	2.08	0.2200	0.0632	0.6134	0.0826	0.9265	0.0430
PP-Mar-7	Y2	0.3443	0.0296	1.3260	0.0389	99.78	2.08	0.3126	0.0260	0.3936	0.0471	0.9294	0.0435
PP-Mar-7	Y3	0.3158	0.0315	1.3970	0.0507	97.19	2.29	0.1970	0.0634	0.5510	0.0920	0.9188	0.0413
PP-Mar-7	Y4	0.2897	0.0258	1.4438	0.0401	99.82	2.07	0.1570	0.0576	0.6206	0.0805	0.9348	0.0442
PP-Mar-7	Y5	0.3591	0.0250	1.3369	0.0432	99.51	2.15	0.1903	0.0630	0.5164	0.0914	0.9873	0.0410

Table S3.3. *Outliers for the box plots of Fig. S3.1.*
(Nomenclature as in Tables S3.1 and S3.2.)

	Indexes		Year	Sample	Value
PE	KCBI		Y0	PE-Mar-22	0.8821
			Y1	PE-Mar-22	0.7758
	ECBI (PE)		Y0	PE-Mar-22	1.1134
			Y0	LDPE-Fr	0.1031
			Y0	LDPE-Pe	0.0595
			Y2	PE-Mar-22	1.0503
			Y3	PE-Mar-22	1.1864
			Y3	PE-Mar-5	0.5745
			Y4	PE-Mar-22	0.9959
			Y5	PE-Mar-22	1.0620
	VBI		Y0	LDPE-Pe	0.0671
			Y1	PE-Mar-22	0.6289
			Y4	PE-Mar-22	0.5357
			Y5	PE-Mar-4	0.7734
	IDBI		Y3	LDPE-Pe	0.1577
			Y5	HDPE-Fr	0.1965
			Y5	HDPE-Fr	0.1298
	OHi	3360	-	-	-
		3623	Y0	PE-Mar-21	0.2991
			Y4	PE-Mar-21	0.2272
			Y5	PE-Mar-15	0.7499
		3637	Y0	PE-Mar-21	0.2844
			Y2	PE-Mar-20	0.2302
			Y5	PE-Mar-15	0.3597
PP	ECBI (PP)		Y2	PP-Mar-2	0.6638
	MGI		Y1	PP-Pe	1.0390
	Isotacticity (%)		Y0	PP-Fr-1	84.4200
	OHi	3360	-	-	-
		3623	-	-	-
		3637	Y4	PP-Mar-3	0.0069
			Y4	PP-Mar-1	1.2046

3.6 References

PlasticsEurope. Plastics – the Facts 2021: An analysis of European plastics production, demand and waste data; PlasticsEurope: Association of Plastics Manufacturers: Brussels, 2021.

Lau, W.W.Y.; Shiran, Y.; Bailey, R.M.; Cook, E.; Stuchtey, M.R.; Koskella, J.; Velis, C.A.; Godfrey, L.; Boucher, J.; Murphy, M.B.; et al. Evaluating scenarios toward zero plastic pollution. Science 2020, 369, 1455-1461, doi:10.1126/science.aba9475.

Pinto-da-Costa, J.; Rocha-Santos, T.; Duarte, A.C. The environmental impacts of plastics and micro-plastics use, waste and pollution: EU and national measures; European Union. Policy Department for Citizens' Rights and Constitutional Affairs: Brussels, 2020; pp. 1-72.

Napper, I.E.; Thompson, R.C. Release of synthetic microplastic plastic fibres from domestic washing machines: Effects of fabric type and washing conditions. Mar. Pollut. Bull. 2016, 112, 39-45, doi:10.1016/j.marpolbul.2016.09.025.

OECD. Global Plastics Outlook: Economic Drivers, Environmental Impacts and Policy Options, OECD Publishing, Paris, 2022, doi:10.1787/de747aef-en.

North, E.J.; Halden, R.U. Plastics and environmental health: the road ahead. Reviews on Environmental Health 2013, 28, 1-8, doi:10.1515/reveh-2012-0030.

Carpenter, E.J.; Smith, K.L. Plastics on the Sargasso Sea surface. Science 1972, 175, 1240-1241, doi:10.1126/science.175.4027.1240.

Chamas, A.; Moon, H.; Zheng, J.; Qiu, Y.; Tabassum, T.; Jang, J.H.; Abu-Omar, M.; Scott, S.L.; Suh, S. Degradation rates of plastics in the environment. ACS Sustainable Chem. Eng. 2020, 8, 3494-3511, doi:10.1021/acssuschemeng.9b06635.

Gewert, B.; Plassmann, M.M.; MacLeod, M. Pathways for degradation of plastic polymers floating in the marine environment. Environ. Sci. Processes Impacts 2015, 17, 1513-1521, doi:10.1039/C5EM00207A.

Gopanna, A.; Mandapati, R.N.; Thomas, S.P.; Rajan, K.; Chavali, M. Fourier transform infrared spectroscopy (FTIR), Raman spectroscopy and wide-angle X-ray scattering (WAXS) of polypropylene (PP)/cyclic olefin copolymer (COC) blends for qualitative

and quantitative analysis. Polym. Bull. 2019, 76, 4259-4274, doi:10.1007/s00289-018-2599-0.

Brandon, J.; Goldstein, M.; Ohman, M.D. Long-term aging and degradation of microplastic particles: Comparing in situ oceanic and experimental weathering patterns. Mar. Pollut. Bull. 2016, 110, 299-308, doi: 10.1016/j.marpolbul.2016.06.048.

Edo, C.; Tamayo-Belda, M.; Martínez-Campos, S.; Martín-Betancor, K.; González-Pleiter, M.; Pulido-Reyes, G.; García-Ruiz, C.; Zapata, F.; Leganés, F.; Fernández-Piñas, F.; et al. Occurrence and identification of microplastics along a beach in the Biosphere Reserve of Lanzarote. Mar. Pollut. Bull. 2019, 143, 220-227, doi:10.1016/j.marpolbul.2019.04.061.

ASTM. Standard Practice for Preparation of Substitute Ocean Water, ASTM D1141-98(2021). 2021, doi:10.1520/D1141-98R21.

Rånby, B. Photodegradation and photo-oxidation of synthetic polymers. J. Anal. Appl. Pyrolysis 1989, 15, 237-247, doi:10.1016/0165-2370(89)85037-5.

Jabarin, S.A.; Lofgren, E.A. Photooxidative effects on properties and structure of high-density polyethylene. J. Appl. Polym. Sci. 1994, 53, 411-423, doi:10.1002/app.1994.070530404.

Singh, B.; Sharma, N. Mechanistic implications of plastic degradation. Polym. Degrad. Stab. 2008, 93, 561-584, doi:10.1016/j.polymdegradstab.2007.11.008.

Agboola, O.; Sadiku, R.; Mokrani, T.; Amer, I.; Imoru, O. Polyolefins and the environment. In Polyolefin Fibres (Second Edition), Ugbolue, S.C.O., Ed.; Woodhead Publishing: 2017; pp. 89-133.

Albertsson, A.-C.; Andersson, S.O.; Karlsson, S. The mechanism of biodegradation of polyethylene. Polym. Degrad. Stab. 1987, 18, 73-87, doi:10.1016/0141-3910(87)90084-X.

Zerbi, G.; Gallino, G.; Del Fanti, N.; Baini, L. Structural depth profiling in polyethylene films by multiple internal reflection infra-red spectroscopy. Polymer 1989, 30, 2324-2327, doi:10.1016/0032-3861(89)90269-3.

Arkatkar, A.; Arutchelvi, J.; Bhaduri, S.; Uppara, P.V.; Doble, M. Degradation of unpretreated and thermally pretreated polypropylene by soil consortia. Int. Biodeterior. Biodegrad. 2009, 63, 106-111, doi:10.1016/j.ibiod.2008.06.005.

Adothu, B.; Costa, F.R.; Mallick, S. Damp heat resilient thermoplastic polyolefin encapsulant for photovoltaic module encapsulation. Sol. Energy Mater. 2021, 224, 111024, doi:10.1016/j.solmat.2021.111024.

Chung, I.-M.; Kim, J.-K.; Han, J.-G.; Kong, W.-S.; Kim, S.-Y.; Yang, Y.-J.; An, Y.-J.; Kwon, C.; Chi, H.-Y.; Yhung Jung, M.; et al. Potential geo-discriminative tools to trace the origins of the dried slices of shiitake (Lentinula edodes) using stable isotope ratios and OPLS-DA. Food Chem. 2019, 295, 505-513, doi:10.1016/j.foodchem.2019.05.143.

Worley, B.; Powers, R. PCA as a practical indicator of OPLS-DA model reliability. Current Metabolomics 2016, 4, 97-103, doi:10.2174/2213235x04666160613122429.

Bylesjö, M.; Rantalainen, M.; Cloarec, O.; Nicholson, J.K.; Holmes, E.; Trygg, J. OPLS discriminant analysis: combining the strengths of PLS-DA and SIMCA classification. J. Chemometrics 2006, 20, 341-351, doi:10.1002/cem.1006.

Hiejima, Y.; Kida, T.; Takeda, K.; Igarashi, T.; Nitta, K.-h. Microscopic structural changes during photodegradation of low-density polyethylene detected by Raman spectroscopy. Polym. Degrad. Stab. 2018, 150, 67-72, doi:10.1016/j.polymdegradstab.2018.02.010.

Carrasco, F.; Pagès, P.; Pascual, S.; Colom, X. Artificial aging of high-density polyethylene by ultraviolet irradiation. Eur. Polym. J. 2001, 37, 1457-1464, doi:10.1016/S0014-3057(00)00251-2.

Iedema, P.D.; Remerie, K.; Seegers, D.; McAuley, K.B. Tacticity changes during controlled degradation of polypropylene. Macromolecules 2021, 54, 8921-8935, doi:10.1021/acs.macromol.1c01383.

Rosal, R. Morphological description of microplastic particles for environmental fate studies. Mar. Pollut. Bull. 2021, 171, 112716, doi:10.1016/j.marpolbul.2021.112716.

4 General Discussion

This dissertation studies the physicochemical ageing of plastics under laboratory simulated environment conditions. The chemical, physical, and structural changes suffered by different types of plastics were monitored to correlate them with the intensity of stressors and with their fragmentation patterns.

The definition of microplastics (MP, plastics smaller than 5 mm), has been established by UNE-CEN ISO/TR 21960 "Plastics — Environmental aspects — State of knowledge and methodologies", which additionally defines "large microplastics" for particles in the 1-5 mm range, and nanoplastics (NP) for sizes below 1 micron. This definition partially agrees with the one provided by the Group of Experts on the Scientific Aspects of Marine Environmental Protection, which recommends 5 mm as upper size boundary for microplastics without differentiating between large and small microplastics (GESAMP, 2019). This wide range of particle sizes imposes limitations for the different techniques available for the assessment of size, morphology, and the textural and physiochemical properties of plastic particles. The resolution of some techniques sometimes does not allow to distinguish smaller particles below a certain size, and this is especially limiting when working with nanoplastics and microplastics of size below 5-20 microns. In these cases, mass spectrometry techniques are sometimes used, by means of which it is possible to analyze the smaller size fractions, but without obtaining information about each individual particle.

To simulate the solar part of UV irradiation (UVB + UVA, 280 – 400 nm) with energies in the 3.1 to 4.3 eV (72-97 kcal/mol) range, a 150 W medium-pressure mercury lamp (Novalight TQ150), which emitted in the UV (> 300 nm) and visible was used. The equivalence with solar radiation was established using "Nasa Surface meteorology and Solar Energy database", which recorded monthly insolation data for two different latitudes: one from Madrid, 4.4 kWh m^{-2} day^{-1} (183 W m^{-2}), for the experiments

performed into a 1 L photochemical reactor kept at 24 ºC and stirred at a constant rate of 700 min^{-1}, with an average irradiation in the central part of the liquid exposed 1060 Wm^{-2} (UVA+UVB) as described in the Chapters 1 and 2, and other corresponded to Canary Islands, 5.62 kWh m^{-2} day^{-1} (234 W m^{-2}), and was used for the experiments performed in open 250 mL and 90 mm diameter glass containers shacked at 30 rpm to get an even exposure, with an average irradiation 1350 W m^{-2}, as described in Chapter 3.

The experiments were performed used different material. First, for the experiment described in the Chapter 1, three different polyethylene (PE) materials, which were chosen to represent the entire lifecycle of low-density polyethylene (LDPE): virgin pellets, commercial goods, and recycled LDPE. Differences in the degradation process are expected expressed in variations of physical, chemical, and structural properties, as well as the presence of additives in commercial goods and in recycled pellets, which would not be found in virgin pellets, supplied as additive-free. For the experiments described in the Chapters 2 and 3, PE and polypropylene (PP) fragments recovered as marine debris from the beach known as Ámbar, which is located in La Graciosa Island, belonging to the Canary Islands (Spain). In the case of the Chapter 2, polystyrene (PS) foams were collected from Ilha Desserta (Faro, Portugal). The media used was, ultrapure water (Milli-Q, > 18 MΩ cm) in the case of the Chapter 1, and simulated seawater (ASTM D1141-98) in the case of the Chapters 2 and 3.

The experiments described into **Chapter 1** were performed according to two different methods, indicated below as Procedure I, and Procedure II. In Procedure I each exposure run proceeded in parallel using three different reactors with 500 mL ultrapure water and 10% (w/v) LDPE. One of them was irradiated and stirred (I), another one non-irradiated and stirred (NI), and the latter non-irradiated and non-stirred (NI/NS), all of them running for 72 h, with sampling every 24 h. The resulting material at the end of the exposure experiments was filtered at 25 μm, by stainless steel mesh filters

resulting in three size fractions: one solid fraction of large MPs, which corresponded to the degraded initial pellets; another fraction consisting of small secondary MPs > 25 μm (and < 5 mm) formed in the degradation process; and liquid that contained secondary MPs < 25 μm and the NPs formed. Procedure II was also performed for each material, in the same reactor having 500 mL ultrapure water and 10% (w/v) LDPE non-irradiated and stirred (NI) for 72 h. However, after the first 72 h sampling, the pellets were removed to further go ahead with irradiated runs in the same way described before with similar sampling protocol. In Procedure II, only secondary MPs detached from the first plastic fragments were irradiated.

The size fraction of MPs < 5 mm was monitored every 24 h (initial or [0], [24], [48] and [72]), which allowed tracking the evolution of melting temperature (T_m) and crystallinity (X) from Differential Scanning Calorimetry (DSC) data, and hydroxyl (HO, 3200-3500 cm^{-1}), carbonyl (C=O, 1730 cm^{-1}), and carbon-oxygen bonds (C-O-C, 1160 cm^{-1}) and (C-O, 1230 cm^{-1}) absorption bands and relative indexes from "Attenuated Total Reflectance-Fourier Transform Infrared" (ATR-FTIR) spectroscopy (see table 1.1). The results showed that the structural modifications occurring during PE aging are complex. LPDE-1 (virgin pellets) displayed smooth changes according to the expected behaviour for that material. The presence of oxygenated moieties was clear after the first 24 h, in irradiated runs as well as in non-irradiated runs. C-O index revealed structural changes like chain scission or crosslinking reactions leading to functional groups having oxygen, whose bands increased with exposure. The peak of C=O appeared in non-irradiated runs in samples taken after 72 h but after 48 h in irradiated runs. A similar pattern was observed for HO groups. The degradation procedure was somewhat different in the case of LDPE-2 (commercial goods), and LDPE-3 (pellets from recycled greenhouse cover), probably due to the different history of the specimens and to the presence of additives. The results showed significantly higher values for all degradation peaks and indexes after the first 24 h, with a general tendency to increase, in all runs, irradiated or not, compared with pure pellets. Melting temperature slightly decreased and the crystallinity displayed slight increase upon irradiation and to decrease in hydrolytic, non-irradiated runs. The possible changes in

the conformation of LDPE are known to be decided by the first degree of branching, by the inter- and intramolecular forces and by the polarity of the newly generated (and bulky) oxygen-containing groups. The SEM images of LDPE (1, 2 & 3) pellets (see Figure S1.7) showed the formation of surface cracks that are the most probable origin for the small plastic fragments saw as secondary MP, which would be the consequence of detaching fragments from the outer surface or pellets. The micro-FTIR spectra of the small MPs fragments recovered onto 25 μm filters (see Fig S1.5) clearly displayed all the bands usually associated to oxygenated moieties. The results showed significant difference between peak intensity in irradiated and non-irradiated specimens, with higher values for the degradation indexes in irradiated ones (see Table 1.1).

Unfiltered liquid samples taken every 24 h were used to measure particle size distribution using a combination of laser diffractometry (Mastersizer) and flow cytometry. PS latex beads were used as calibration kit (1, 3, 4, 6, 10, 15, and 25 μm) in a background of ultrapure water, which allowed the application of Mie's equation to count the number of particles of assorted sizes. The following size classes were recorded: < 5 μm, 5-25 μm range, and >25 μm. The results (see Figure 1.2) showed that many MPs of small size appeared during the first part of the runs, thereby demonstration a rapid onset of fragmentation even in the absence of prolonged exposure to irradiation. It was found that the mechanical stress was important to produce secondary MP, and that small MPs are much more abundant than larger fragments. The small MPs in the few microns to tens of microns range, as determined by flow cytometry were in the 10^6-10^7 MPs/L (or 10^4-10^5 MPs/g_{LDPE}) range, which represented < 0.01 % of the start mass of exposed polymer.

Unfiltered and < 1 μm filtered samples were recorded every 24 h to measure TOC (NPOC) as a quantification of the LDPE based on dissolved carbon (see Table 1.2). The results showed, for all LDPE types, the presence of secondary MPs in the first 24 h and NPs at 72 h in measurable amount. The particle sizes from samples filtered through micron filter were in the range of a few hundred of nanometres. Assuming the dissolved organic matter was LDPE and that particles were spherical with the size given in Table 1.2 and from the average density of LDPE, the concentration of NP particles could reach about 10^{10} NPs/g_{LDPE}, approximately 0.10 percent of the first mass of the pellets. Aliquots of the final liquid fractions that have

secondary MPs < 25 μm and NPs was filtered by means of 1 μm filters and examined using micro-FTIR to assess the presence of PE in the submicron size range. An extraction system was developed, using xylene as solvent for LDPE, which allowed to obtain solid fragments suitable for micro-FTIR analyses. The results clearly found PE in the NPs size range (see Figure 1.2).

The experiments described in the **Chapter 2,** used marine MPs obtained in real sampling campaigns in geographical points of great environmental interest, as explained above. The material was PE-PP mixed in 88:12 ratio (as sampled from a sandy beach) by weight, and fragments of PS foam all the in MPs size (< 5 mm). The fragments were subject to 360 h of continuous irradiation, with samples every 72 h or five years of solar UVA+UVB exposure and non-irradiated exposure to simulated seawater for 720 h, with intermediate sapling at 360h. Simulated seawater was used as liquid media previously filtered through 0.45 μm filters. For PE-PP runs, a concentration of 40 g/L was used, while PS experiments used 4 g/L (due to the lower density of PS). All runs began with a pre-conditioning non-irradiated 72 h period, in which the number of particles produced from PE-PP and PS MPs reached 1.2-1.8 x 10^5 particles/mg. These results showed that MPs were easily detached from already stressed MP by mechanical stress due to their state of degradation, which was readily visible in the micrographs of fragments shown in Figure S2.2.

All samples taken for flow cytometry analyses were filtered by 100 μm to avoid the clogging of fluid lines. Flow cytometry allowed measuring the particles in the 1-100 μm range, which were calculated per mass of parent PE-PP or PS MPs, after subtracting blanks. The counts were in both cases in the 10^5 – 10^6 particles/mg range (Table 2.1) and is three orders of magnitude over the results obtained in the case of non-environmentally aged LDPE pellets. The most abundant fragments from PE-PP and PS marine MPs were small particles in the few microns range, almost all of them below 10 μm. The average density of PE-PP and PS allowed calculating the mass of PE-PP and PS particles in the 1-100 μm range, which could be estimated as up to 2.5 % of the first mass of PE-PP fragments and about 0.2 % for PS. The results measured the relative abundance of all MP sizes in irradiated and non-irradiated materials. The results were

adjusted to the power law abundance using the logarithmic expression describing the particle concentration as a function of size: log(abundance) = c - α log(size). The results showed an average exponent of the power law at 3.1 for PE-PP (Figure 2.4A), and at 2.9 for PS (Figure 2.4B), in agreement with a three-dimensional fragmentation pattern but much higher that found in environmental size distribution samples (Kooi and Koelmans, 2019). The abundance of NPs could be estimated using TOC values and size from DLS measurements. The results were marked with dots in the upper left side the plots. The deviation from the power law is probably because of the aggregation of NPs with nanoparticles in the background colloid coming from the salts used for simulated seawater.

The generation of NPs appeared clear when examining the TOC of samples filtered by means of 1 μm filters (Figure 2.5). The difference was significant when comparing irradiated runs with non-irradiated runs either for PE-PP or PS. In irradiated runs the results showed the generation of up to 10 mg NPs/g and 2.8 mg NPs/g for PE-PP and PS, respectively, while for runs in the absence of irradiation, both concentrations were about 1 mg NPs/g even after 720 h. The NPs size obtained by DLS (Table 2.2) was in the range of hundreds of nm. It is important to note the presence in simulated seawater of particles having DLS size slightly over 200 nm, probably indicating that the colloid of simulated seawater facilitated the aggregation of NPs, thus explaining the clear deviation of small MPs from the behaviour of those in the 1-100 μm range. TOC data allowed estimating the concentration of NP in the 10^{11}-10^{13} NPs/g range considering an average particle size in the 200-400 nm range (Figure 2.5). This value represents one-to-three orders of magnitude over that determined for pure LDPE in Chapter 1. The spectroscopic identification of NPs by micro-FTIR was possible, with acceptable results (see Figure 2.6) using aliquots of the liquid obtained at the end of the runs after filtration (1 μm), and after extracting with xylene for PE/PP, and trichloromethane for PS.

After finishing the runs, the parent pellets were separated, and the remaining liquid filtered through 25 μm stainless steel mesh. Both the remaining pellets and the secondary MP particles > 25 μm were analysed using FTIR (ATR-FTIR or micro-FTIR).

The recorded spectra are shown in Figure 2.3 for irradiated runs and in Figure S2.5 for non-irradiated experiments. The spectroscopic information displayed unambiguous signs of photooxidation as noticed by C=O stretching bands at 1740 cm-1 and C-O stretching vibration in the 1050-1310 cm^{-1}. The alteration of small MPs was also assessed by means of DSC. The results, plotted in Figure S2.6, presented melting points at 124.5 °C, due to PE, and at 140.9 & 142.9 °C which corresponded to PP in different degradation states. A decrease in PS's glass transition ranges from ~ 100 °C to 50-60 °C could also be interpreted because of photooxidative degradation.

In Chapter 3 a spectroscopic and chemometric study was undertaken with samples from the same marine debris sampled in sandy beaches as indicated below. Specifically, a set of 36 MP were selected as follows: 2 commercial pellets (one LDPE, one PP), 4 fragments of LDPE, HDPE and PP obtained from several commercial goods, and 30 MPs from marine debris (23 PE and 7 PP). For each of them FTIR spectra were recorded every 72 h, during 360 h of irradiation with UVA+UVB equivalent to 5 years of solar irradiation. The samples were: Y0 (initial), Y1 (72 h), Y2 (144 h), Y3 (216 h), Y4 (288 h), and Y5 (360 h). Seven FTIR spectra were obtained per sample generating a total number of 252 spectra per irradiation time. The complete set of spectra resulted in a matrix of 1512 rows (observations) and 6950 columns (variables or wavelengths). The information was extracted using chemometric methods.

OMNIC software was used to assess the changes in absorbance intensity for the different absorbance peaks recorded in the mid-IR, which corresponded to the carbonyl bond (1740 cm^{-1}) the keto-carbonyl bond (1715 cm^{-1}), and the double bonds (1650 cm^{-1} and 908 cm^{-1}, terminal and internal), respectively. The absorbance of those peaks was referred to that of the methylene bond (CH_2 deformation, 1465 cm^{-1}) to calculate keto-carbonyl, ester-carbonyl, vinyl and internal double bound indexes (KCBI, ECBI, VBI, IDBI). The absorbance intensity for amorphous methylene (I_a) at 1474 cm^{-1} and for crystalline methylene (I_b) at 1464 cm^{-1} were used to calculated degree of crystallinity (*X*, %) of PE. In the case of PP, the changes in the absorbance intensity of the ester (1748 cm^{-1}) and methyl groups (1377 cm^{-1}) with reference to the bending of methylene group at 1456 cm^{-1} were used to calculate the ester carbonyl bond (ECBI) and the

methyl group index (MGI) respectively. The isotacticity index (I, %) for PP was calculated by means of the 997 cm^{-1} and 973 cm^{-1} bands. Both for PE and PP, and also using the same reference bands stated before, OH groups were quantified from (1) the intensity of peaks at 3637 cm^{-1}, which corresponded to the OH stretching of intramolecular hydrogen bonds and (2) the bands at 3637 cm^{-1} and 3623 cm^{-1} due to OH groups. The peaks allowed calculating three different hydroxyl indexes as shown in Tables S3.1 and S3.2.

The evolution of the afore mentioned indexes is displayed in Figure S3.1 as a function of the accumulated years of solar exposure. The results showed high values for KCBI and ECBI in certain specimens. However, the evolution of most fragments did not follow an obvious tendency, although maximum values for KCBI and ECBI were frequently observed after a first irradiation period, roughly representing one year of solar light. Concerning PE crystallinity and PP isotacticity the results showed that both parameters decreased with irradiation. Some authors reported a tendency of crystallinity to increase upon photochemical irradiation due to the higher reactivity of the amorphous polymer (Hiejima et al., 2018). An explanation for the decrease of crystallinity is that the formation of bulkier groups decreased polymer compactness (Carrasco et al., 2001). For PP isotacticity the decrease with exposure was probably due to the generation of tertiary carbon radicals, which induce a loss of stereospecificity (Iedema et al., 2021). Photochemical ageing on degradation indexes was clearer when standing for changes between two consecutive measurements rather than absolute values (see Figure 3.1). A non-obvious pattern was also observed for the changes in carbonyl indexes, which increased first to decrease at intermediate doses of ultraviolet exposure (Figure 3.1a, FCBI+ECBI, Figure 3.1b, VBI). The plots in Figure 3.1c, OHi 3360+3623+3637, showed that all the variability could be attributed to OHi-3360 associated to intramolecular hydrogen bonding, because the peaks from primary and non-primary OH only underwent minor changes. Similar, no pattern was seen for PP isotacticity (Figure 3.1d).

A statistic tool was used to derive all the information in the matrix of FTIR spectra. Previously, the information was pre-processed (correction of baseline and offset,

normalization, and smoothing using Unscrambler v10.4 software) Multivariate Data Analysis Software SIMCA® was used for Orthogonal partial least squares discrimination analysis, OPLS-DA with a confidence level for Hotelling's T2 established at 0.05, trying to obtain the highest number of orthogonal components. The models were set using as variables the composition (PE, PP), type of material (pellets, fragments of objects, and marine plastics), colour, and irradiation time. The resulting spectra were: 1512 spectra for All Samples, 84 spectra for Commercial pellets, 168 spectra for Fragments of objects, 1260 spectra for Marine debris, 1050 spectra for PE, and 462 spectra for PP, which resulted a root mean square error of estimation and root mean square error of cross validation as shown in Table 3.1. The effect of the photo-oxidative degradation checked as a gradient of irradiation time, appeared in the models within group class Irradiation Time and is presented in Figures 3.2a (all samples, PE+PP, 3.2a1, PE samples 3.2a2, PP samples 3.2a3). The results allow a good grouping of the specimens depending on the received dose of UV irradiation, due to the management of all the information contained in the spectra. For OPLS-DA models, predicted vs. observed, regression plots are presented in Figure 3.2b1 for all samples (PE+PP), 3.2b2 for PE samples and 3.2b3 for PP samples, with the following coefficients of determination, R2 equal 0.7551 for PE+PP, 0.9575 for PE, and 0.8203 for PP respectively, which showed the robustness of OPLS-DA models were robust and their good fitting to experimental data. The three models showed CV-ANOVA p-value < 0.05, thereby confirming the finding of significant differences among treatments. The models OPLS-DA obtained for PE and PP were used to analyse the effects of the photo-oxidation process selecting data year by year (Y1…Y5) and comparing with first data, Y0 (Figures 3.3a1 to 3.3a5 for PE and Figure 3.4a1 to 3.4a5 for PP). The contribution threshold was set to 0.5 and the results are summarized in Figures 3.3b1 to 3.3b5 for PE and Figures 3.4b1 to 3.4b5 for PP, respectively. When spectra were analysed as a whole, the information contained in the different absorbance peaks used in classic degradation indexes also appeared. For example, the OH stretching bands (3623 cm^{-1} and 3637 cm^{-1}) significantly contributed from Y1 to Y3. The opposite was observed for the peak at 1650 cm^{-1} due to terminal double bonds (see Figures 3.3c1 to 3.3c5). Concerning PP, the OH stretching absorption was significant at the beginning of the

exposure to decreased until reaching negative correlation. The carbonyl stretching (1748 cm^{-1}) reached > 0.75 score after the first year or simulated irradiation to follow a non-simple pattern thereafter (see Figures 3.4c1 to 3.4.c5). Variable influence on projection (VIP) analysed as total VIP, predictive VIP, and orthogonal VIP for PE+PP, PE, and PP OPLS-DA models is plotted in Figures 3.5a1 to 3.5a3 for PE+PP, Figure 3.5b1 to 3.5b3 for PE, and Figures 3.5c1 to 3.5c3 for PP. The results showed that it is possible to allowed to quantitatively assess the discriminating power of certain. Peaks associated with VIP > 1 could be considered highly explanatory. Accordingly, the explanatory peaks were for PE 1650 cm^{-1}, 1715 cm^{-1}, and 1740 cm^{-1}, and for PP 1748 cm^{-1}. Other with lower VIP could be considered moderately explanatory like that at 1377 cm^{-1} for PE+PP and 973 cm^{-1} for PP, corresponding to MGI and Isotacticity. The peaks used as reference did not convey degradation information, confirming they were correctly selected.

References:

Carrasco, F.; Pagès, P.; Pascual, S.; Colom, X. Artificial aging of high-density polyethylene by ultraviolet irradiation. European Polymer Journal 37, 1457-1464, 2001.

GESAMP, 2019. Guidelines for the monitoring and assessment of plastic litter in the ocean. In: Kershaw, P.J., Turra, A., Galgani, F. (Eds.), Rep. Stud. GESAMP No. 99. IMO/FAO/UNESCO-IOC/UNIDO/WMO/IAEA/UN/UNEP/UNDP/ISA Joint Group of Experts on the Scientific Aspects of Marine Environmental Protection, p. 130.

Hiejima, Y.; Kida, T.; Takeda, K.; Igarashi, T.; Nitta, K.-h. Microscopic structural changes during photodegradation of low-density polyethylene detected by Raman spectroscopy. Polymer Degradation and Stability 150, 67-72, 2018.

Iedema, P.D.; Remerie, K.; Seegers, D.; McAuley, K.B. Tacticity changes during controlled degradation of polypropylene. Macromolecules 54, 8921-8935, 2021.

Kooi, M., Koelmans, A.A. Simplifying microplastic via continuous probability distributions for size, shape, and density. Environmental Science & Technology Letters, 6(9), 551-557, 2019.

Conclusions

The generation of small MPs from the photochemical degradation of PE, PP and PS was assessed using flow cytometry and laser diffractometry. The results showed that secondary MPs < 100 μm reached 10^4-10^5 MPs/g for LDPE pellets and up to 10^8-10^9 MPs/g in the case of marine MP debris.

For marine PE-PP and PS MPs, most secondary particles formed during irradiation (98%) were < 10 μm (modal value 2 μm) and followed a particle size distribution consistent with a three-dimensional fragmentation pattern.

Using DLS particle size and TOC for the fraction < 1 μm, the concentration number of NPs could be estimated about 10^{10} NPs/g for LDPE pellets and 10^{11}-10^{13} NPs/g for marine MPs, representing 10 mg NPs/g for PE-PP and 2.8 mg NPs/g for PS. A solvent extraction allowed identifying the chemical nature of NPs using micro-FTIR.

Chemometric models based on OPLS-DA were used to process the information contained in mid-infrared spectra. The obtained models were robust and allowed clustering MPs as a function of the received irradiation. VIP analyses showed that the most explanatory absorption peaks corresponded to the stretching absorptions of hydroxyl and carbonyl moieties.

Abbreviations

ATR-FTIR	Attenuated Total Reflectance-Fourier Transform Infrared
CAS	The Chemical Abstract Service
C-O	Carbon-Oxygen bonds
C=O	Carbonyl
C-O-C	Ether
CV-ANOVA	Analysis of Variance Testing of Cross Validated Predictive Residuals
DLS	Dynamic Light Scattering
DSC	Differential Scanning Calorimetry
ECBI	Ester-Carbonyl Bond Index
EPS	Expanded Polystyrene
EU	European Union
eV	Electron-volt
FSC	Forward-scattered light
GESAMP	Joint Group of Experts on the Scientific Aspects of Marine Environmental Protection
HDPE	Hight Density Polyethylene
HO	Hydroxyl
Hoi	Hydroxyl Index
I	Irradiated
I_a	Absorbance for FTIR band at 1474 cm^{-1}
I_b	Absorbance for FTIR band at 1464 cm^{-1}
IDBI	Internal Double Bond Index
KCBI	Keto-Carbonyl Bond Index
LDPE	Low Density Polyethylene
MP(s)	Microplastic(s)
MΩ	Megaohm
n	Particle diameter
NASA	National Aeronautics and Space Administration

NI	Non-irradiated
NP(s)	Nanoplastic(s)
NS	Non-stirred
(O)PLS-DA	(Orthogonal) Partial Least Squares-Discriminant Analysis
PE	Polyethylene
PP	Polypropylene
PS	Polystyrene
Q^2	Goodness-of-Prediction
rpm	Revolutions per minute
R^2P	Coefficient of Determination in Prediction
R^2X/Y	Goodness-of-Fit
RMSECV	Root Mean Square Error of Cross-Validation
RMSEE	Root Mean Square Error of Estimation
SEM	Scanning Electron Microscopy
SIMCA	Soft Independent Modelling of Class Analogy
SM	Supplementary Material
SNV	Standard Normal Variate
SSC	Side-scattered light
T_m	Melting Temperature
TOC	Total Organic Carbon
UV	Ultraviolet Radiation
UVA	Ultraviolet A Radiation
UVB	Ultraviolet B Radiation
v	volume
VBI	Vinyl Bond Index
VIP	Analysis of Variable Importance of the Projection
w	weight
WEF	World Economic Forum
X	Crystallinity
Xe	Xenon
σ_s	Scattering cross-section